공학박사 학위논문

양팔 매니퓰레이터와 수중 운항 플랫폼의 협업 작업

Cooperative operation of underwater robotic vehicle and dual-arm manipulator

2019년 2월

서울대학교 대학원
기계항공공학부

배 장 호

양팔 매니퓰레이터와 수중 운항 플랫폼의 협업 작업

Cooperative operation of underwater robotic vehicle and dual-arm manipulator

지도 교수 김 종 원

이 논문을 공학박사 학위논문으로 제출함
2018 년 10 월

서울대학교 대학원
기계항공공학부
배 장 호

배장호의 공학박사 학위논문을 인준함
2018 년 12 월

위 원 장 _____ (인)

부위원장 _____ (인)

위 원 _____ (인)

위 원 _____ (인)

위 원 _____ (인)

Abstract

This paper proposed a manipulation method for turning a handle valve with dual-arm underwater vehicle-manipulator system (UVMS) and the cooperative manipulation algorithm between the vehicle and the manipulator was developed. By dividing task loads between two subsystems with the algorithm, the system can turn handle valve and compensate external disturbance efficiently, which has never been proposed. Previous underwater systems used a manipulator only for performing specific task and a vehicle thrust force only for compensating external disturbance with free floating vehicle. In this study, one arm of dual-arm manipulator was used for clamping the whole system on fixed structure to increase efficiency and stability with respect to external disturbance. Also, this paper provided cooperation algorithm between the manipulator and the vehicle to make the two subsystems help each other. With the cooperation algorithm, the system can perform valve turning task with smaller manipulator torque.

The manipulation method that grabs a fixed structure with one arm while performing objective task was proposed on this paper. When grabbing fixed structure, the whole system can be considered as parallel manipulator. Due to the kinematic properties of parallel manipulator, the torque and force for performing task can be distributed between the manipulator and the vehicle. In addition, the system can produce internal force with manipulator and can compensate external disturbance easily. By dynamic simulation, the proposed method was compared with common methods, the single arm and the dual-arm without clamping. The vehicle thrust force and manipulator torque were reduced with the proposed manipulation method, and effect of these advantages maximized when the disturbance was applied.

Based on the manipulation method, the structure and configuration of the manipulator were optimized. Four design alternatives were created to distribute certain number of degree of freedom between two arms. Dynamic manipulability

was set as objective function, which can consider not only kinematics but also dynamic properties. Each design alternative was optimized to have maximum total dynamic manipulation during operation with genetic algorithm. After optimizing link lengths and trajectories, the optimal structure was selected between two alternatives that has large dynamic manipulability.

After that, cooperative manipulation method of the system was developed. The system can be considered as a redundant parallel manipulator. Therefore, the force and torque for turning handle valve can be distributed by applying weighted pseudoinverse to Jacobian of the system. The vehicle thrust which was not used on common method can be used to help the valve turning operation of the manipulator. On the contrary, the manipulator can help disturbance compensation of the vehicle with small amount of torque. In this research, the task load was distributed with respect to maximum capabilities of each actuator. Simulations were conducted to prove the advantages of the algorithm. The manipulator torque were significantly reduced while applying cooperation algorithm on the valve turning, and the vehicle thrust force for compensating disturbance was also reduced with the algorithm.

Finally, the proposed cooperation algorithm was proved by valve turning experiments. The waterproof joint actuator module was designed and manufactured, and the dual-arm manipulator was made by connecting joint modules. To make the joint module apply desired torque from the algorithm, the torque controller and friction compensation method were also designed. Experiments were conducted the constructed test bench with handle valve in a water tank. The valve turning and disturbance compensating experiments were conducted, and the advantages of the cooperation algorithm were proved.

Keyword : underwater vehicle-manipulator system, dual-arm manipulator, mobile manipulation, cooperation, handle valve turning, manipulator design.

Student Number : 2012-23167

Table of Contents

List of the Tables

List of the Figures

Chapter 1. Introduction

1.1 Motivation

1.1.1 Previous UVMSs

The need for underwater operation is rising due to growth of oceanic industries. Underwater tasks, such as exploring, intervention, mining and construction, are usually not safe for human divers due to harsh condition. Due to safety issues, using an underwater vehicle-manipulator system (UVMS) is efficient for performing underwater operations. There are mainly two types of UVMS, the one is heavy UVMS and the other is light UVMS. Examples of two UVMS types and their mechanical speculations are shown in Table 1.1.

Table 1.1 Examples of two types of UVMS for underwater operations, and their speculations.

Types	Heavy UVMS	Light UVMS
Pictures		
Name	Leopard (2014), SAAB [1]	DTG2 worker (2013), Deep Trekker [2]
Size	2150 × 1174 × 1160 mm^3	325 × 258 × 279 mm^3
Weight	1200 kg	8.5 kg
Depth	2000 m	75 m
Manipulator	11 DOF, two arms	2 DOF, one arm

The heavy UVMS is currently used mainly in deep water operations, such as constructing and intervention task on an oil well. This type of UVMS tends to have enough payload for underwater operation and robotic arms that have enough degree-of-freedoms (DOF). Also, the heavy type UVMS can maintain stability under disturbance such as oceanic current because of its inertia and strong thrusters. However, due to its large size and heavy weight, it is not easy to perform shallow water operations, which operation mainly performed by human divers.

On the contrary, the light UVMS is easy to perform tasks in shallow water because of its small size and light weight. However, the light UVMS is currently not used in actual underwater operation, but only in inspection tasks. Due to its small size and light weight, the light UVMS usually cannot use robotic arm that strong enough to perform underwater operations. Not only strength of a robotic arm, but also DOFs of a robotic arm usually insufficient to perform various underwater operations. For these reasons, the light type UVMS is currently not suitable for performing underwater operation.

Therefore, the medium size UVMSs are currently being researched. Various types of UVMS were designed and developed [3-7]. Some researches considered the controller of the end-effector without setting specific objective task [3-4], and other researches set specific objective task such as operating valve panel [5], and transferring object [6-7]. In this paper, the medium size UVMS is developed with specific objective task.

1.1.2 Underwater vehicle TTURT

1.1.2.1. Mechanical design

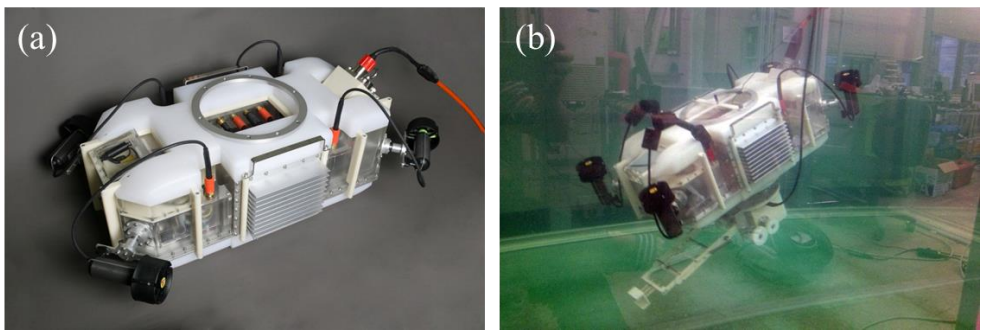

Fig. 1.1 (a) The appearance of TTURT; (b) Hovering test of TTURT

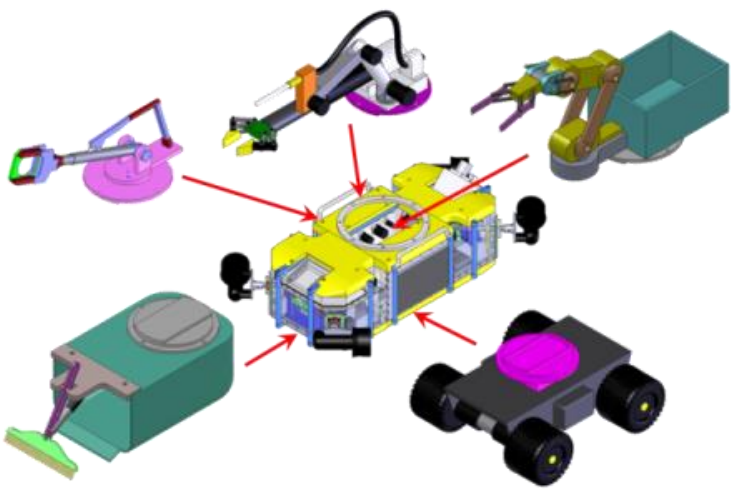

Fig. 1.2 The platform-module design of TTURT

A previous study proposed underwater platform, the name of which is tilting thrusting underwater robot (TTURT) [8-9]. Fig. 1.1 shows the appearance of TTURT and its hovering test dive. TTURT has four thrusters and two tilting motors. The two front thrusters and two rear thrusters are tilted simultaneously with one tilting motor each. TTURT achieved six DOF hovering motion with reduced number of actuators, while conventional UVMS uses eight thrusters. The mechanical specifications of TTURT was described in table 1.2.

Table 1.2 Mechanical specifications of TTURT [8].

Mechanical parameters	**Values**	
Size	326 × 755 × 280 mm^3	
Weight	57.1 kg	
Density	1021.5 kg/m^3	
	Values	
Power capacity	1200 W	
Max thrust	Horizontal	80 N
	Vertical	114 N
Max velocity	Horizontal	1.1 m/s
	Vertical	0.6 m/s

The platform-module design concept was applied on TTURT. Various modules can be attached to module attachment point of TTURT. Fig 1.2 shows the platform-module concept of TTURT, and attachment points. Previously, the underwater capturing manipulator was designed and developed [10], which is presented on Fig. 1.3. TTURT has two module attachment points, the one is on the top of the system, and the other one is on the bottom.

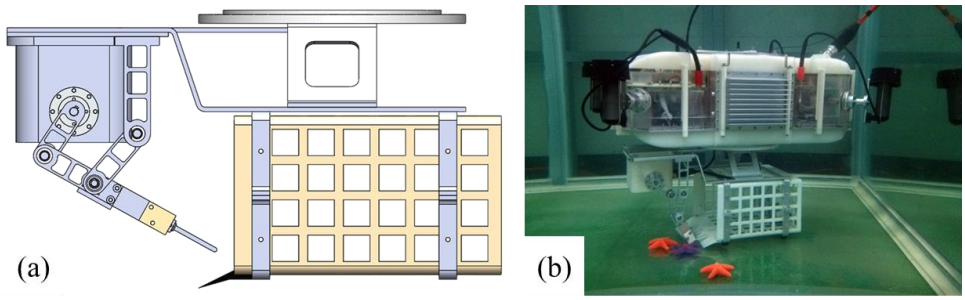

Fig. 1.3 Starfish capturing module for TTURT—(a) 3D modeling of starfish capturing module; (b) Manufactured starfish capturing module.

1.1.2.2. Control method

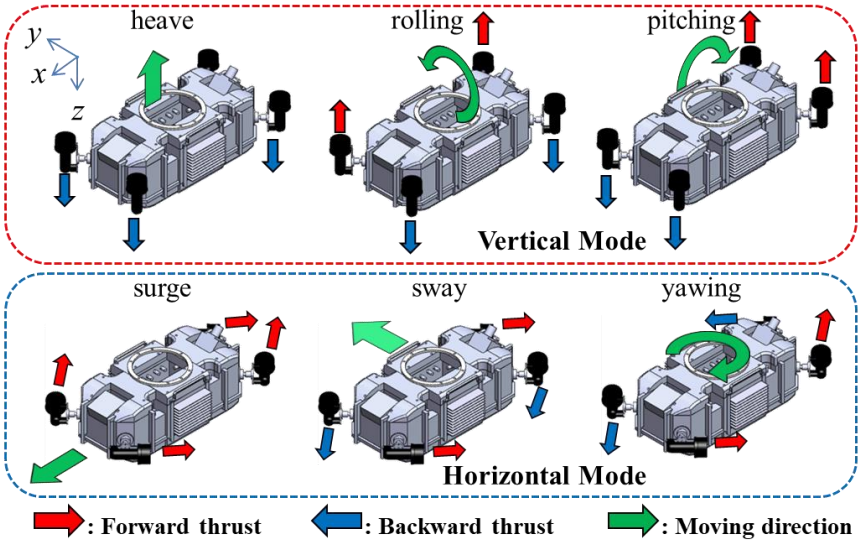

Fig. 1.4 6 DOF movement method with TTURT

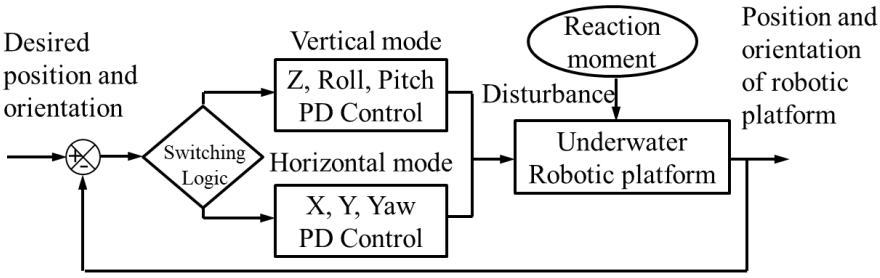

Fig. 1.5 Selective switching control diagram of TTURT

The selective switching controller was applied to TTURT to achieve 6 DOF hovering motion. Due to the nonlinearity from tilting mechanism, the system cannot control six DOF motion simultaneously. Instead, the system is divided into two 3 DOF subsystems, the one is vertical mode and the other one is horizontal mode. Configuration of each system is presented on Fig 1.4. Each subsystem is controlled by PD controller. The switching controller picks a subsystem that has larger error than the other and control the subsystem until the error is smaller than the other subsystem. The control diagram of TTURT is described on Fig 1.5.

1.2 Manipulation objectives of UVMS

1.2.1 Valve turning operation

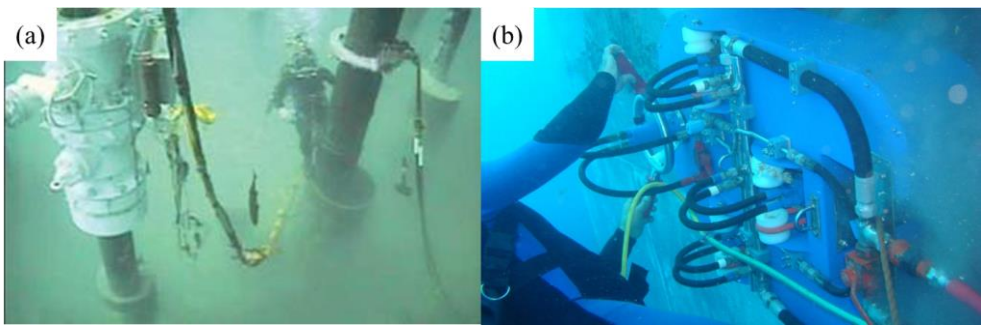

Fig. 1.6 Handle valves in underwater condition—(a) Handle valve located on wellhead of oil rig in the Gulf of Mexico [11]; (b) Handle valve on the underwater structure [12].

Operating handle valve is one of the most important tasks in underwater condition. Fig. 1.6 shows the example of handle valves located in the ocean. Currently, the handle valve located on shallow water, shallower than 75 m deep, is operated by human divers [13]. However, as mentioned on the previous section, the underwater operation is dangerous for human. Therefore, various researches were conducted to operate handle valves with UVMS. Fig. 1.7 shows the valve turning researches by using UVMS.

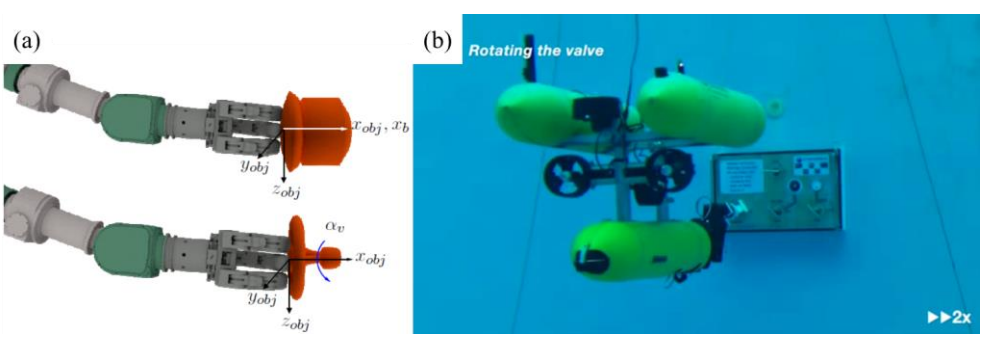

Fig. 1.7 Researches about operating handle valve with UVMS—(a) Analyzing interaction terms while turning the handle valve [14]; (b) Rotating valve handle experiment [15].

1.2.2 Clamping on environments

Fig. 1.8 Ocean one's docking on the underwater structure while the system is under large disturbance [5].

External disturbance such as oceanic current is one of the main problems on underwater operations. Stability and accuracy of robotic systems could be improved by using of the operational environment. Grabbing or clamping of environmental elements, such as handrails or pipes, results in creation of a reaction force, which prevents sudden movement or system collapse. Harada et al. proposed a humanoid-robot balancing method involving grasping of a handrail. Through experiments, their study demonstrated increased stability during motion of a robot climbing up a large step [17]. Koyanagi et al. developed a pattern generator for humanoid robots involving touching of a handrail, and demonstrated increase in stability of the robot while walking over a rough terrain [18]. Lehmann et al. succeeded in increasing the accuracy of milling operations performed by clamping onto a rigid environment [19].

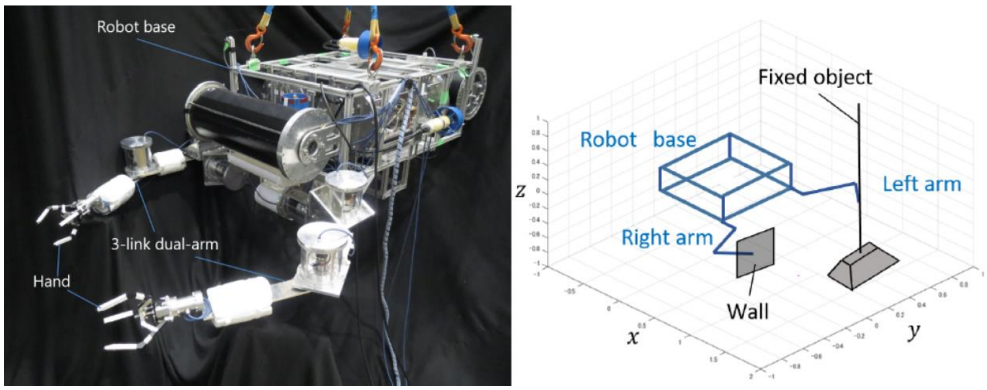

Fig. 1.9 Research about increasing vehicle's stability by clamping left arm on the fixed object while maintaining contact force of right arm [16].

The underwater system is very vulnerable to external disturbance. However, few researches consider grabbing fixed object while performing tasks. Khatib et al., showed the idea to Ocean one UVMS to stand underwater disturbance on his article, and this docking method is shown in Fig. 1.8. However, they only considered withstanding disturbance, not performing task under disturbance. Seki et al., presented control method that can stabilize the vehicle by clamping fixed structure while maintaining contact force of the right end-effector. They applied position control on the vehicle and left arm, and torque control on the right arm. The presented control scheme was proved by simulation. Fig. 1.9 shows outlines of the research about clamping.

1.2.3 Cooperation between a vehicle and a manipulator

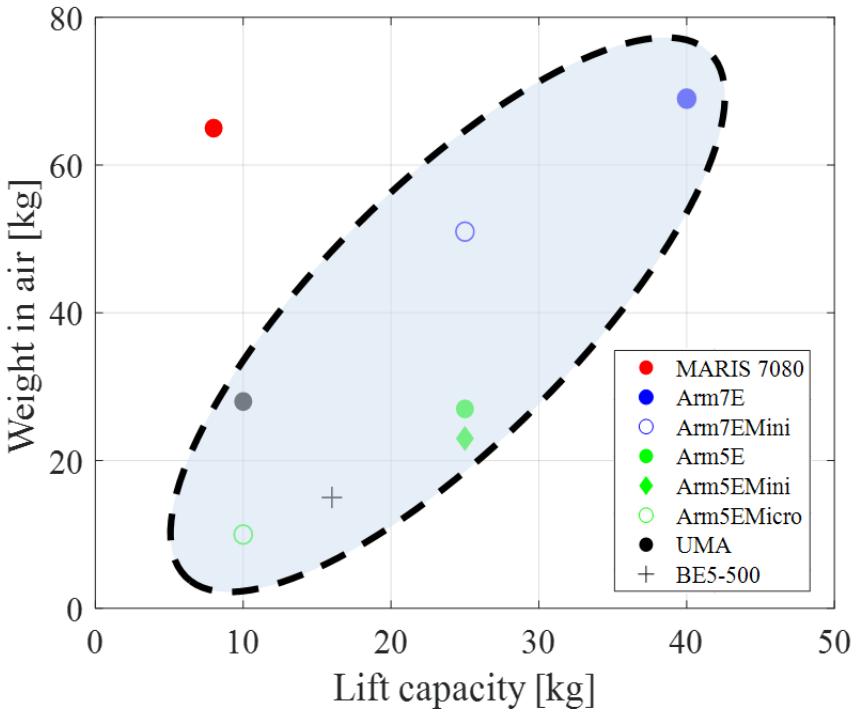

Fig. 1.10 Relation between air weight and lift capacity of commercial underwater manipulators [20]

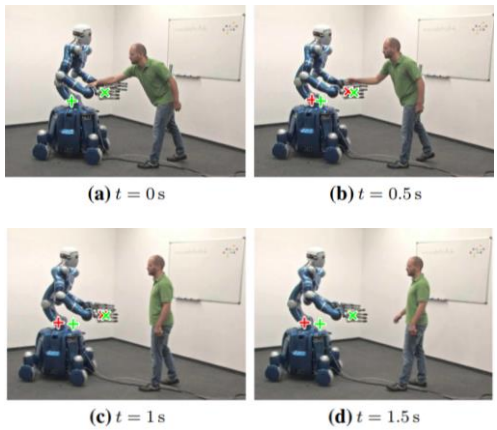

Fig. 1.11 Cooperative compliant control between a mobile base and upper body of Rollin' Justin [21]

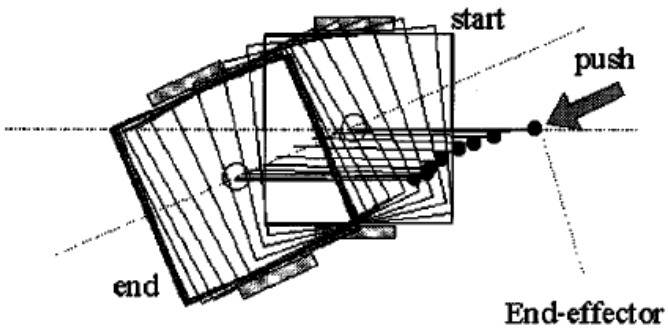

Fig. 1.12 Cooperation between a mobile base and a single-arm manipulator under external force [22]

In mobile manipulator system, the strength of manipulator is limited due to weight and size of the actuator. Fig. 1.10 shows the relation between weight in air and lift capacity of electric underwater manipulators. The stronger the actuator is, the heavier the actuator becomes. To overcome this limitation, the cooperation method between a mobile base and a manipulator is needed. If the strong mobile base helps the manipulator's task, the burden of manipulator can be reduced.

There were several researches about cooperation between a mobile base and a manipulator. Inoue et al. presented cooperation controller between a non-holonomic mobile base and a single arm manipulator to cope with external force, which is shown in Fig. 1. 12 [22]. Dietrich et al. also proposed cooperative compliance control of Rollin' Justin robot and perform an experiment to verify the controller with the robot [23]. Cooperation between two subsystems was also researched on underwater robotic systems. Han et al. minimized restoring moment of a single-arm UVMS by using both of an underwater vehicle and a single-arm manipulator [24]. Simetti and Casalino achieved subtasks with inequality while performing a transferring task by using whole body system [25]. However, there was no researches about distributing task loads between two subsystems on torque and force level for performing certain objective task.

1.3 Research objectives

The main objective of the research is developing a dual-arm underwater vehicle-manipulator system that can perform shallow water operations mainly done by human divers. By attaching a dual-arm manipulator module to existing underwater platform TTURT, a dual-arm UVMS can be made. Turning underwater handle valve was selected as objective task for the UVMS, because operating handle valve is conventional intervention task on underwater as mentioned on previous sections. This research includes two main topics.

The first topic is design and manufacture a dual-arm manipulator module which is attached to underwater platform TTURT. To perform handle valve turning task, the manipulation method of the UVMS should be determined, such as single-arm or dual-arm manipulation. To maintain stability of system under disturbance, clamping on the environmental structure was considered and advantages of the method is proved. After selecting proper manipulation method, the joint structure of the manipulator module should be optimized for valve turning task. The placement of joints between two arms was determined to maximize the dynamic manipulability, which can consider dynamic properties of the system such as inertia, drag and maximum torque. Finally, the dual-arm manipulator module was designed and manufactured to verify the following cooperation concept.

The second topic is developing cooperation manipulation method between the dual-arm manipulator and the vehicle. The kinematics and dynamics of the whole system were modelled. After that, the optimal trajectory of the system was defined. To overcome limitation of small and light system, the loads on the manipulator should be distributed to the vehicle. By using redundant degree of freedom of the system, the task loads can be distributed between two subsystems. Also, external disturbance should be compensated during a valve turning operation. Compensating term was considered and added on the controller. Disturbance

compensating loads were also distributed between two systems. The effect of the cooperation method was verified with experiments.

The rest of the paper is organized as follows. In chapter 2, the manipulation method was determined and the advantages of clamping on a structure were proved by simulations. Chapter 3 provides the design and optimization method of a dual-arm manipulator module for the UVMS. The kinematics and dynamics modeling of the UVMS and cooperation manipulation method between the vehicle and dual-arm manipulator is explained on chapter 4. The simulation results of cooperation method are organized on chapter 5. In chapter 6, detailed design and manufacturing of the dual-arm manipulator module is provided and experimental results are discussed. Finally, chapter 7 summarized the conclusion of the research.

Chapter 2. Manipulation method determination

2.1 Manipulation methods for valve task

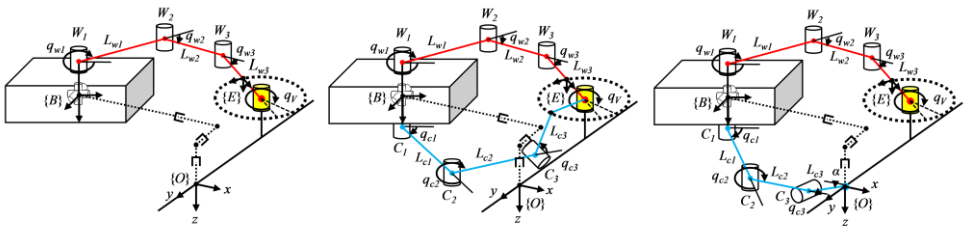

Fig. 2.1 Kinematic diagram of the three manipulation methods: (a) Single-arm manipulation (M1); (b) Dual-arm manipulation (M2) with manipulators grabbing at two points on the handle valve; (c) Dual-arm manipulation (M3) with clamping manipulator grabbing an underwater pipe located near handle valve.

As mentioned on the introduction section, the platform-module concept was applied in TTURT design. There exist two connectors that can attach to working modules—one connector is located at the top of the vehicle while the other is located at the bottom. Handle valve turning, which is an important underwater operation, was assigned as the objective task for the proposed UVMS.

Owing to the limited number of attachment points, only the single and dual-arm manipulation methods could be considered for the handle valve turning task. The single-arm method involves no choice but to hold the handle valve with the end-effector of the single arm. Dual-arm manipulation, on the other hand, offers two possible cases. In the first case, both UVMS arms are used to grab the valve handle, which is the typical method of operating with dual arms. The second case involves grabbing the valve handle with one arm, the other arm being used to clamp onto a nearby underwater pipe. Schematic representations of the three candidate methods are depicted in Fig. 2.1.

2.2 Manipulation methods modeling

2.2.1. Kinematics modeling

When the proposed UVMS grabs the handle valve, the entire system can be considered as a parallel manipulator, and the underwater vehicle can be modeled as a combination of three unlimited prismatic and three rotational joints located on the fixed base and at the center of the vehicle, respectively [25]. The handle valve was modeled as a virtual passive joint with virtual linkage extended up to the last manipulator joint. Therefore, when grabbing the handle valve, the entire system could be considered as a parallel manipulator attached to the ground. Fig. 2.1 depicts the parallel kinematic modeling of the three manipulation methods.

Notations used for the three manipulation methods are described in Fig 2.1. The upper arm that grabs the valve handle is referred to as the "working manipulator" while the lower arm, which grabs the valve handle or pipe, is called the "clamping manipulator." The origin is denoted by $\mathbf{O}$, and the position of the vehicle center is indicated as $\mathbf{B}$. The *i*-th joint of the working manipulator is denoted by $\mathbf{W}_i$ while that of a clamping manipulator is denoted by $\mathbf{C}_i$. Position of the virtual joint, which is equivalent to that of the handle valve, is denoted by $\mathbf{V}$. L_{wi} and L_{ci} denote linkage lengths of the working and clamping manipulators. The *i*-th joint angle of the working manipulator is expressed as q_{wi} while that of the clamping manipulator is denoted by q_{ci}. The end-effector of the working manipulator is indicated as $\mathbf{E}$. Lastly, the joint angle at the virtual joint—indicating the angle of the handle valve—is denoted by q_v.

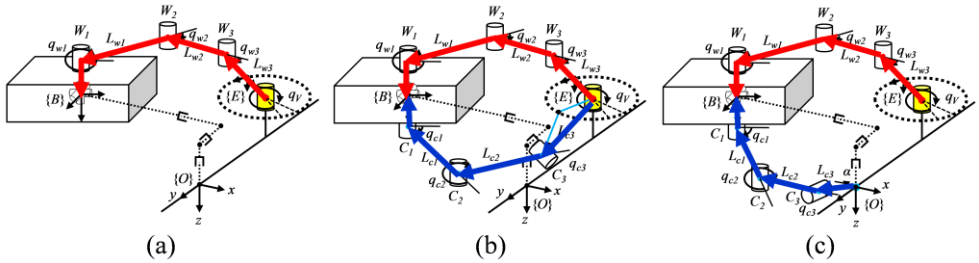

Fig. 2.2 Constraints of manipulation methods—(a) M1, (b) M2, and (c) M3. Position and orientation of the vehicle must be same as that derived using manipulator angles.

The above kinematics of the three manipulation methods was solved in accordance with the theory of parallel manipulators [26]. The minimum number of joints required to express the system configuration were referred to as independent joints, represented by $\boldsymbol{q}_u$. All other joints were called dependent joints, denoted by $\boldsymbol{q}_v$. Joints that controlled by actuators were called active joints, $\boldsymbol{q}_r$. Table 2.1 lists a grouping of joints for each manipulation method. The vector $\boldsymbol{\eta}=[x,y,z,\varphi,\theta,\psi]^{\mathrm{T}}$ indicates the position and orientation of the vehicle in the earth-fixed coordinate frame; $\boldsymbol{q}_w=[q_{w1},q_{w2},q_{w3}]^{\mathrm{T}}$ and $\boldsymbol{q}_c=[q_{c1},q_{c2},q_{c3}]^{\mathrm{T}}$ represent joint vectors for the working and clamping manipulators, respectively; q_{Vc} is the handle valve angle with respect to the clamping manipulator, which is required for M2 to fully represent its configuration.

Table 2.1 Independent and active joints of three manipulation methods

Manipulation Method	M1	M2	M3
Independent joints ($\boldsymbol{q}_u$)	$[\psi,\boldsymbol{q}_w{}^{\mathrm{T}}]^{\mathrm{T}}$	$[x,y,\psi]^{\mathrm{T}}$	$\boldsymbol{q}_w$
Active joints ($\boldsymbol{q}_r$)	$[\boldsymbol{\eta}^{\mathrm{T}},\boldsymbol{q}_w{}^{\mathrm{T}}]^{\mathrm{T}}$	$[\boldsymbol{\eta}^{\mathrm{T}},\boldsymbol{q}_w{}^{\mathrm{T}},\boldsymbol{q}_c{}^{\mathrm{T}}]^{\mathrm{T}}$	$[\boldsymbol{\eta}^{\mathrm{T}},\boldsymbol{q}_w{}^{\mathrm{T}},\boldsymbol{q}_c{}^{\mathrm{T}}]^{\mathrm{T}}$
All joints ($\boldsymbol{q}_{all}$)	$[\boldsymbol{\eta}^{\mathrm{T}},\boldsymbol{q}_w{}^{\mathrm{T}},q_V]^{\mathrm{T}}$	$[\boldsymbol{\eta}^{\mathrm{T}},\boldsymbol{q}_w{}^{\mathrm{T}},\boldsymbol{q}_c{}^{\mathrm{T}},q_V,q_{Vc}]^{\mathrm{T}}$	$[\boldsymbol{\eta}^{\mathrm{T}},\boldsymbol{q}_w{}^{\mathrm{T}},\boldsymbol{q}_c{}^{\mathrm{T}},q_V]^{\mathrm{T}}$

Constraint equations were derived to resolve forward kinematics corresponding to the three manipulation methods. Vehicle position and orientation could be derived using joint angles and lengths of manipulators, which should be equivalent to the actual vehicle position and orientation. Fig. 2.2 depicts how constraint equations for the three manipulation methods were derived. In case of M1, the earth-fixed vehicle position and orientation vector $\boldsymbol{\eta}$ must be equal to that derived using joint angles of the working manipulator ($\boldsymbol{\eta}_w$). For M2 and M3, $\boldsymbol{\eta}$ must be equivalent to $\boldsymbol{\eta}_w$ and $\boldsymbol{\eta}_c$—the position and yaw orientation derived using joint angles of the clamping manipulator. Additionally, in the case of M2, the difference between the handle valve angles q_V and q_{Vc} must remain constant during operation, because both manipulators grab the same structure. Constraint equations corresponding to the three manipulation methods could, therefore, be expressed as follows:

$$
\begin{aligned}
&\mathbf{g}_{\mathrm{M1}}(\boldsymbol{q}_{all}) = \boldsymbol{\eta}_w - \boldsymbol{\eta} \\
&\mathbf{g}_{\mathrm{M2}}(\boldsymbol{q}_{all}) = [(\boldsymbol{\eta}_w - \boldsymbol{\eta})^{\mathbf{T}}, (\boldsymbol{\eta}_c - [x, y, z, \psi]^{\mathbf{T}})^{\mathbf{T}}, q_V - q_{Vc} - \beta]^{\mathbf{T}} \\
&\mathbf{g}_{\mathrm{M3}}(\boldsymbol{q}_{all}) = [(\boldsymbol{\eta}_w - \boldsymbol{\eta})^{\mathbf{T}}, (\boldsymbol{\eta}_c - [x, y, z, \psi]^{\mathbf{T}})^{\mathbf{T}}]^{\mathbf{T}}
\end{aligned}
\tag{2.1}
$$

The vector $\mathbf{g}_{\mathrm{M}i}$ indicates constraint equation for the *i*-th manipulation method; β denotes the angle between the last linkages of the working and clamping manipulators while grabbing the handle valve in M2. The roll and pitch derived from clamping manipulator were removed due to dependencies along the derived z position of the vehicle. All constraints must equal zero during the proposed UVMS operation. The specific terms of equations (2.1) were derived by using screw theory [27].

The constraint Jacobian could be obtained by differentiating the constraint equations with respect to time. With the constraint Jacobian, relations between the independent and all other joint velocities could be obtained. Derivation of these relations was proceeded as follows:

$$\frac{d\mathbf{g}_{\mathrm{M}i}(\boldsymbol{q}_{all})}{dt} = \mathbf{G}_{\mathrm{M}i}\dot{\boldsymbol{q}}_{all,\mathrm{M}i} = \boldsymbol{O} \tag{2.2}$$

$$\dot{\boldsymbol{q}}_{v,\mathrm{M}i} = \boldsymbol{\Phi}\dot{\boldsymbol{q}}_{u,\mathrm{M}i} \tag{2.3}$$

$$\dot{\boldsymbol{q}}_{all,\mathrm{M}i} = \boldsymbol{\Lambda}\dot{\boldsymbol{q}}_{u,\mathrm{M}i} \tag{2.4}$$

$$\dot{\boldsymbol{q}}_{r,\mathrm{M}i} = \boldsymbol{\Gamma}\dot{\boldsymbol{q}}_{u,\mathrm{M}i} \tag{2.5}$$

Subscript $\mathrm{M}i$ indicates involvement of the vector in the *i*-th manipulation method. Equation (2.2) describes differentiation of the constraint equation with respect to time. Aligning the row of the constraint Jacobian and performing matrix inversion, equations (2.3) and (2.4) could be obtained. Relations between the independent and active joint velocities could also be deduced by selecting the row of Jacobian $\boldsymbol{\Lambda}$ given by equation (2.5).

Relations between the handle valve angular velocity $\dot{q}_V$ and independent joint velocity vector $\dot{\boldsymbol{q}}_u$, through use of the forward Jacobian of the respective manipulation methods, can be derived as follows:

$$\dot{q}_V = \mathbf{J}\dot{\boldsymbol{q}}_{all,\mathrm{M}i} \tag{2.6}$$

$$\dot{q}_V = (\mathbf{J}_{u,\mathrm{M}i} + \mathbf{J}_{v,\mathrm{M}i}\boldsymbol{\Phi})\dot{\boldsymbol{q}}_{u,\mathrm{M}i} = \mathbf{J}_{f,\mathrm{M}i}\dot{\boldsymbol{q}}_{u,\mathrm{M}i} \tag{2.7}$$

Equation (2.6) could also be derived using the relation between the vehicle yaw and manipulator joint angles. Substituting equations (2.3) and (2.4) to obtain equation (2.7), which is the forward Jacobian of *i*-th manipulation method, $\mathbf{J}_{f,\mathrm{M}i}$.

2.2.2. Dynamics modeling

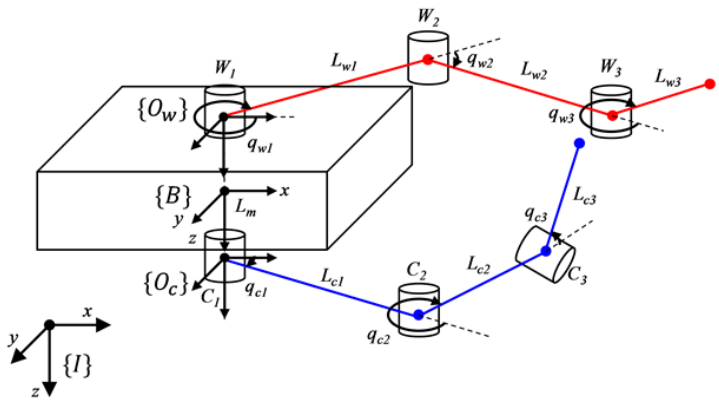

Fig. 2.3 Notation diagram of free-floating dual-arm UVMS

Parallel dynamic modeling of the proposed manipulation methods was obtained by modifying the dynamics equation of the free-floating dual-arm UVMS, thereby making them adhere to constraint equations. Fig. 2.3 depicts the free-floating dual-arm UVMS. The conventional dynamics equation for an underwater vehicle in the body-fixed frame of reference can be written as follows [28]:

$$\mathbf{M}_v\dot{\boldsymbol{v}} + \mathbf{C}_v(\boldsymbol{v})\boldsymbol{v} + \mathbf{D}_v(\boldsymbol{v})\boldsymbol{v} + \boldsymbol{g}_v = \boldsymbol{\tau}_v \tag{2.8}$$

The vector $\boldsymbol{v} = [u,v,w,p,q,r]^{\mathrm{T}}$ denotes the body-fixed vehicle velocity; $\mathbf{M}_v$ represents the inertia matrix with added mass terms of the vehicle; $\mathbf{C}_v(\boldsymbol{v})$ denotes the centrifugal and Coriolis force matrix, which has been neglected in this study owing to low operating speeds of the system. The hydrodynamic drag matrix is denoted by $\mathbf{D}_v(\boldsymbol{v})$; $\boldsymbol{g}_v$ denotes gravity as well as buoyancy vector, which has also been neglected because the system can be considered to maintain neutral buoyancy, since the center of buoyancy and center of mass coincide. $\boldsymbol{\tau}_v$ denotes the thrust force vector of the vehicle. Corresponding terms for the TTURT vehicle have been calculated by the authors in their previous study [9].

Dynamic equation of the underwater manipulator fixed on the ground could be written as follow [28]:

$$\mathbf{M}_m\ddot{\boldsymbol{q}} + \mathbf{C}_m(\boldsymbol{q})\dot{\boldsymbol{q}} + \mathbf{D}_m(\boldsymbol{q})\dot{\boldsymbol{q}} + \boldsymbol{g}_m = \boldsymbol{\tau}_m \tag{2.9}$$

where the vector $\boldsymbol{q}$ denotes the manipulator joint angle vector; $\boldsymbol{\tau}_m$ denotes the manipulator joint torque. All other notations bear the same meanings as in Eq. (2.8).

To put the above equation together, however, interactions between the vehicle and manipulators must be considered. The iterative Newton–Euler dynamics algorithm, reported in Schjoberg's research [28], was employed to put together the above equations, vehicle dynamics, and dynamics of the working and clamping manipulators. After grouping the resulting terms, equations corresponding to each subsystem could be arranged as follows:

$$\mathbf{M}(\boldsymbol{\zeta})\dot{\boldsymbol{\zeta}} + \mathbf{D}(\boldsymbol{q},\dot{\boldsymbol{q}},\boldsymbol{\zeta})\boldsymbol{\zeta} = \boldsymbol{\tau} \tag{2.10}$$

where

$$\mathbf{M}(\boldsymbol{\zeta}) = \begin{bmatrix} \mathbf{M}_v + \mathbf{H}_w(\boldsymbol{q}_w) + \mathbf{H}_c(\boldsymbol{q}_c) & \mathbf{M}_{Cw}(\boldsymbol{q}_w) & \mathbf{M}_{Cc}(\boldsymbol{q}_c) \\ \mathbf{M}_{Cw}{}^{\mathrm{T}}(\boldsymbol{q}_w) & \mathbf{M}_w(\boldsymbol{q}_w) & \mathbf{O} \\ \mathbf{M}_{Cc}{}^{\mathrm{T}}(\boldsymbol{q}_c) & \mathbf{O} & \mathbf{M}_c(\boldsymbol{q}_c) \end{bmatrix} \tag{2.11}$$

$$\mathbf{D}(\boldsymbol{q},\boldsymbol{\zeta}) = \begin{bmatrix} \mathbf{D}_v(\boldsymbol{v}) + \mathbf{D}_{w1} + \mathbf{D}_{c1} & \mathbf{D}_{w2} & \mathbf{D}_{c2} \\ \mathbf{D}_{w3} & \mathbf{D}_w & \mathbf{O} \\ \mathbf{D}_{c3} & \mathbf{O} & \mathbf{D}_c \end{bmatrix} \tag{2.12}$$

Equation (12) represents the dynamic equation of the entire UVMS. The term $\boldsymbol{\zeta} = [\boldsymbol{v}^{\mathrm{T}}, \dot{\boldsymbol{q}}_w{}^{\mathrm{T}}, \dot{\boldsymbol{q}}_c{}^{\mathrm{T}}]^{\mathrm{T}}$ represents the UVMS velocity vector, and subscripts v, w,

and c indicate the involvement of the term with the vehicle, working manipulator, and clamping manipulator, respectively. The term $\mathbf{M}$ represents the inertia matrix including added mass terms, and $\mathbf{D}$ represents the hydrodynamic drag. $\mathbf{H}$ denotes inertia added from a manipulator to the vehicle; $\mathbf{M}_c$ denotes the reaction force and moment induced between a manipulator and vehicle; $\mathbf{D}_i$ indicates quadratic drag terms caused by interactions between the vehicle and manipulators; the vector $\boldsymbol{\tau} = [\boldsymbol{\tau}_v^{\mathrm{T}}, \boldsymbol{\tau}_w^{\mathrm{T}}, \boldsymbol{\tau}_c^{\mathrm{T}}]^{\mathrm{T}}$ is the drive force and torque vector, which comprises vehicle thrust force and joint torques of the two manipulators. The physical terms mentioned on equations (2.11) and (2.12) were obtained in previous research [26]. The manipulator linkages were considered to be of a thin cylindrical shape, terms related to which were calculated.

The body-fixed UVMS dynamic equation could be modified into a parallel dynamic equation. Through application of Cheng's work, constraint equations can be induced from body-fixed dynamics equation [29]. Dynamic equations of the *i*-th manipulation method could, therefore, be derived as follows:

$$\hat{\mathbf{M}}_{\mathrm{M}i}\ddot{\boldsymbol{q}}_{\boldsymbol{u},\mathrm{M}i} + \hat{\mathbf{D}}_{\mathrm{M}i}\dot{\boldsymbol{q}}_{\boldsymbol{u},\mathrm{M}i} = \boldsymbol{\Gamma}_{\mathrm{M}i}\boldsymbol{\tau}_{\boldsymbol{r},\mathrm{M}i} \tag{2.13}$$

$$\hat{\mathbf{M}}_{\mathrm{M}i} = \boldsymbol{\Lambda}_{\mathrm{M}i}^{\mathrm{T}}\mathbf{M}_{\mathrm{M}i}\boldsymbol{\Lambda}_{\mathrm{M}i} \tag{2.14}$$

$$\hat{\mathbf{D}}_{\mathrm{M}i} = \boldsymbol{\Lambda}_{\mathrm{M}i}^{\mathrm{T}}\mathbf{M}_{\mathrm{M}i}\dot{\boldsymbol{\Lambda}}_{\mathrm{M}i} + \boldsymbol{\Lambda}_{\mathrm{M}i}^{\mathrm{T}}\mathbf{D}_{\mathrm{M}i}\boldsymbol{\Lambda}_{\mathrm{M}i} \tag{2.15}$$

Equation (2.13) represents the dynamic equation of the *i*-th manipulation method with respect to its independent joints, $\boldsymbol{q}_{\boldsymbol{u},\mathrm{M}i}$. $\boldsymbol{\Lambda}_{\mathrm{M}i}$ and $\boldsymbol{\Gamma}_{\mathrm{M}i}$ denote constraint Jacobians of the *i*-th manipulation method. $\mathbf{M}_{\mathrm{M}i}$ and $\mathbf{D}_{\mathrm{M}i}$ denote inertia and drag matrices of body-fixed dynamics—equation (2.10). In case of M1, clamping manipulator terms were eliminated, since M1 only comprises the working manipulator; $\boldsymbol{\tau}_{\boldsymbol{r},\mathrm{M}i}$ is the force and torque vector of active joints corresponding to the *i*-th manipulation method.

2.3 Comparison between the methods

2.3.1. Desired trajectory generation

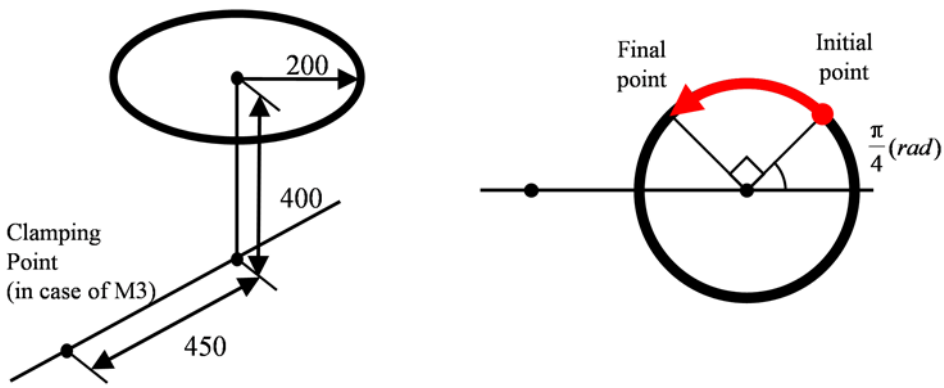

Fig. 2.4 Dimensions of the handle valve and the objective trajectory for comparing manipulation methods

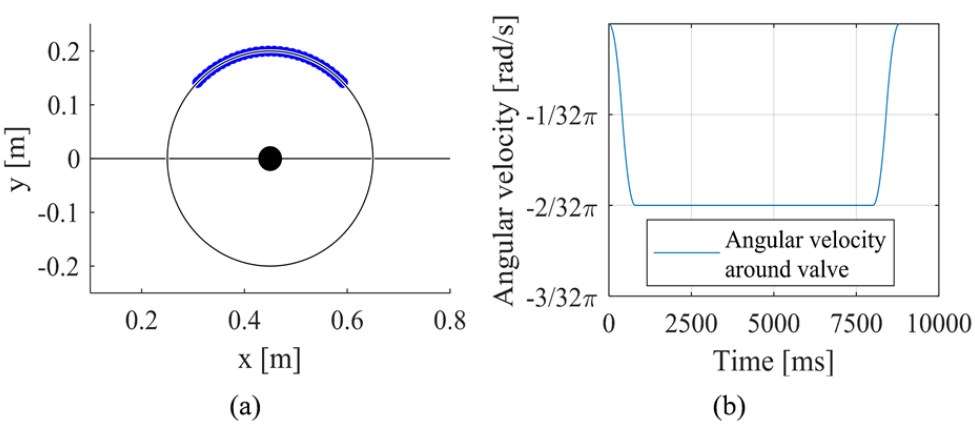

Fig. 2.5 Desired end-effector trajectory with respect to time—(a) Desired end-effector positions at same time interval (30 ms); (b) Desired angular velocity of handle valve q_v; velocity is negative owing to counterclockwise direction.

Fig 2.4 depicts dimensions of the handle valve and the desired valve-turning angle. The objective task was turning the handle-valve through 90 degrees in the counterclockwise direction. The radius of the handle valve was set as 200 mm, and its height from the base was set as 400 mm. In case of M3, the clamping point of the clamping manipulator was set 450 mm away from the base of the handle valve. The initial grabbing point on the handle valve was located 45 degrees counterclockwise from the base pipe. The desired angular velocity profile is depicted in Fig 2.5. A second-order velocity profile was used to obtain the desired trajectory, thereby preventing rapid changes in angular acceleration. The maximum angular speed was set as 1/16π rad/s.

Linkage lengths and initial configuration of the proposed manipulation methods were obtained from the authors' previous work [30]. Table 2.2 lists linkage lengths corresponding to the three manipulation methods. Method M1 do not have clamping manipulator, hence linkage length corresponding to only the working manipulator have been listed. In case of M2, length L_{c3} of the third linkage of the clamping manipulator was extended to have same horizontal length as that of M3, because the height of the clamping point here is different from that in case of M3. Initial configurations of the proposed manipulation methods were set using initial joint-angle results for the working manipulator as well as the position and orientation of the vehicle. Initial joint angles of the clamping manipulator were calculated to fit the configuration, since it possessed a unique solution.

Table 2.2 Linkage lengths for three manipulation methods

Method	L_{w1} (mm)	L_{w2} (mm)	L_{w3} (mm)	L_{c1} (mm)	L_{c2} (mm)	L_{c3} (mm)
M1	350	350	150	N/A	N/A	N/A
M2	350	350	150	382	463	521
M3	350	350	150	382	463	286

Desired joint trajectories of manipulation methods were derived using a generalized inverse method. The entire system contains more actuators compared to the system's DOF, and the number of the independent joints was greater compared to the objective task's DOF. Use of the redundancy resolution method is, therefore, required to determine the desired UVMS trajectory. Desired velocities of independent joints could be derived as follows:

$$\dot{q}_{V,d} = \mathbf{J}_{f,\mathrm{Mi}}\dot{\boldsymbol{q}}_{u,\mathrm{Mi},d} \tag{2.16}$$

$$\dot{\boldsymbol{q}}_{u,\mathrm{Mi},d} = \mathbf{J}_{f,\mathrm{Mi}}{}^{\ddagger}\dot{q}_{V,d} \tag{2.17}$$

where subscript d indicates desired value. $\mathbf{J}_{f,\mathrm{Mi}}{}^{\ddagger}$ denotes the weighted pseudoinverse, which could be mathematically expressed as:

$$\mathbf{J}_{f,\mathrm{Mi}}{}^{\ddagger} = (\mathbf{\Gamma}^{\mathrm{T}}\mathbf{\Gamma})^{-1}(\mathbf{J}_{f,\mathrm{Mi}}(\mathbf{\Gamma}^{\mathrm{T}}\mathbf{\Gamma})^{-1})^{\dagger} \tag{2.18}$$

where superscript (†) is Moore-Penrose pseudoinverse. This trajectory of independent joints is minimizing joint velocity norm of all actuated joints as follows:

$$\min\left\|\dot{\boldsymbol{q}}_{r,\mathrm{Mi},d}\right\|^2 = \min\left\|\mathbf{\Gamma}\dot{\boldsymbol{q}}_{u,\mathrm{Mi},d}\right\|^2 \tag{2.19}$$

which can be achieved by equation (2.17).

2.3.2. Disturbance modeling

Oceanic currents were modeled to simulate disturbance. The speed and direction of oceanic currents were modeled using the first-order Gauss–Markov process [7, 31]. Equations used to obtain the oceanic currents were as follows:

$$\dot{v}_{ocean} + \mu_0 v_{ocean} = w_v(t) \tag{2.20}$$

$$\dot{\theta}_{ocean} + \mu_0 \theta_{ocean} = w_\theta(t) \tag{2.21}$$

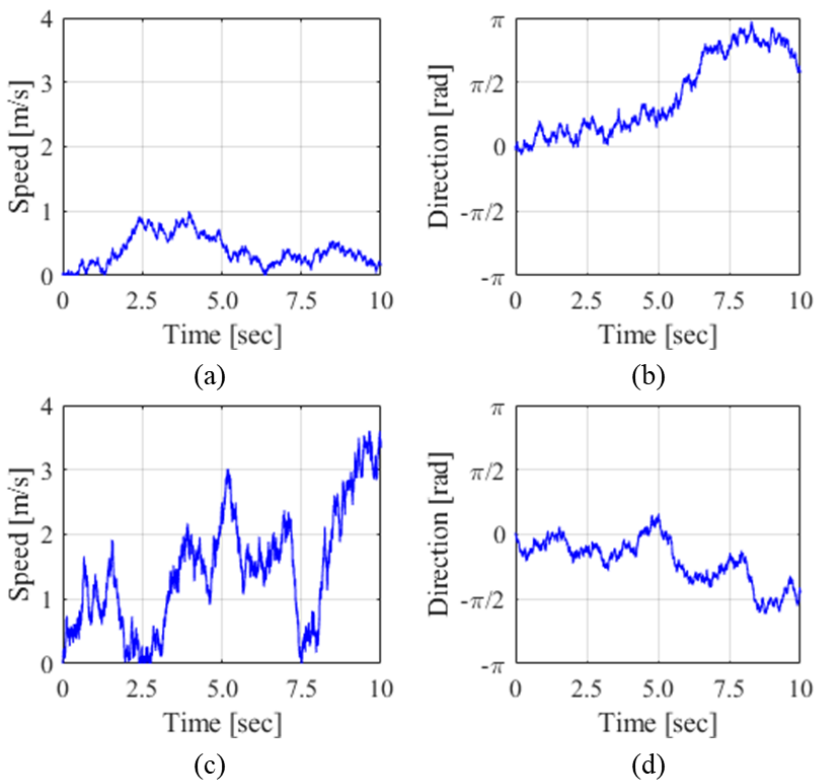

Fig. 2.6 Time histories of oceanic-current models used for simulating the effect of external disturbance—(a) Speed variation in slow oceanic-current model; (b) Direction variation in slow oceanic-current model; (c) Speed variation in fast oceanic current model; (d) Direction variation in fast oceanic-current model.

Terms v_{ocean} and θ_{ocean} in the above equations denote the speed and direction of oceanic currents in the earth-fixed reference frame; $w_v(t)$ and $w_\theta(t)$ denote Gaussian white noise corresponding to the speed and direction of oceanic current; μ_0 is arbitrary constant. Two oceanic current models were considered, as already mentioned. Gaussian white noise power for speed $w_v(t)$ was set as 20 dB and 30 dB for the slow and fast oceanic currents, respectively. The corresponding value of $w_\theta(t)$ was set as 25 dB for both models, and μ_0 was set as 0.001. Fig. 2.6 depicts time histories of speed and direction of the two oceanic-current models.

In the simulation, oceanic currents were considered as additional vehicle velocities [31]. Terms related to hydrodynamic parameters in the dynamic model were function of the relative vehicle velocity with respect to the water. The relative vehicle velocity vector could be obtained by subtracting the oceanic current vector from the vehicle velocity, and substituting this relative velocity term in the hydrodynamic force-related terms yielded the disturbance induced dynamic equation given by:

$$\tilde{\boldsymbol{v}} = \boldsymbol{v} - \boldsymbol{v}_{ocean}^{\{B\}} \tag{2.22}$$

$$\mathbf{M}(\tilde{\boldsymbol{\zeta}})\dot{\boldsymbol{\zeta}} + \mathbf{D}(\boldsymbol{q}, \dot{\boldsymbol{q}}, \tilde{\boldsymbol{\zeta}})\tilde{\boldsymbol{\zeta}} = \boldsymbol{\tau} \tag{2.23}$$

The term $\boldsymbol{v}_{ocean}^{\{B\}}$ denotes the velocity of oceanic currents in the body-fixed reference frame of the vehicle; $\tilde{\boldsymbol{v}}$ denotes the relative velocity with respect to water; and $\tilde{\boldsymbol{\zeta}} = [\tilde{\boldsymbol{v}}^{\mathrm{T}}, \dot{\boldsymbol{q}}_w^{\mathrm{T}}, \dot{\boldsymbol{q}}_c^{\mathrm{T}}]^{\mathrm{T}}$ denotes the UVMS velocity vector with due consideration of relative vehicle velocity. Modifying equation (2.23), the parallel dynamics equation under the influence of oceanic currents could be obtained.

2.3.3. Simulation results and discussions

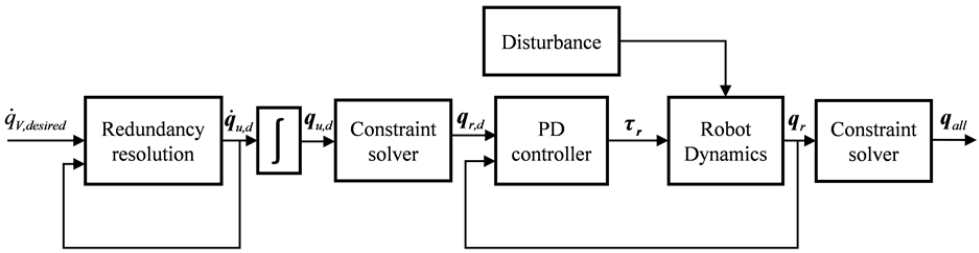

Fig. 2.7 Control diagram for dynamic simulation

With the derived dynamic equation above, simulations of UVMS operation based on the proposed manipulation methods were performed for comparison. Desired trajectories of independent and active joints were derived using the forward and constraint Jacobians, respectively. A PD controller was designed to make the active joints adhere to desired trajectories in accordance with the following equation:

$$\boldsymbol{\tau}_{r,\mathrm{M}i} = (\boldsymbol{\Gamma}^{\mathrm{T}})^{+}(\mathbf{K}_{P,\mathrm{M}i}\boldsymbol{e}_{\mathrm{M}i} - \mathbf{K}_{D,\mathrm{M}i}\dot{\boldsymbol{e}}_{\mathrm{M}i}) \tag{2.26}$$

where $\boldsymbol{e}_{\mathrm{M}i} = \boldsymbol{q}_{u,\mathrm{M}i,d} - \boldsymbol{q}_{u,\mathrm{M}i}$ represents the error in independent joints of the *i*-th manipulation method, and $\mathbf{K}_{P,\mathrm{M}i}$ and $\mathbf{K}_{D,\mathrm{M}i}$ denote controller gains. Values of controller gains for each manipulation method are listed in Table 2.3. The term $\mathrm{diag}(*)$ refers to a diagonal matrix comprising elements $(*)$. Fig. 2.7 depicts the simulation control diagram.

Table 2.3 PD controller gain values for each method

Method	$\mathbf{K}_P$	$\mathbf{K}_D$
M1	diag([2000,2000,2000,300])	diag([1.5k,1.5k,1.5k,1k])
M2	diag([150,150,150])	diag([5k,5k,5k])
M3	diag([100,100,100])	diag([100,100,100])

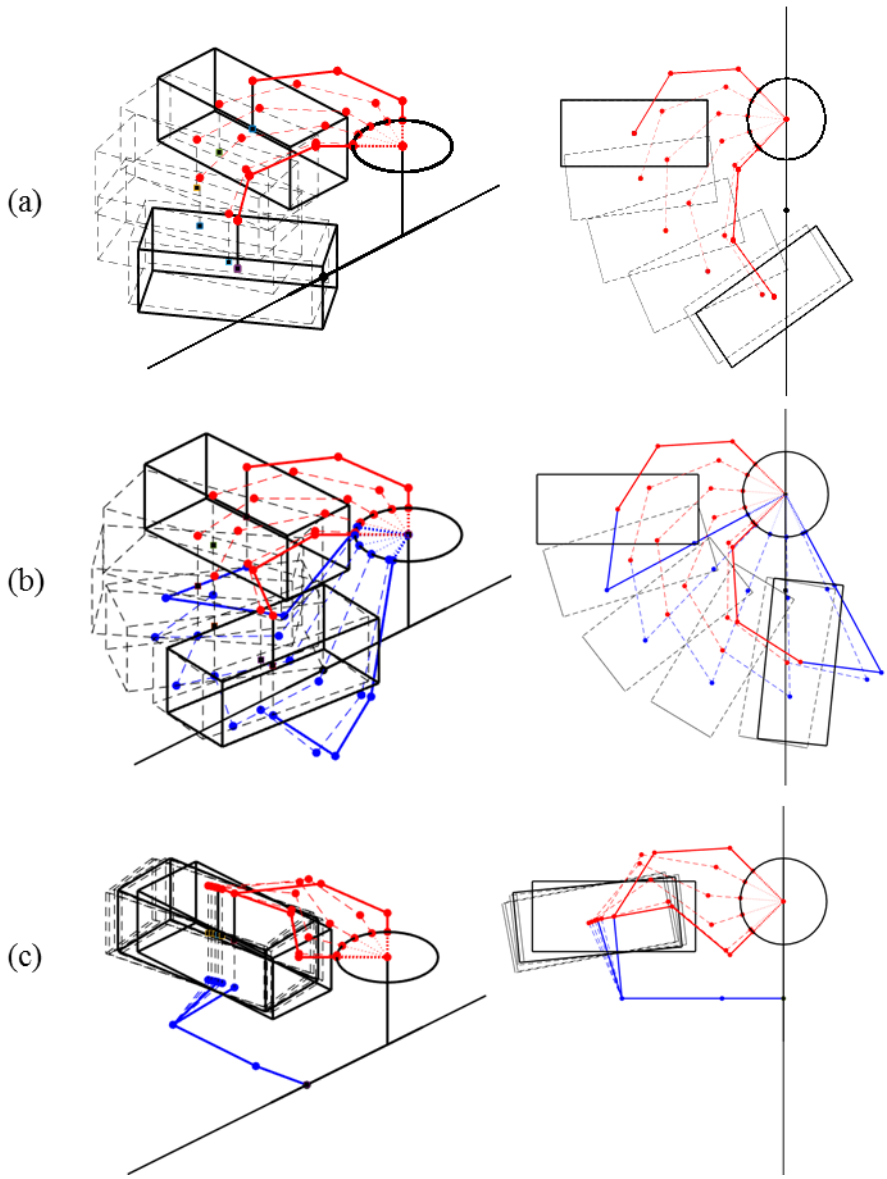

Fig. 2.8 Desired trajectories of the three manipulation methods derived by using the kinematics equation. Initial and final configurations are depicted using thick lines. Red and blue lines denote linkages of the working and clamping manipulators. The vehicle is presented by the black-colored box shape. (a) Vehicle trajectory in method M1; (b) Vehicle trajectory in method M2; and (c) Vehicle trajectory in method M3.

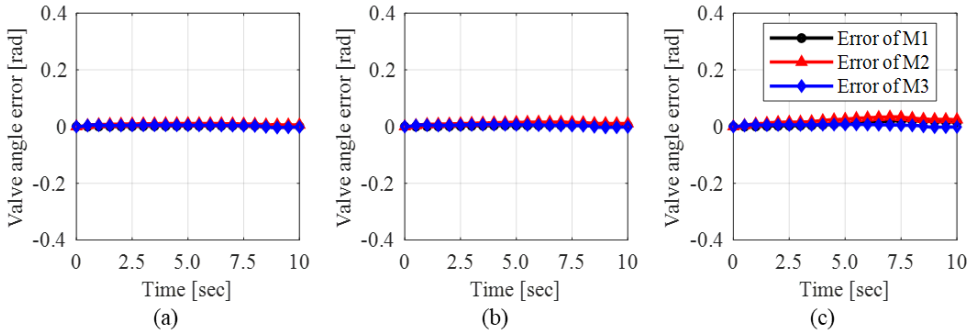

Fig. 2.9 The error of the handle valve angle trajectory. The black line indicates the error of the method M1, and the red line is the error of the method M2. The error of M3 is drawn as blue line. (a) Error graph without disturbance; (b) Error graph under slow oceanic current; (c) Error graph under fast oceanic current.

Simulations of the handle valve turning operation were performed for the three proposed manipulation methods, and obtained results were subsequently analyzed. All simulations were programed in MATLAB Simulink, and simulation length was set as ten seconds; the sampling time was set as 1 ms. Fig. 2.8 depicts desired trajectories of the three manipulation methods derived using the kinematic equation. In each case, the vehicle demonstrates only two-dimensional motion on the x–y plane owing to limitations imposed by constraint equations. In cases M1 and M2, the vehicle moves a large distance around the handle valve, since valve turning is the primary task to be performed by the vehicle. In the case of M3, however, the vehicle covers a relatively short distance compared to the other two methods. This is because the working manipulator can turn the valve handle owing mainly to the fixed end of the clamping manipulator. Fig. 2.9 shows the trajectory error of three cases. The errors of three cases were bounded to nearly zero. Due to the disturbance, the error is not completely zero. There were no meaningful differences on the valve angle error between three manipulation methods.

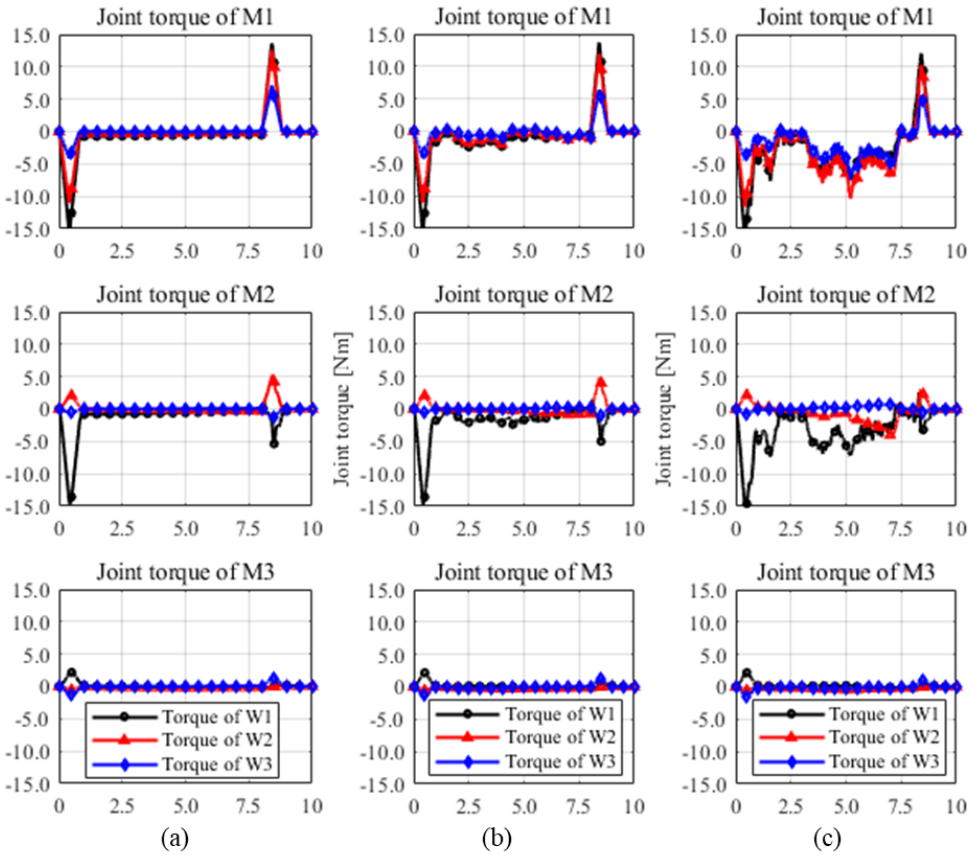

Fig. 2.10 Time histories of the joint torques of the working manipulator. The torque at joint W1, which is closest to the vehicle, is indicated by black line. The red line describes torque at joint W2, and blue line indicates torque at joint W3, the last joint of working manipulator. (a) Working manipulator torque without disturbance; (b) Working manipulator torque under slow oceanic currents; (c) Working manipulator torque under fast oceanic currents.

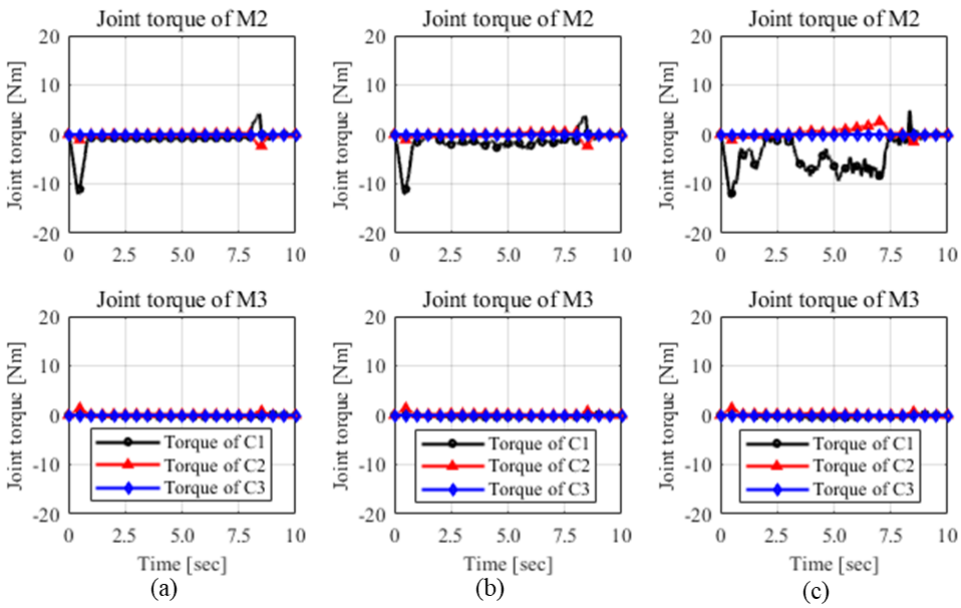

Fig. 2.11 Time histories of joint torque at clamping manipulator. Black line denotes joint torque of C1 joint located closest to the vehicle. Red and blue lines similarly denote torques developed at the C2 and C3 joints. (a) Joint torque of clamping manipulator without disturbance; (b) Joint torque of clamping manipulator under slow oceanic currents. (c) Joint torque of clamping manipulator under fast oceanic currents.

Time histories of the joint torque of the working manipulator when using methods M1, M2 and M3 are depicted in Fig. 2.10 while Fig. 2.11 depicts corresponding time histories of the joint torque of the clamping manipulator. Among the three manipulation methods, M3 demonstrates generation of the smallest torque at the working manipulator while M2 generated larger torque than M3. M1 showed the largest torque values between three manipulation methods. Owing to high speed movement of the vehicle, working manipulators of methods M1 and M2 are required to withstand vehicle–water interactions and drag forces, and corresponding results for the clamping manipulator demonstrate similar tendencies. The M3 method demonstrates a smaller value of the clamping

manipulator joint torque compared to M2. Under presence of oceanic curret, manipulator linkages were subjected to drag forces caused by oceanic current. Owing to the reaction force generated at the clamping manipulator in M3, the additional force required for compensating the disturbance can be reduced. Thus, when oceanic currents were applied to UVMS, the observed wobbling of manipulator torque was small in case of M3.

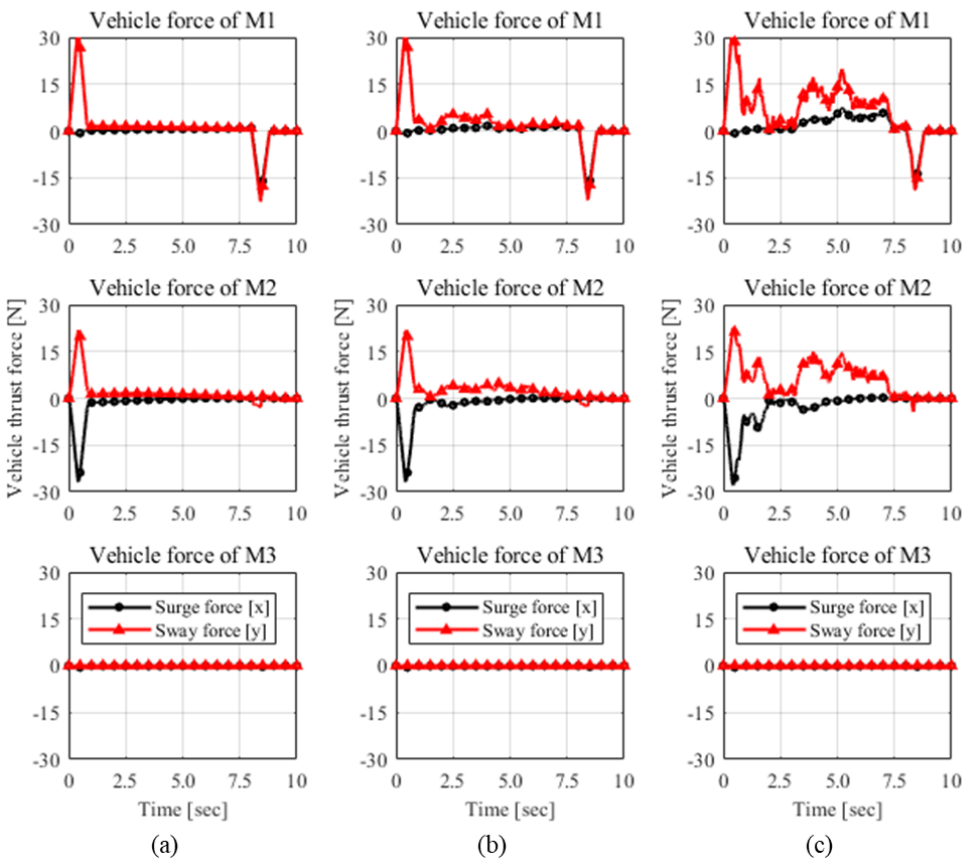

Fig. 2.12 Trends in vehicle thrust force observed during underwater operation. The sway and surge (i.e., x- and y-components of the thrust force) force components are denoted by black and red curves. (a) Trends in thrust force without disturbance; (b) Trends in thrust force under slow oceanic currents; (c) Trends in thrust force under fast oceanic currents.

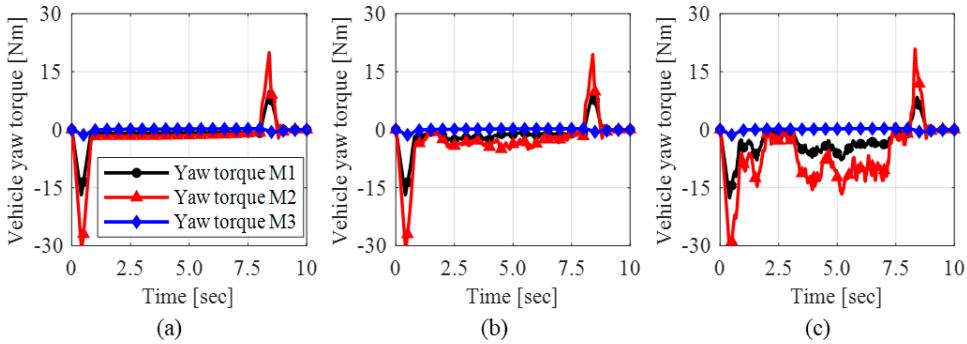

Fig. 2.13 The yaw torque of the vehicle thrust. The black line indicates the yaw torque of the method M1, and the red line is that of the method M2. The yaw torque of M3 is drawn as blue line. (a) Yaw torque without disturbance; (b) Yaw torque under slow oceanic current; (c) Yaw torque under fast oceanic current.

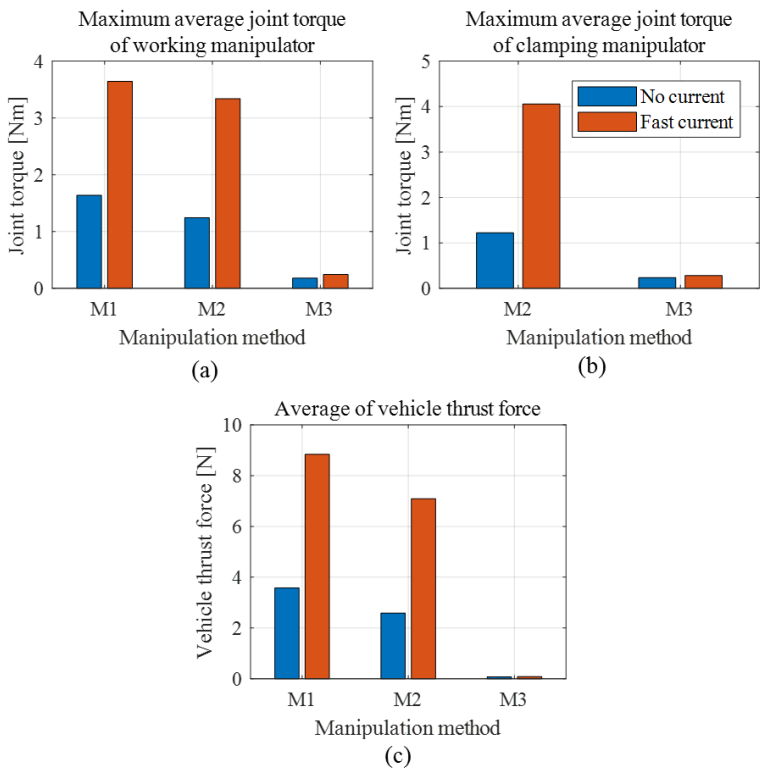

Fig. 2.14 Summary of the results—(a) Maximum average joint torque of working manipulator; (b) Maximum average joint torque of clamping manipulator; (c) Average of vehicle thrust force vector size.

Figure 2.12 depicts time histories of the vehicle thrust force while Fig. 2.13 depicts corresponding trends in vehicle yaw torque. The vehicle thrust along x and y directions and yaw torques were analyzed because the vehicle demonstrated two-dimensional motion in the x–y plane. Owing to the large movement of the vehicle, the thrust force and yaw torques involved in methods M1 and M2 were observed to be significantly larger compared to those involved in M3. Moreover, under the influence of oceanic currents, the level of thrust wobble was observed to be much larger when employing methods M1 and M2. This is natural, because the vehicle, in these methods, is required to handle all forces induced by oceanic currents. When clamped onto the surrounding environment, the joint torque at the manipulator could also be used to compensate for external disturbance. Therefore, in case of M3, the required vehicle thrust force is significantly reduced.

In all cases, the valve angle error, joint torque, and vehicle thrust force were observed to have increased under the influence of oceanic currents. Fig. 2.14 shows the summary of the simulation results. The M3 method demonstrates smallest values of the average joint torque, and vehicle thrust force with respect to time. The main reason behind these trends is the existence of the reaction force generated at the end-effector of the clamping manipulator in M3. Without clamping on the environment, vehicles forces are mainly used for valve turning and compensating for the underwater disturbance, thereby leading to generation of driving manipulator torques and vehicle thrust forces. Therefore, use of the M3 manipulation method yields efficient results, especially under disturbance, such as those caused by oceanic currents. The major problem associated with the use of M3 lies in searching for an appropriate environment near the workspace, which must be resolved prior to applying the M3 method in actual UVMS operations.

Chapter 3. Design a structure of the dual-arm manipulator

3.1. Design alternatives of the dual-arm manipulator

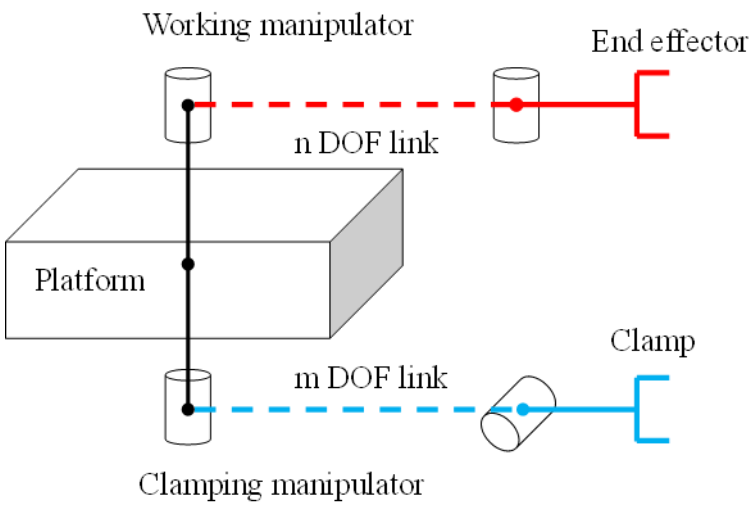

Fig. 3.1 Distribution of DOF between a clamping manipulator and a working manipulator

In previous chapter, the dual-arm manipulation with clamping was selected as a manipulation method for the UVMS. The dual-arm manipulator consists of two parts. The first part of the manipulator is a clamping manipulator. The clamping manipulator is used to anchor the entire system on a fixed point. In a manner similar to that of a human diver, the UVMS can achieve a desired task under strong disturbance by holding a point. The second part of the manipulator corresponds to a working manipulator. The working manipulator consists of an end-effector to perform specific tasks. It is necessary to design each part of a dual-arm manipulator in conjunction with each other.

All the DOFs of a dual-arm manipulator were defined to determine the configuration of a dual-arm manipulator. A few tasks require a three-dimensional trajectory of the end-effector. Three DOF on a plane corresponds to the minimal DOF that is necessary to achieve full planar motion. However, the addition of an extra DOF in the plane makes the manipulator redundant, and thus it can simultaneously perform various tasks. Furthermore, the changing of the working plane can be a solution to ensure that a task is performed with ease. Therefore, an additional DOF is added to incline the working plane. Hence, the dual-arm manipulator was determined to have 5-DOF, four of which is on the working plane and rest of which is assigned to be able to move the working plane.

The configuration of the dual-arm manipulator is determined by dividing DOFs between two arms. Fig. 3.1 describes the constraints of dividing DOFs. It is necessary to attach two arms to the top and the bottom and to ensure that the two joints are in the same line. Thus, the system requires an additional joint. The problem is simplified by including 1 DOF that inclines the working plane at the end of the clamping manipulator. It is possible to deploy planar 4 DOFs on both arms of the manipulator. Therefore, the number of the joints was set as six. Design alternatives of the dual-arm manipulator can be made by assigning six rotation joints to the two manipulators. Fig. 3.2 shows the proposed design alternatives of a dual-arm manipulator. Revolute joints in the x direction and z direction are used for inclining the working plane and for performing planar motion, respectively.

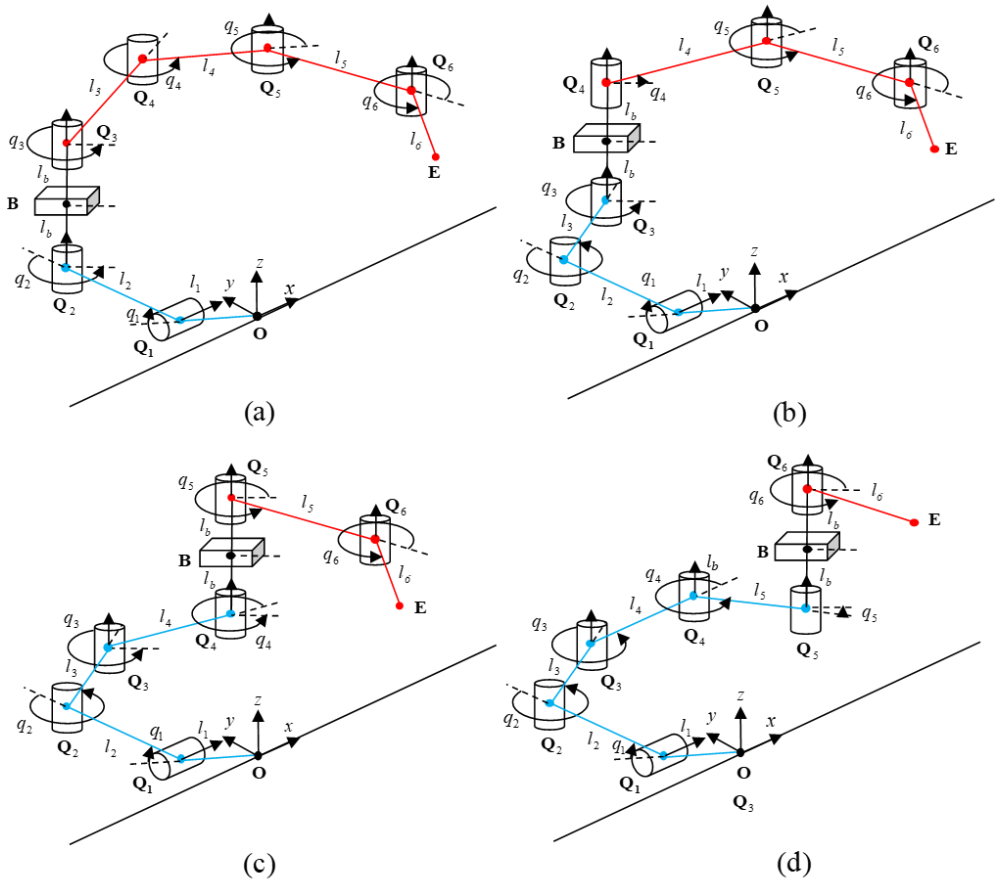

Fig. 3.2 Design alternatives of the dual-arm manipulator. Each alternative is created by deploying revolute joints—(a) Design alternative #1 (A1), 1 joint on clamping, 4 joints on the working manipulator; (b) Design alternative #2 (A2), 2 joints on clamping, 3 joints on the working manipulator; (c) Design alternative #3 (A3), 3 joints on clamping, 2 joints on the working manipulator; (d) Design alternative #4 (A4), 4 joints on clamping, 1 joint on the working manipulator.

While anchored on a fixed point, the whole system can be considered as a serial manipulator with six revolute joints. Configurations and notations of the alternatives are shown in Fig. 3.2. The vehicle with its position indicated by B was considered as a part of a linkage. Origins of the alternatives are defined at the end of the clamping manipulator O, and the end-effectors of the alternatives are denoted as E. The position of the *i*-th joint is denoted as $\mathbf{Q}_i$ while the joint angle of *i*-th joint is expressed as q_i. Additionally, l_i indicates the length of the *i*-th horizontal linkage, and l_b denotes the length of the linkage attached to the vehicle.

Kinematics of each alternative were solved to determine the position of the end-effector as a function of the joint angle vector $\boldsymbol{\theta}$. The position of the end-effector was calculated by using screw theory [29]. By multiplying exponent of the twists of each joint, we could obtain the position of the end-effector with respect to the joint angles. The velocities of end-effectors were determined by differentiating the end-effector position with respect to time. The velocities of end-effectors were expressed in the form of a Jacobian matrix as follows:

$$\dot{\boldsymbol{x}}_e = \mathbf{J}(\boldsymbol{\theta})\dot{\boldsymbol{\theta}} \tag{3.1}$$

3.2. Optimization of each alternative

3.2.1. Cost function for optimization

Dynamic manipulability was selected as an indicator to determine the performance of each design alternative. Dynamic manipulability is used for applying dynamic properties to verify the performance of the alternatives. The following section describes the addition of hydrodynamic terms to dynamic manipulability. Dynamic equations of the alternatives are summarized as follows:

$$\mathbf{M}(\boldsymbol{\theta})\ddot{\boldsymbol{\theta}} + \mathbf{D}(\boldsymbol{\theta},\dot{\boldsymbol{\theta}})\dot{\boldsymbol{\theta}} = \boldsymbol{\tau} \tag{3.2}$$

where $\mathbf{M}(\boldsymbol{\theta})$ denotes the inertia matrix that includes the added mass terms, and $\mathbf{D}_i(\boldsymbol{\theta},\dot{\boldsymbol{\theta}})$ denotes the hydrodynamic damping matrix. The term $\boldsymbol{\tau}$ is joint torque vector. The kinematic equation of the alternatives (3.1) is differentiated with respect to time to obtain the following expression:

$$\dot{\boldsymbol{v}} = \mathbf{J}\ddot{\boldsymbol{\theta}} + \dot{\mathbf{J}}\dot{\boldsymbol{\theta}} \tag{3.3}$$

The velocity of the end-effector is expressed as $\boldsymbol{v}$. Additionally, new vectors $\tilde{\boldsymbol{\tau}}$ and $\dot{\tilde{\boldsymbol{v}}}$ are introduced, and torque and the end-effector velocity can be indicated as follows:

$$\tilde{\boldsymbol{\tau}} = \boldsymbol{\tau} - \mathbf{D}(\boldsymbol{\theta},\dot{\boldsymbol{\theta}})\dot{\boldsymbol{\theta}} \tag{3.4}$$

$$\dot{\tilde{\boldsymbol{v}}} = \dot{\boldsymbol{v}} - \dot{\mathbf{J}}\dot{\boldsymbol{\theta}} \tag{3.5}$$

The term $\dot{\boldsymbol{v}}$ is the acceleration of the end-effector. $\dot{\tilde{\boldsymbol{v}}}$ denotes the acceleration of the end-effector without virtual acceleration $\dot{\mathbf{J}}\dot{\boldsymbol{\theta}}$. $\tilde{\boldsymbol{\tau}}$ is the joint torque vector after overcoming hydrodynamic drag effect $\mathbf{D}(\boldsymbol{\theta},\dot{\boldsymbol{\theta}})\dot{\boldsymbol{\theta}}$. The idea of dynamic

manipulability involves determining the variability of the end-effector acceleration with respect to the joint torque $\boldsymbol{\tau}$ [32]. Equations (3.2), (3.3), (3.4), and (3.5) are combined to obtain the following expression:

$$\dot{\tilde{\boldsymbol{v}}} = \mathbf{J}\mathbf{M}^{-1}\tilde{\boldsymbol{\tau}} \tag{3.6}$$

With respect to the relation between $\tilde{\boldsymbol{\tau}}$ and $\dot{\tilde{\boldsymbol{v}}}$ in Equation (3.6), the variability of acceleration under a joint torque constraint is measured by using dynamic manipulability w_d as follows:

$$w_d = \sqrt{\det(\mathbf{J}(\mathbf{M}^{\mathrm{T}}\mathbf{M})^{-1}\mathbf{J}^{\mathrm{T}}} \tag{3.7}$$

However, it is necessary to normalize the joint torque vector in (14) because the maximum joint torque varies with respect to the configuration and velocity. Thus, the *i*-th component of normalized joint torque $\hat{\tau}_i$ is defined as follows:

$$\hat{\tau}_i = \tilde{\tau}_i / \tilde{\tau}_{i0}(\boldsymbol{\theta}, \dot{\boldsymbol{\theta}}) \tag{3.8}$$

where

$$\tilde{\tau}_{i0}(\theta, \dot{\theta}) = \tau_{i0} - \left|\mathbf{D}(\boldsymbol{\theta}, \dot{\boldsymbol{\theta}})\dot{\boldsymbol{\theta}}\right|_i \tag{3.9}$$

$\tilde{\tau}_{i0}(\boldsymbol{\theta}, \dot{\boldsymbol{\theta}})$ denotes the rest of the maximum joint torque after overcoming hydrodynamic damping effects. The constant τ_{i0} denotes the maximum joint torque of the *i*-th joint. The term $\left|\mathbf{D}(\boldsymbol{\theta}, \dot{\boldsymbol{\theta}})\dot{\boldsymbol{\theta}}\right|_i$ represents the *i*-th component of results that multiplies the drag matrix with the joint velocity vector. To normalize

maximum joint torque to 1, The joint torque without damping effect, $\tilde{\boldsymbol{\tau}}$ should be divided with $\tilde{\tau}_{i0}(\boldsymbol{\theta}, \dot{\boldsymbol{\theta}})$. There is no difference in acceleration weighting, and thus it is not necessary to normalize the end-effector acceleration. Therefore, normalized end-effector velocity is obtained as follows:

$$\hat{v}_j = \tilde{v}_j \tag{3.10}$$

Substituting Eq. (15) and Eq. (17) into Eq. (13) results in the following expression:

$$\dot{\hat{\boldsymbol{v}}} = \mathbf{J}\hat{\mathbf{M}}^{-1}\hat{\boldsymbol{\tau}} \tag{3.11}$$

where

$$\hat{\mathbf{M}} = diag[1/\tilde{\tau}_{i0}]\mathbf{M} \tag{3.12}$$

The term $diag(*)$ denotes the diagonal matrix with the elements of $(*)$. An approach similar to that specified in the above paragraph is adopted, and thus dynamic manipulability with respect to the normalized joint torque is expressed as follows:

$$\hat{w}_d = \sqrt{\det(\mathbf{J}(\hat{\mathbf{M}}^{\mathrm{T}}\hat{\mathbf{M}})^{-1}\mathbf{J}^{\mathrm{T}}} \tag{3.13}$$

The cost function of the optimization is given by the integration of dynamic manipulability with respect to the operating time. Only the x and y directions are considered since the desired task is planar. Therefore, dynamic manipulability is calculated by a Jacobian only with respect to the x and y direction terms as follows:

$$F = \int \hat{w}_d \, dt \tag{3.14}$$

3.2.2. Optimization problem definition

Modified dynamic manipulability was selected as an index to measure the performances of the alternatives. The manipulability corresponds to a function of joint angles and link lengths, and thus it is necessary to optimize the alternatives to include maximum manipulability in their configurations. Therefore, it is necessary to optimize the link lengths of the alternatives. Additionally, modified dynamic manipulability is influenced by the joint trajectory, and therefore it is important to carefully select the joint trajectory to maximize manipulability of a specific configuration.

As previously mentioned, turning the handle valve is designated as the desired task. Fig. 2.4 shows the desired end-effector trajectory of the objective task. The handle valve lies on the *xy*-plane. The distance from the clamping point to the handle valve base was set as 450 mm, the height of the valve is set as 200 mm, and the radius of valve was set as 200 mm. The desired rotation velocity of the valve was also specified. Fig. 2.5 shows the desired of the end-effector trajectory and the desired angular velocity profile of the valve. A second order profile was used to prevent rapid changes in acceleration. The maximum angular speed was set as 1/16π rad/s.

A joint trajectory generation algorithm is required to calculate the optimization function because the link lengths of the alternatives correspond to the design optimization parameters. A gradient projection method was used to determine a joint trajectory that maximizes a cost function. The alternatives include an additional DOF in the *xy*-plane, and thus the null space was used to determine a trajectory that maximizes dynamic manipulability. A kinematic equation of the alternatives (3.1) was used to describe a null space equation as follows:

$$\dot{\boldsymbol{\theta}} = \mathbf{J}^{\dagger}\dot{\boldsymbol{x}}_e + (\mathbf{I} - \mathbf{J}^{\dagger}\mathbf{J})\dot{\boldsymbol{\theta}}_0 \tag{3.15}$$

where $\mathbf{J}^{\dagger}$ denotes the Moore-Penrose generalized inverse of a Jacobian matrix as follows:

$$\mathbf{J}^{\dagger} = \mathbf{J}^{\mathrm{T}}(\mathbf{J}\mathbf{J}^{\mathrm{T}}) \tag{3.16}$$

The arbitrary function $\dot{\boldsymbol{\theta}}_0$ was set as follows:

$$\dot{\boldsymbol{\theta}}_0 = k(\frac{\partial F}{\partial \boldsymbol{\theta}})^T \tag{3.17}$$

The integration of dynamic manipulability F was maximized with respect to the trajectory. In this problem, the constant *k* in equation (3.17) was set as -0,0005 to maximize the total dynamic manipulability. The desired end-effector velocity was already known, and the joint trajectory of the alternatives was generated by integrating equation (3.15) with respect to time. Initial positions were determined by solving for the inverse kinematics of the alternatives. It was necessary to fix at least one joint angle to determine the initial condition due to the redundancy. The first angle of a revolute joint in the z-direction was selected to design parameters to set the initial joint trajectory. Due to the kinematic structure of the design alternatives, in case of A1, q_3 was selected as the additional design parameter. In case of the others, q_2 was selected as the additional design parameter.

The optimization constraints were set as follows. The length of links attached to TTURT was specified as 225 mm because the module connectors are located on the top and the bottom of the TTURT. The lengths of other links were specified in the range of 350 mm to 500 mm given the issue in placing internal parts such as motors, motor drivers, and electrical parts. The length of end links of the clamping manipulator and working manipulator were specified in range of 150 mm to 300 mm due to size limitations of end-effector and internal parts. The specified length of the geared motor candidate, Maxon DC RE30 with planetary gear, corresponds

to 111 mm. In addition, the initial joint angle was specified in certain ranges to ensure that the initial configuration is reasonable. The constraints for optimizing each alternative are listed in Table 3.1.

Table 3.1 Optimization constraints of the design parameters

Parameter	Optimization constraints
l_b (mm)	$l_b = 225$
l_1, l_6 (mm)	$150 \le l_1, l_6 \le 300$
l_2, l_3, l_4, l_5 (mm)	$350 \le l_2, l_3, l_4, l_5 \le 500$
Joint angle (rad)	$3/2\pi \le q_2 \le 2\pi$ $(1/2\pi \le q_3 \le \pi$ for A1)

A genetic algorithm was selected as the optimization algorithm. Genetic algorithm is a widely known algorithm to determine the global maximum of a cost function. The genetic algorithm function in Global Optimization Toolbox of MATLAB was used to optimize each alternative. The population size was set as 200, and the crossover fraction was set as 0.8. The Gaussian mutation was set as mutation function. The optimization scheme is described in Fig. 3.3.

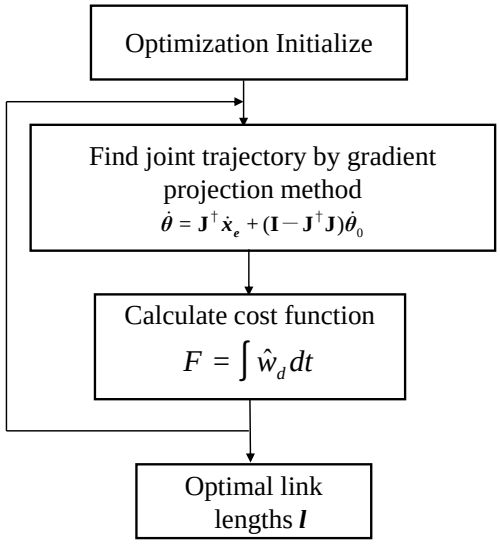

Fig. 3.3 Optimization schematics

3.3. Selection of the design for the dual-arm manipulator

The design alternatives presented in the previous section were optimized to maximize the total dynamic manipulability through operation. Inertia and hydrodynamic terms of TTURT were applied to compute the dynamics of the alternatives. All linkages were considered as equivalent to a cylinder with a radius corresponding to 50 mm. The mass of each of the linkages was set as 1 kg. It is assumed that the center of mass of a linkage is located at the center of the linkage. Hydrodynamic damping and added mass terms were calculated by assuming that the shape of the linkages corresponds to that of a thin cylinder as mentioned in the previous section. The maximum torque of all the joints is set as 15 Nm each. The maximum torque of joints was selected by available DC motor candidates [33].

Linkage lengths and initial trajectories of the alternatives were set as the design parameters and optimized. Table 3.2 lists the optimization results of the design alternatives. Joint angle q_2 (in case of A1, q_3) defines the initial configuration of the alternatives. Dynamic manipulability of the optimized alternatives during operation is presented in Fig. 3.4

Table 3.2 Optimized design parameters of the alternatives

Design	l_1 (mm)	l_2 (mm)	l_3 (mm)	l_4 (mm)	l_5 (mm)	l_6 (mm)
A1	150	351	499	350	350	150
A2	300	500	350	350	350	150
A3	157	355	407	492	351	151
A4	189	394	434	416	395	151

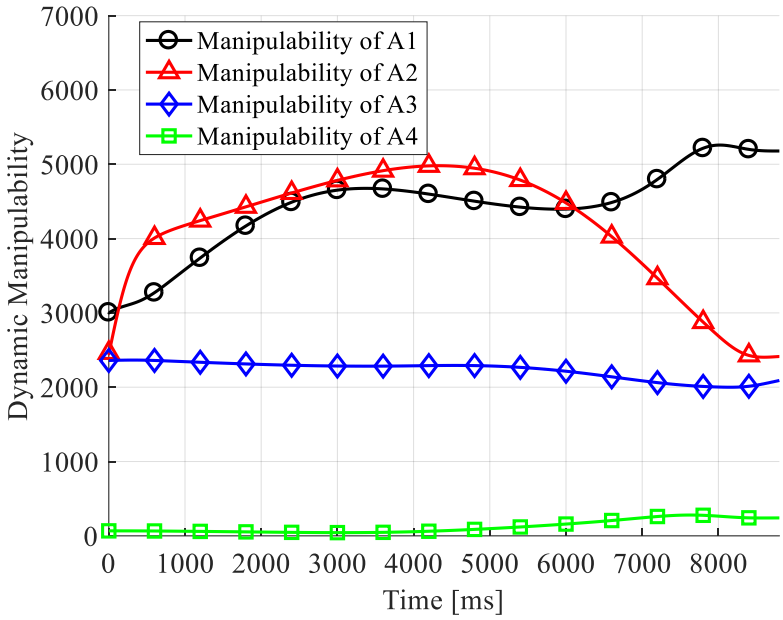

Fig. 3.4 Dynamic manipulability with respect to operation time

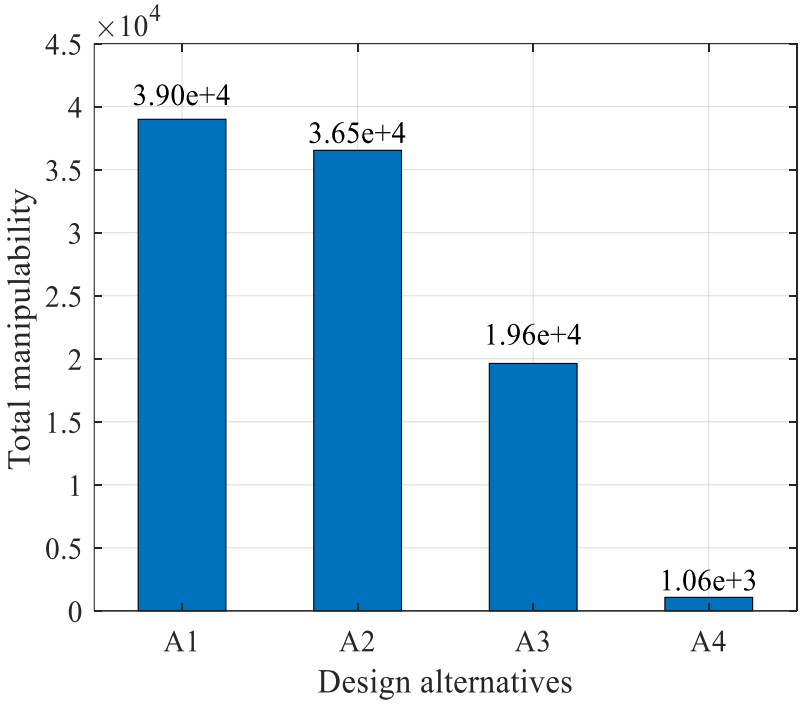

Fig. 3.5 Total dynamic manipulability during operation time

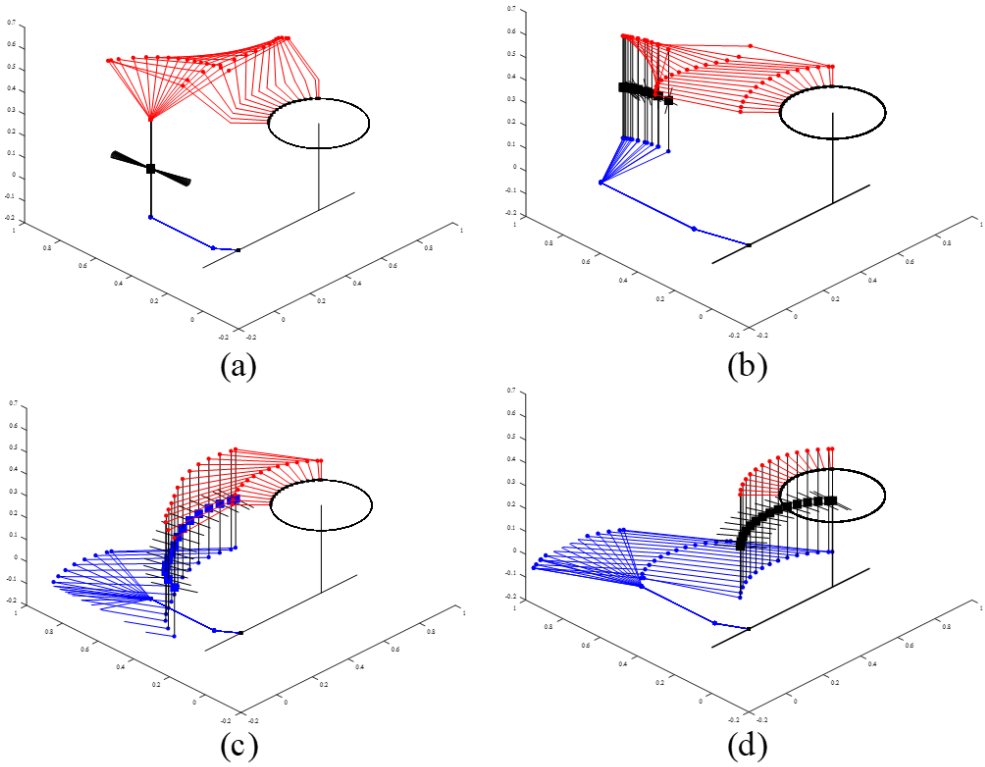

Fig. 3.6 Joint trajectories of the optimized alternatives. Joint positions are denoted as dots. The black square denotes the position of TTURT. The black line passing through the square indicates the direction of TTURT. Linkages expressed as blue lines are parts of the clamping manipulator. Linkages expressed as red lines are parts of a working manipulator. The axes are representing the distance from the orientation in meters. (a) Joint trajectory of A1; (b) Joint trajectory of A2; (c) Joint trajectory of A3; (d) Joint trajectory of A4.

As shown in Fig. 3.5, A1 and A2 exhibit a significantly high value of total dynamic manipulability when compared to those of other alternatives. The difference between total dynamic manipulability of A1 and A2 was too low to determine the optimal alternative. Additionally, the total dynamic manipulability of A3 corresponds to approximately half that of A1 and A2 each. The total dynamic manipulability of A4 is extremely low compared to those of the other alternatives.

Dynamic manipulability is influenced by inertia and hydrodynamic damping of linkages. The alternatives contain the vehicle between two linkages. Dynamic manipulability of the alternatives is significantly influenced by position and velocity of the vehicle because the vehicle has a significantly high amount of inertia, added mass, and hydrodynamic damping when compared with the other linkages. The high velocity of the vehicle decreases the dynamic manipulability of the alternatives because of the high amounts of hydrodynamic damping force generated by the vehicle. The high acceleration of the vehicle also reduces dynamic manipulability because of the high inertia and added mass of the vehicle.

Fig. 3.6 shows the joint trajectory of each alternative with respect to the valve rotating task. Fig. 3.7 presents a two-dimensional view of joint trajectories. Evidently, movement and velocity of the vehicle in A1 and A2 are lower than those in A3 and A4. It is not possible for the vehicle to move during the task due to the A1 configuration. In case of A2, it is necessary for the vehicle to move to achieve the desired trajectory. However, the results indicated that the joint trajectory that minimized movement and velocity of the vehicle corresponded to the gradient projection method. Specifically, it is important for the vehicle to move by a significant distance with respect to high speed in the case of A3 and A4 because the position of the vehicle is close to the end-effector. However, movement and velocity of the vehicle are limited in achieving the desired end-effector trajectory due to the close distance from the end-effector. Therefore, the findings indicate that the performances of A1 and A2 exceed those of the other alternatives since they exhibit a higher amount of total dynamic manipulability.

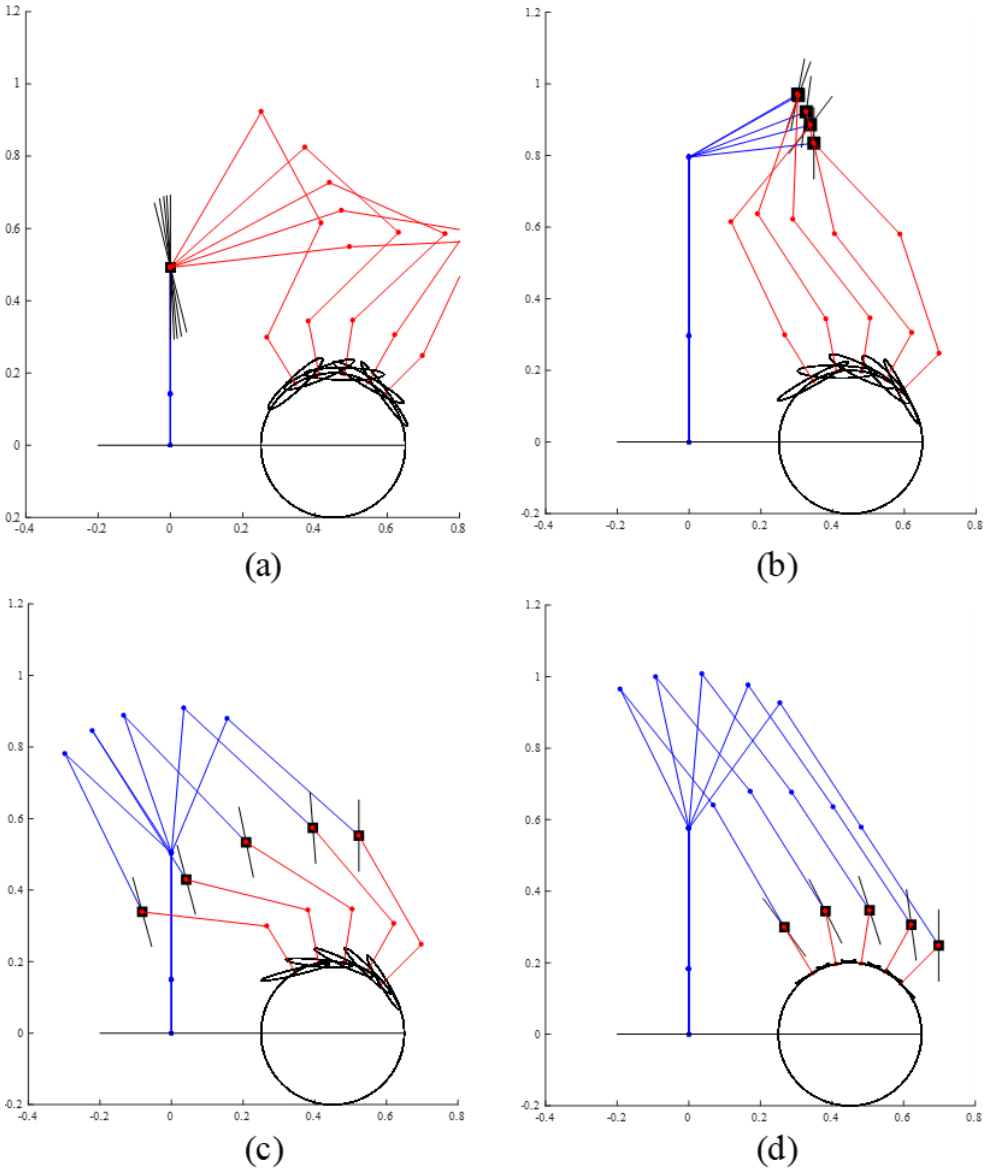

Fig. 3.7 Dynamic manipulability ellipse of optimized alternatives with respect to workspace—(a) A1, (b) A2, (c) A3, (d) A4.

The optimized alternatives were compared with each other. The findings indicated that alternatives A1, which has four joints on the working manipulator, and A2, which has three joints for each manipulator, exhibited a higher performance as compared to those of the other alternatives. Design alternative A2 was selected for optimal design for valve turning UVMS. Although dynamic manipulability of A2 is not the highest among the alternatives, the difference of dynamic manipulability between A1 and A2 is small and alternative A1 cannot use vehicle's force and torque to help manipulator due to constraints.

Chapter 4. Cooperative manipulation method

4.1. Modeling of the UVMS

4.1.1. Kinematics modeling

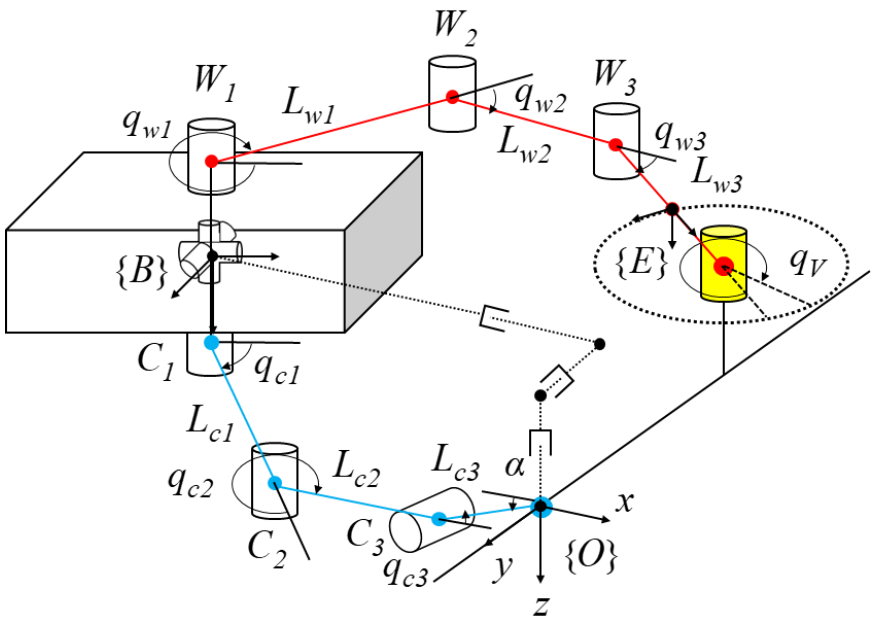

Fig. 4.1 Kinematics diagram of the dual-arm UVMS

The basics of modeling of UVMS was once derived at the chapter 2. The final version of kinematic and dynamic modeling was confirmed for optimal dual-arm UVMS. Fig 4.1 shows the kinematic diagram of the system, and Table 4.1 presents the final length of linkages. The lengths of linkages were slightly changed from optimal value due to design issues.

Table 4.1 Linkage lengths of the UVMS

L_{w1} (mm)	L_{w2} (mm)	L_{w3} (mm)	L_{c1} (mm)	L_{c2} (mm)	L_{c3} (mm)
350	350	288	382	463	423

Table 4.2 Joint classification from parallel manipulator modeling

Independent Joints	Active Joints	All Joints
$\boldsymbol{q}_w$	$[\boldsymbol{\eta}^{\mathrm{T}}, \boldsymbol{q}_w{}^{\mathrm{T}}, \boldsymbol{q}_c{}^{\mathrm{T}}]^{\mathrm{T}}$	$[\boldsymbol{\eta}^{\mathrm{T}}, \boldsymbol{q}_w{}^{\mathrm{T}}, \boldsymbol{q}_c{}^{\mathrm{T}}, q_V]^{\mathrm{T}}$

The whole system can be considered as parallel system, because the both end-effectors are holding fixed structure. Total DOFs of the system is 3, so three independent joints are needed to define movement of the whole system. Table 4.2 shows the classification of the joints, three joints of the working manipulator were set as independent joints and all joints except virtual valve handle joint were set as actuated joints. Jacobian matrix between the independent joints and the handle valve angle was derived as follows:

$$\dot{q}_V = \mathbf{J}\dot{\boldsymbol{q}}_{all} \tag{4.1}$$

$$\dot{q}_V = (\mathbf{J}_u + \mathbf{J}_v\boldsymbol{\Phi})\dot{\boldsymbol{q}}_u = \mathbf{J}_f\dot{\boldsymbol{q}}_u \tag{4.2}$$

where the term $\dot{q}_V$ is velocity of the handle valve angle and the term $\dot{\boldsymbol{q}}_u$ is velocity vector of independent joints. The term $\mathbf{J}$ is Jacobian matrix between all joints and the handle valve angle. The term $\boldsymbol{\Phi}$ is constraint Jacobian and $\mathbf{J}_f$ is Jacobian matrix between the independent joint and the handle valve angle. The detailed method for deriving kinematic modeling is explained on chapter 2.

4.1.2. Dynamics modeling

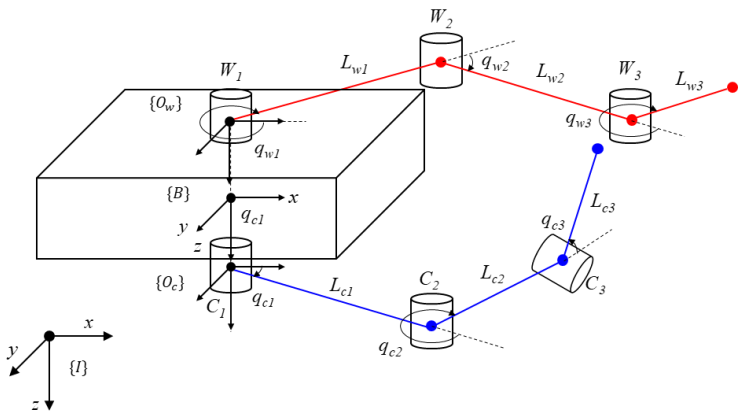

Fig. 4.2 Free floating dynamic model of the dual-arm UVMS.

The dynamic modeling of the UVMS was derived by applying parallel constraints to free-floating dynamic modeling of the UVMS. Fig 4.2 shows the free-floating dual-arm UVMS diagram.

$$\mathbf{M}(\boldsymbol{\zeta})\dot{\boldsymbol{\zeta}} + \mathbf{D}(\boldsymbol{q},\dot{\boldsymbol{q}},\boldsymbol{\zeta})\boldsymbol{\zeta} = \boldsymbol{\tau} \tag{4.3}$$

Equation (4.3) shows the dynamic equation of the whole UVMS. To derive the dynamic equation of the UVMS, Iterative Newton-Euler method were used [28, 34].

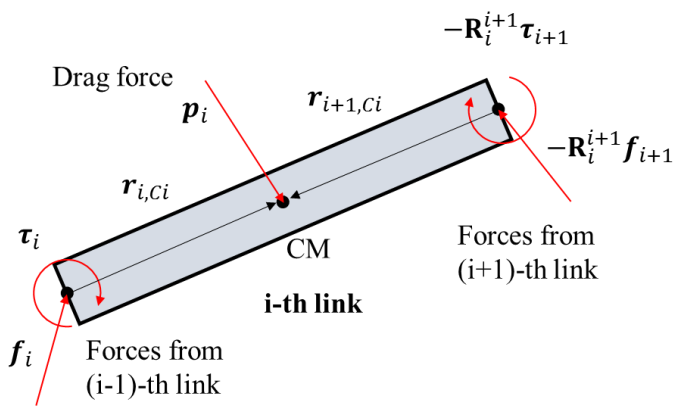

Fig. 4.3 Free-body diagram of *i*-th linkage.

Fig. 4.3 shows basic idea of the iterative Newton-Euler method. A free-body diagram of *i*-th linkage can be drawn as Fig. 4.3. First, acceleration of each linkage was derived by forward recursion process, which was done by following equation:

$$\boldsymbol{a}_{ci} = \mathbf{R}_i^{i+1}\boldsymbol{a}_{e,i-1} + \alpha_i \times \boldsymbol{r}_{i,Ci} \tag{4.5}$$

The term $\boldsymbol{a}_{ci}$ indicated the center of mass acceleration of *i*-th linkage and $\boldsymbol{a}_{e,i-1}$ indicated acceleration of end point of *i-1*-th linkage. α_i is angular acceleration of *i*-th linkage. $\mathbf{R}_i^{i+1}$ is transformation matrix between two linkage fixed coordinates. $\boldsymbol{r}_{i,Ci}$ is vector from *i*-th joint to center of mass of the *i*-th link.

After deriving acceleration terms of each linkage, force and torque applied to each linkage were calculated by backward recursion process. Following equations shows the backward recursion method.

$$\boldsymbol{f}_i = \mathbf{R}_i^{i+1}\boldsymbol{f}_{i+1} + m_i\boldsymbol{a}_{c,i} + \boldsymbol{p}_i \tag{4.6}$$

$$\boldsymbol{\tau}_i = \mathbf{R}_i^{i+1}\boldsymbol{\tau}_{i+1} - \boldsymbol{f} \times_i \boldsymbol{r}_{i,ci} + \mathbf{R}_i^{i+1}\boldsymbol{f}_{i+1} \times \boldsymbol{r}_{i+1,ci} + I_i\alpha_i \tag{4.7}$$

As seen in Fig. 4.3, $\boldsymbol{f}_i$ and $\boldsymbol{\tau}_i$ are force and torque from *i*-th joint. $\boldsymbol{p}_i$ is hydrodynamic drag term derived by assuming the shape of linkages as cylinder [35]. By repeating backward recursion to $\boldsymbol{\tau}_1$ and organizing result terms, dynamic equation of one ground-fixed manipulator can be calculated. The UVMS has moving platform and two manipulators, so set the $\boldsymbol{a}_{c0}$ term as the acceleration of the vehicle and proceed forward and backward recursion to get three equations.

$$\mathbf{M}_w\ddot{\boldsymbol{q}}_w + \mathbf{D}_{w5}\dot{\boldsymbol{q}}_w + \mathbf{M}_{Cw}^T\dot{\boldsymbol{v}} + \mathbf{D}_{w4}\boldsymbol{v} = \boldsymbol{\tau}_w \tag{4.8}$$

$$\mathbf{M}_c\ddot{\boldsymbol{q}}_c + \mathbf{D}_{c5}\dot{\boldsymbol{q}}_c + \mathbf{M}_{Cc}^T\dot{\boldsymbol{v}} + \mathbf{D}_{c4}\boldsymbol{v} = \boldsymbol{\tau}_c \tag{4.9}$$

$$\begin{aligned}&\mathbf{M}_v\dot{\boldsymbol{v}} + \mathbf{D}_v\boldsymbol{v} + \mathbf{H}_w\dot{\boldsymbol{v}} + \mathbf{D}_{w2}\boldsymbol{v} + \mathbf{M}_{Cw}\ddot{\boldsymbol{q}}_w + \mathbf{D}_{w3}\dot{\boldsymbol{q}}_w \\ &+ \mathbf{H}_c\dot{\boldsymbol{v}} + \mathbf{D}_{c2}\boldsymbol{v} + \mathbf{M}_{Cc}\ddot{\boldsymbol{q}}_c + \mathbf{D}_{c3}\dot{\boldsymbol{q}}_c = \boldsymbol{\tau}_v\end{aligned} \tag{4.10}$$

Equation (4.8) is a dynamic equation of a working manipulator and equation (4.9) is a clamping manipulator dynamics. Equation (4.10) is vehicle dynamics. The term $\boldsymbol{v}$ indicated body-fixed velocity of the vehicle. The term with subscription '$\boldsymbol{v}$' is vehicle related term, subscription '$\boldsymbol{w}$' is working manipulator related and subscription '$\boldsymbol{c}$' is clamping manipulator related terms. The term $\mathbf{M}_C$ is reaction forces and moments between the vehicle and the manipulator. Term $\mathbf{H}$ is added mass term due to manipulators. $\mathbf{D}_i$ terms are coupling drag terms except $\mathbf{D}_5$, the drag term of the manipulator itself. By combining and organizing the three equations, the equation (4.3) can be derived.

4.2. Desired trajectory generation

4.2.1. Desired valve angle trajectory

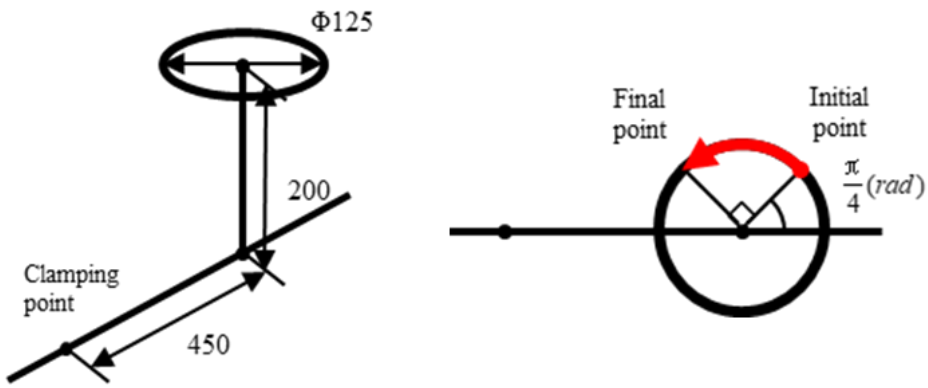

Fig. 4.4 Dimension of the objective handle valve and desired valve turning angle

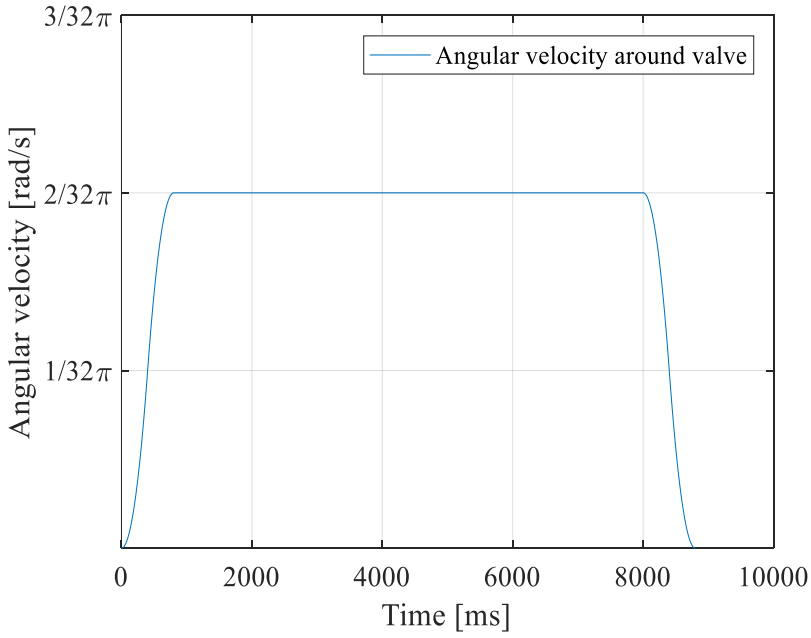

Fig. 4.5 Desired velocity profile of valve turning angle

Dimensions and desired trajectory of the objective handle valve were set as follows. Fig. 4.4 shows dimensions of the handle valve and desired valve turning angle. Diameter of the valve was set as 125 mm and height of the valve was set as 200 mm. These values were determined by referring the size of standard handle. The objective task of the system was set as turning the handle valve 90-degree counterclockwise direction. The clamping position of the manipulator was set as 450 mm from the valve center. Fig. 4.5 shows desired velocity profile of the handle valve. To prevent sudden change in acceleration of the system, second-order quadratic profile was used. The maximum speed of the handle valve was set as 1/16π rad/s.

4.2.2. Desired trajectory generation of independent joints

From the desired handle valve angle trajectory, desired trajectories of independent joints were derived. To find optimal trajectory for turning handle valve, the trajectory that minimizes velocity norm of actuated joints was considered as optimal. The objective function is as follows:

$$\min(\|\dot{\boldsymbol{q}}_r\|) \tag{4.11}$$

The square of velocity norm of actuated joint can be transformed as following form.

$$\|\dot{\boldsymbol{q}}_r\|^2 = \dot{\boldsymbol{q}}_u^T \boldsymbol{\Gamma}^T \boldsymbol{\Gamma} \dot{\boldsymbol{q}}_u \tag{4.12}$$

To minimize this term, weighted pseudoinverse was applied to equation (4.2) as follows:

$$\dot{\boldsymbol{q}}_{u,desired} = \mathbf{J}_f^{\ddagger} \dot{q}_{V,desired} \tag{4.13}$$

$$\mathbf{J}_f^{\ddagger} = (\mathbf{\Gamma}^{\mathrm{T}}\mathbf{\Gamma})^{-1}(\mathbf{J}_f(\mathbf{\Gamma}^{\mathrm{T}}\mathbf{\Gamma})^{-1})^{\dagger} \tag{4.14}$$

With the weighted pseudoinverse with weighting matrix $\mathbf{\Gamma}^{\mathrm{T}}\mathbf{\Gamma}$, which is constraint Jacobian matrix of the system, the objective function for the trajectory (4.12) can be achieved [36]. The desired independent joint trajectory that obtained by equation (4.13) can minimize the velocity norm of all actuated joints.

4.3. Force and torque distribution between two subsystems

4.3.1. Force and torque controller of the UVMS

The force and torque for performing valve turning task should be distributed to overcome limitations of the dual-arm manipulator. Using the weighted pseudoinverse method, the task loads can be distributed between two subsystems. The torque controller for UVMS was derived by modifying torque controller of redundant parallel manipulator system [29]. The equation of the torque controller is as follows:

$$\boldsymbol{\tau}_{r,desired} = (\mathbf{\Gamma}^{T})^{\#}(\mathbf{K}_v\dot{\boldsymbol{e}} + \mathbf{K}_p\boldsymbol{e}) \tag{4.15}$$

where $\boldsymbol{e}$ is error vector of the independent joint angles.

$$\boldsymbol{e} = \boldsymbol{q}_{u,d} - \boldsymbol{q}_u \tag{4.16}$$

The term $(\mathbf{\Gamma}^{T})^{\#}$ is weighted pseudoinverse of transposed constraint Jacobian matrix as follows:

$$(\mathbf{\Gamma}^{\mathrm{T}})^{\#} = \mathbf{W}^{-1}(\mathbf{\Gamma}^{\mathrm{T}}\mathbf{W}^{-1})^{\dagger} \tag{4.17}$$

where $\mathbf{W}$ is weighting matrix. By adjusting weighting matrix $\mathbf{W}$, the force and torque can be distributed within the actuated joint torque $\boldsymbol{\tau}_{r,desired}$.

4.3.2. Force and torque distribution

The weighting matrix $\mathbf{W}$ for distributing task forces and torques is 12 by 12 diagonal matrix. Equation (4.18) shows the weighting matrix and its corresponding actuated joint force and torques.

$$\mathbf{W} = \mathrm{diag}(w_x, w_y, w_z, w_\varphi, w_\theta, w_\psi, w_{w1}, w_{w2}, w_{w3}, w_{c1}, w_{c2}, w_{c3}) \tag{4.18}$$

By properties of weighted pseudoinverse, the actuated joint that has large weighting is more minimized than others while performing the task. The components of the weighting matrix were determined proportionally to reciprocal of maximum possible force and torque of actuated joints and thrust components. Table 4.3 shows the maximum capabilities of each actuated joint (including virtual vehicle joints).

Table 4.3 Maximum capabilities of each actuated joint

$f_{x,\max}$	$f_{y,\max}$	$f_{z,\max}$	$\tau_{\varphi,\max}$	$\tau_{\theta,\max}$	$\tau_{\psi,\max}$	$\tau_{m,\max}$
80.3 N	80.3 N	113.6 N	18.5 Nm	42.9 Nm	60.7 Nm	10 Nm

Therefore, the weighting matrix for distributing loads was determined as Table 4.4. The values were normalized with $f_{x,\max}$ value of Table 4.3.

Table 4.4 Values of diagonal components of the weighting matrix

w_x	w_y	w_z	w_φ	w_θ	w_ψ
1.00	1.00	0.71	4.35	1.88	1.33
w_{w1}	w_{w2}	w_{w3}	w_{c1}	w_{c2}	w_{c3}
8.09	8.09	8.09	8.09	8.09	8.09

4.4. Disturbance compensation method

External disturbance is one of the main problems on underwater operations. Adding disturbance compensating term to the torque controller equation (4.15), known disturbance can be compensated during the operation. Because disturbance mainly caused by underwater current, external disturbance mainly applied to the vehicle. Therefore, disturbance on the vehicle was only considered. Equation (4.19) shows the torque controller with disturbance compensating term.

$$\boldsymbol{\tau}_{r,desired} = (\boldsymbol{\Gamma}^{T})^{\#}(\mathbf{K}_{v}\dot{\boldsymbol{e}} + \mathbf{K}_{p}\boldsymbol{e}) + \boldsymbol{\tau}_{Comp} \tag{4.19}$$

By using virtual work theorem, desired force and torque for compensating disturbance exerted on the vehicle can be calculated as follows:

$$\boldsymbol{\tau}_{comp} = (\boldsymbol{\Gamma}^{\mathrm{T}})^{*}\mathbf{J}_{b}^{T}(-\boldsymbol{f}_{d}) \tag{4.20}$$

The term $\boldsymbol{f}_{d}$ is disturbance force applied on the vehicle and $\mathbf{J}_{b}$ is Jacobian matrix between the independent joints and the vehicle position and orientation. Weighted pseudoinverse was also used for compensating to distribute compensating loads.

$$(\boldsymbol{\Gamma}^{\mathrm{T}})^{*} = \mathbf{W}_{d}^{-1}(\boldsymbol{\Gamma}^{\mathrm{T}}\mathbf{W}_{d}^{-1})^{\dagger} \tag{4.21}$$

Similar to previous section, the compensating load can be distributed between two subsystems by adjusting weighting matrix $\mathbf{W}_{d}$. The cooperation weighting matrix for disturbance compensation was set as same matrix as task weighting matrix.

$$\mathbf{W}_{d} = \mathrm{diag}(w_{x}, w_{y}, w_{z}, w_{\varphi}, w_{\theta}, w_{\psi}, w_{w1}, w_{w2}, w_{w3}, w_{c1}, w_{c2}, w_{c3}) \tag{4.22}$$

4.5. Stability analysis

The control equation of the system is shown in equation 4.19 and 4.20. By substituting two equations to equation 2.13, the following equation can be obtained.

$$\hat{\mathbf{M}}\ddot{\boldsymbol{q}}_u + \hat{\mathbf{C}}\dot{\boldsymbol{q}}_u + \hat{\mathbf{D}}\dot{\boldsymbol{q}}_u - \mathbf{K}_v\dot{\boldsymbol{q}}_u - \mathbf{K}_p(\boldsymbol{q}_{u,d} - \boldsymbol{q}_u) = 0 \tag{4.23}$$

The Lyapunov function for this system was selected as equation 4.24. Differentiating Lyapunov function to obtain equation 4.25.

$$V = \frac{1}{2}\dot{\boldsymbol{q}}_u^T\hat{\mathbf{M}}\dot{\boldsymbol{q}}_u + \frac{1}{2}\boldsymbol{q}_u^T\mathbf{K}_p\boldsymbol{q}_u \tag{4.24}$$

$$\dot{V} = -\dot{\boldsymbol{q}}_u^T(\mathbf{K}_v + 2\hat{\mathbf{D}} + 2\hat{\mathbf{C}} - \hat{\mathbf{M}})\dot{\boldsymbol{q}}_u \tag{4.25}$$

The term $\hat{\mathbf{M}} - 2\hat{\mathbf{C}}$ is zero due to dynamics condition [29]. Eliminating those terms and arranging the equation 4.25 to get an equation as follows:

$$\dot{V} = -\dot{\boldsymbol{q}}_u^T(\mathbf{K}_v + \boldsymbol{\Lambda}^T\mathbf{D}\boldsymbol{\Lambda} + 2\boldsymbol{\Lambda}^T\mathbf{M}\dot{\boldsymbol{\Lambda}})\dot{\boldsymbol{q}}_u \tag{4.26}$$

$$\dot{V} \le -\lambda_{min}(\mathbf{K}_v + \boldsymbol{\Lambda}^T\mathbf{D}\boldsymbol{\Lambda} + 2\boldsymbol{\Lambda}^T\mathbf{M}\dot{\boldsymbol{\Lambda}})\left\|\dot{\boldsymbol{q}}_u\right\|^2 \tag{4.27}$$

The inertia matrix $\mathbf{M}$ and damping matrix $\mathbf{D}$ are positive definite matrices. With enough size of drag term compared to inertia and velocity related term $2\boldsymbol{\Lambda}^T\mathbf{M}\dot{\boldsymbol{\Lambda}}$, the controller can be considered as stable in operation region.

Chapter 5. Simulation

5.1. Simulation setup

Based on kinematics and dynamics of the UVMS, the simulation of the cooperation method was made. The simulation was made by MATLAB 2017a version with Simulink. Fig. 5.1 shows the Simulink simulation of the system and Fig. 5.2 shows the desired trajectory of actuated joints. The handle valve was considered to have 5 Nm of friction.

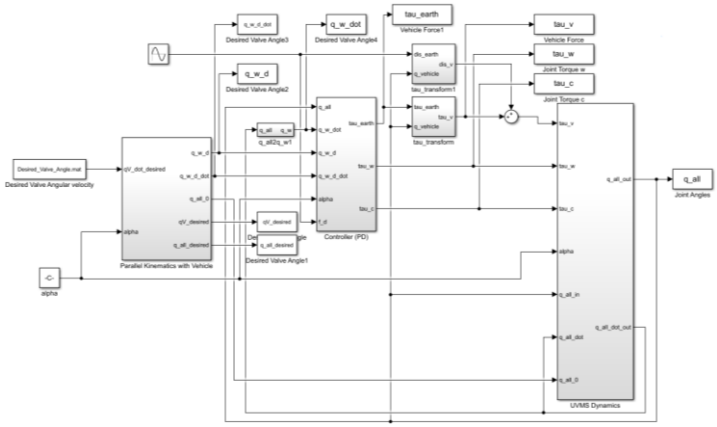

Fig. 5.1 Valve turning simulation made by MATLAB Simulink.

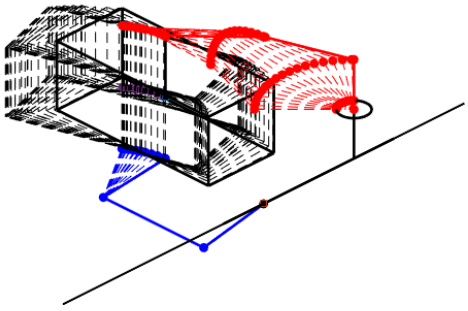

Fig. 5.2 Desired trajectory of the UVMS.

5.2. Simulation without disturbance

5.2.1. Without cooperation

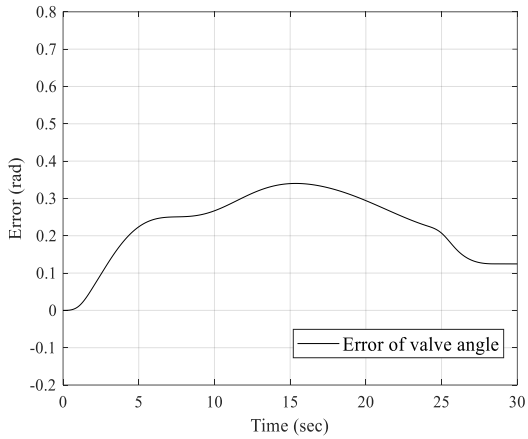

Fig. 5.3 Error of valve angle trajectory.

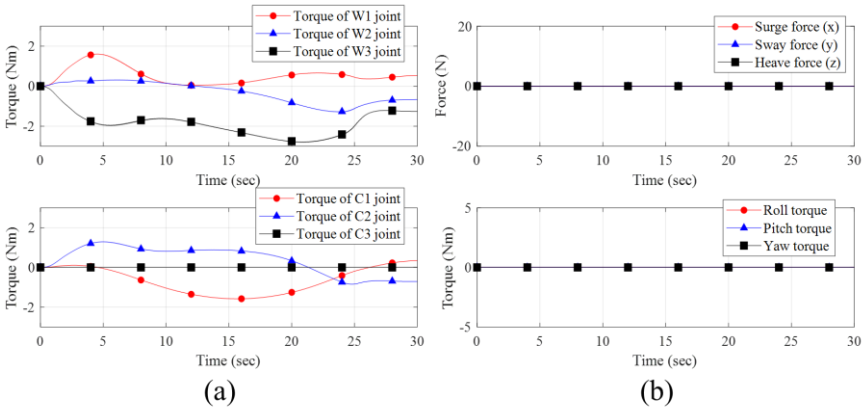

(a) (b)

Fig. 5.4 The manipulator torque and vehicle force of the simulation without cooperation. (a) Joint torque of the manipulator. (b) Vehicle force and torque.

Without cooperation, the manipulators took all task loads for turning handle valve. The vehicle did not produce any thrust force for performing the task.

5.2.2. With cooperation

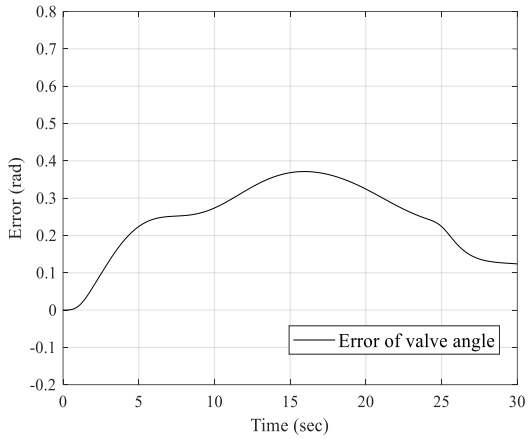

Fig. 5.5 Error of valve angle trajectory.

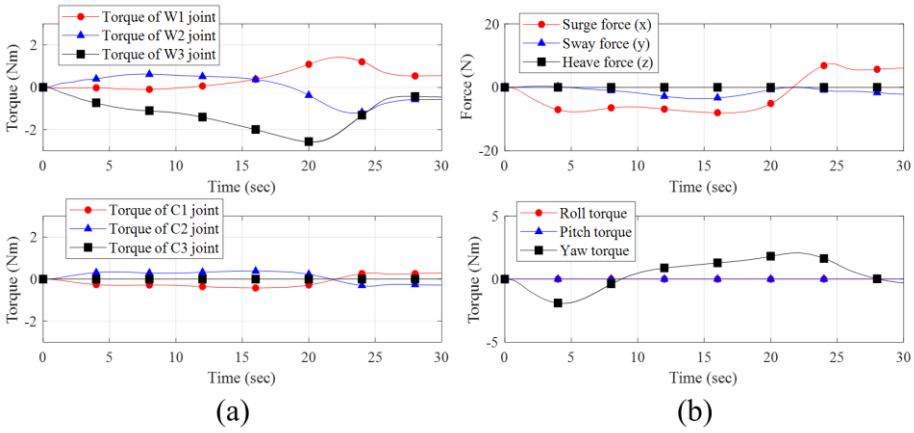

Fig. 5.6 The manipulator torque and vehicle force of the simulation with cooperation. (a) Joint torque of the manipulator. (b) Vehicle force and torque.

With cooperation, the maximum torques of the manipulators were reduced significantly. The vehicle thrust was also used to help the valve turning task of manipulator.

5.2.3. Comparison

The maximum joint torque of all joints were reduced when applying proposed cooperation method. Table 5.1 summarizes the maximum torque value of two cases. Torque of some joints such as W1, W2, W3 joints were reduced a little bit while torque of C1 and C2 joints were reduced significantly. The concept of cooperation can be used to reduce manipulator's burden by using thrust force of the vehicle. With the smaller maximum joint torque of the manipulator, the smaller manipulator can be used for the valve turning operation. Therefore, it can be concluded that using proposed cooperation algorithm is beneficial for designing and operating UVMS.

Table 5.1 Maximum joint torque of each joint of two cases

	W1	W2	W3	C1	C2
Manipulator only	1.62 Nm	1.30 Nm	2.81 Nm	1.58 Nm	1.30 Nm
Cooperation	1.44 Nm	1.23 Nm	2.61 Nm	0.42 Nm	0.39 Nm

5.3. Simulation with disturbance

To prove the effect of cooperation algorithm on compensating disturbance, the simulation was performed. While setting the desired system movement as zero, 5 N size disturbance was applied to the 45 degrees with respect to the direction of the vehicle.

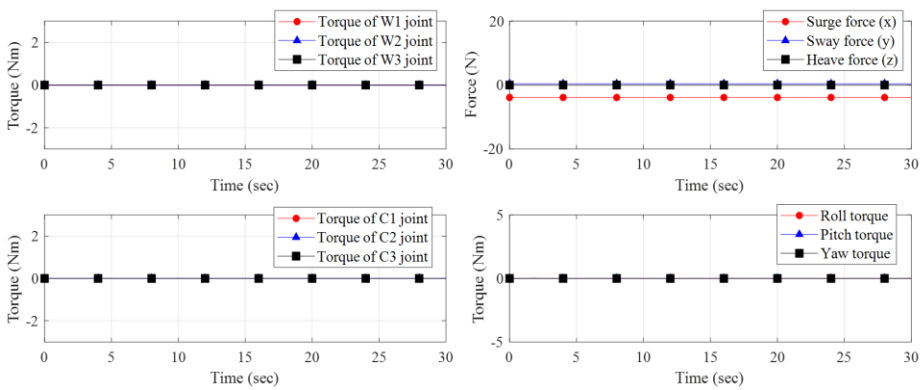

(a) (b)

Fig. 5.7 Disturbance compensating joint torque and vehicle thrust without cooperation. (a) Joint torque of each joint. (b) Vehicle thrust force.

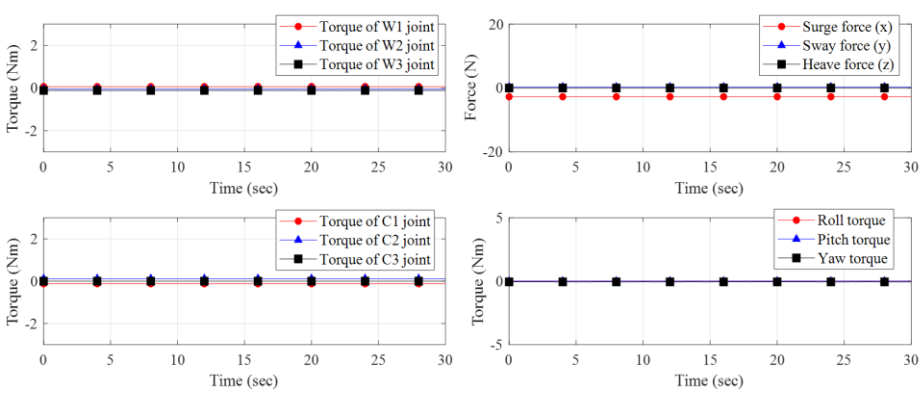

(a) (b)

Fig. 5.8 Disturbance compensating joint torque and vehicle thrust with cooperation. (a) Joint torque of each joint. (b) Vehicle thrust force.

Fig 5.7 and Fig. 5.8 show the joint torque and vehicle thrust for compensating disturbance. While cooperation method is applied, the dual-arm manipulator helps compensating disturbance task of the vehicle. Table 5.2 shows the size of the vehicle force vector and maximum manipulator joint torque for compensating disturbance. When using cooperation algorithm for compensating disturbance, the vehicle force is reduced about 30% with using only 0.1 Nm of the manipulator joint torque. The dual-arm manipulator compensates disturbance applied on the vehicle by producing internal force to the vehicle. Due to the properties of parallel manipulator, large internal force can be produced with small joint torque. Therefore, by using proposed cooperation method on compensating disturbance is efficient for the system.

Table 5.2 Vehicle force and maximum joint torque of compensating disturbance.

	Vehicle force	Max joint torque
Vehicle only	3.89 N	0.00 Nm
Cooperation	2.73 N	0.12 Nm

5.4. Valve turning operation under disturbance

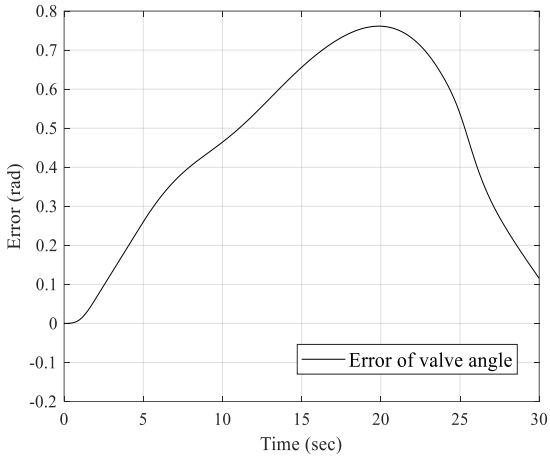

Fig. 5.9 Error of valve angle, without disturbance compensation algorithm under disturbance.

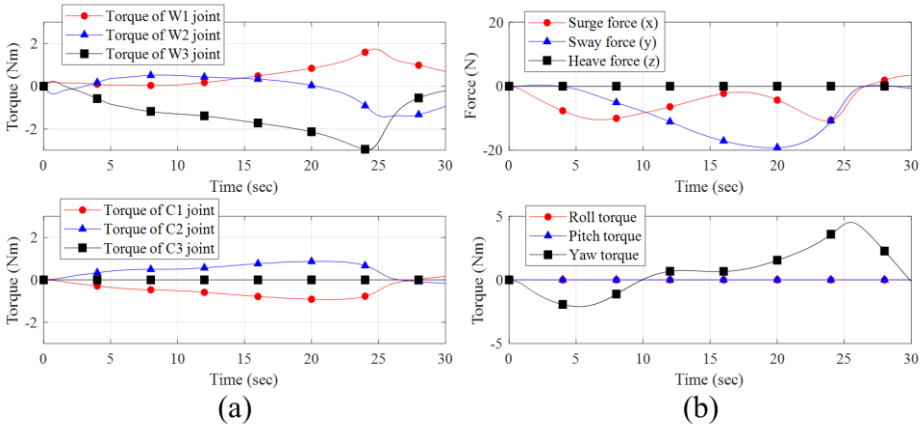

Fig. 5.10 Joint torque of the manipulator without disturbance under disturbance. (a) Manipulator joint torque graph; (b) Vehicle force and torque.

Fig. 5.9 shows valve angle under disturbance without using disturbance compensation algorithm. Without disturbance compensation and cooperation, the manipulator takes most of the task load, as shown on Fig. 5.10.

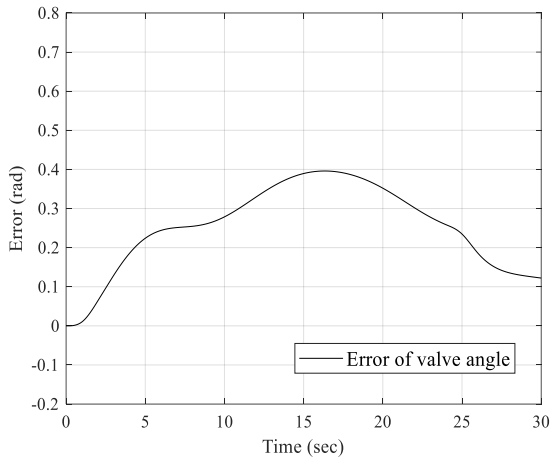

Fig. 5.11 Error of valve angle, with disturbance compensation algorithm under disturbance.

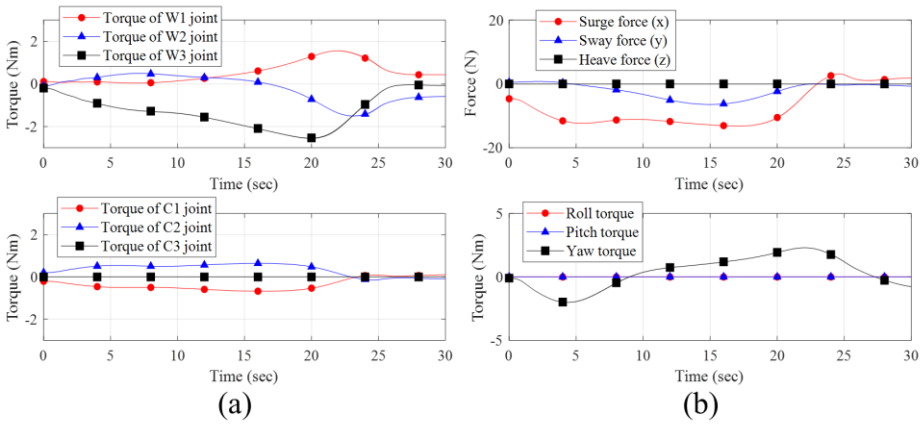

(a) (b)

Fig. 5.12 Joint torque of the manipulator with disturbance under disturbance. (a) Manipulator joint torque graph; (b) Vehicle force and torque.

Fig. 5.11 shows the valve angle error with disturbance compensation algorithm. Compared to Fig. 5.9, the trajectory error is reduced by using disturbance compensation algorithm. Also, by using cooperation algorithm, the joint torque of the manipulator was reduced. The vehicle thrusts helped the valve turning operation, so the required joint torque is reduced.

Chapter 6. Experiments and results

6.1. Underwater manipulator joint design

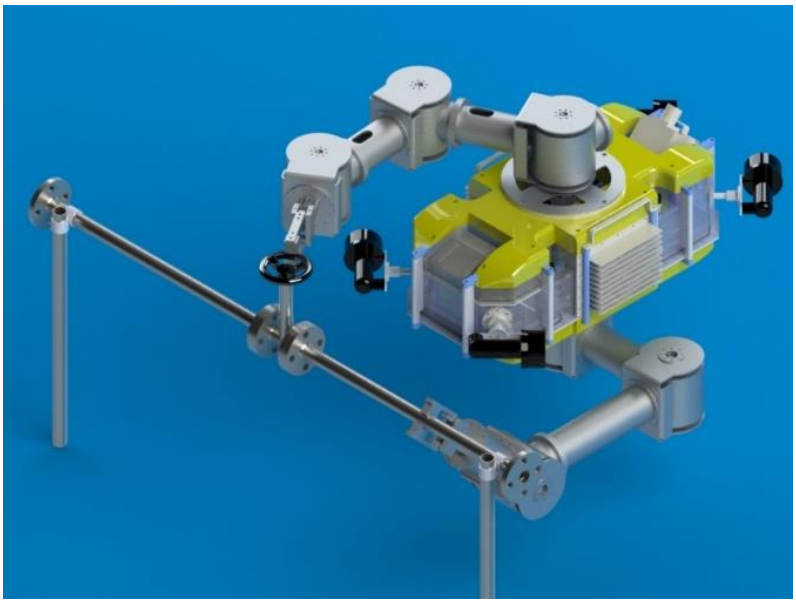

Fig. 6.1 TTURT with dual-arm module attached and the handle valve test bench

To prove the effect of the proposed cooperation algorithm, the dual-arm manipulator for TTURT was designed and manufactured. The dual-arm manipulator is composed of six underwater joint modules. The joint module includes a brushless electric DC (BLDC) motor, a torque sensor with strain gauge and a motor driver. A rotary seal is inserted into the joint module for waterproof countermeasure. For end-effectors of the manipulator, a pneumatic clamp is selected due to waterproof problem and clamping strength.

Also, the replica for an underwater handle valve structure was designed and built. A standard handle valve was selected for test bench and the valve is connected on steel pipe with diameter of 30 mm. The design of overall system and the test bench is presented on Fig. 6.1.

6.1.1. Mechanical design

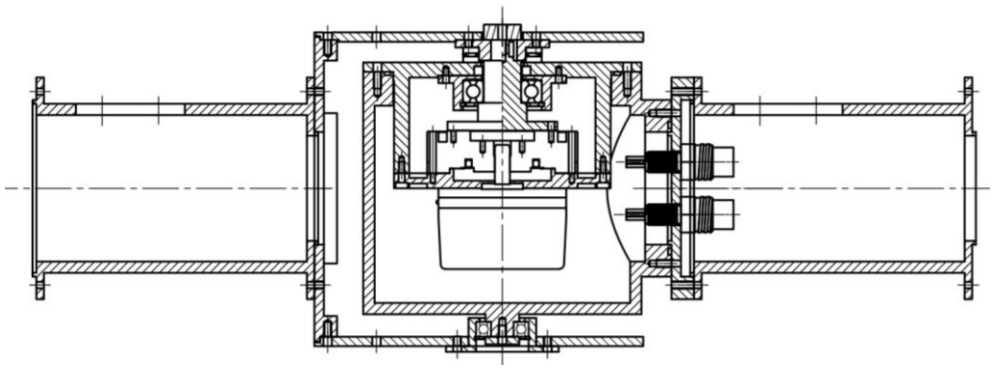

Fig. 6.2 Detailed design of a joint module for the dual-arm manipulator

Fig. 6.2 shows the internal and external design of the underwater joint module. A BLDC motor, a harmonic drive reducer, a torque sensor and a motor driver are located inside of a water proof casing. External casing of the joint module was made with AL6061 alloy. An output axis of the joint module, which is made with S45C alloy, connected to a fork structure which fixes between joint modules. Fig. 6.3 shows components of joint casing.

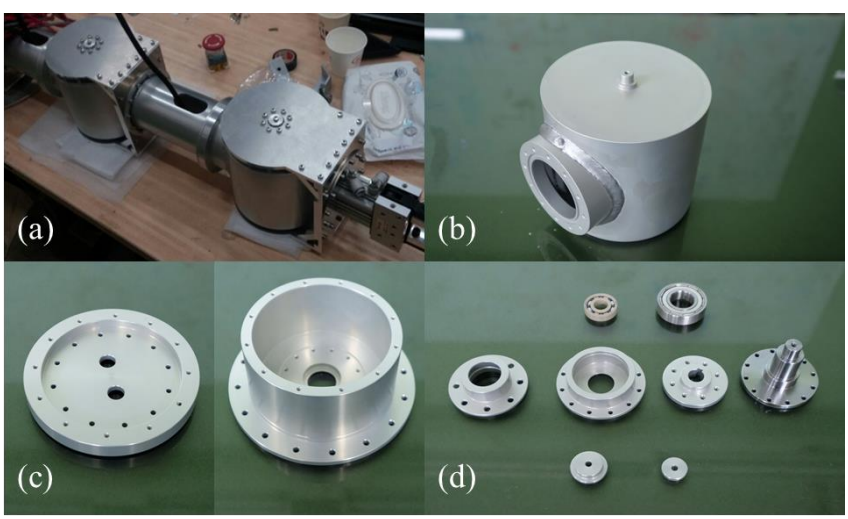

Fig. 6.3 Joint casing components—(a) Connecting structures including fork; (b) Joint casing; (c) Side cover and main cover; (d) Output axis and other components.

6.1.1.1. Waterproof sealing

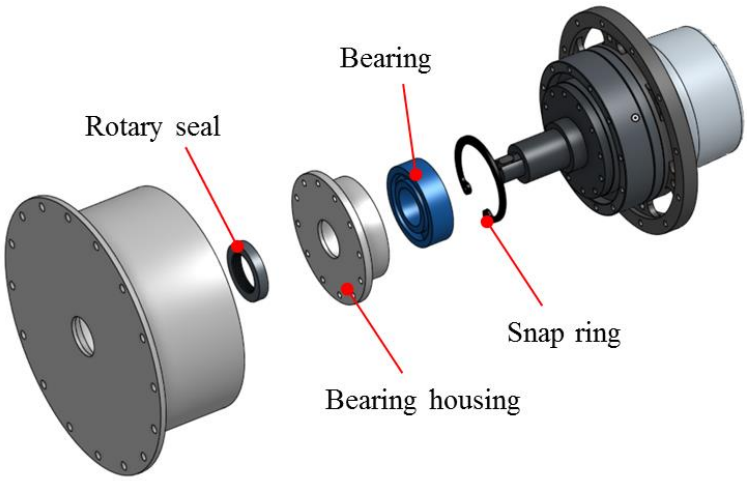

Fig. 6.4 Waterproof design of the joint module

Waterproof countermeasure is very important part for designing underwater systems. The hardest part is sealing rotating output axis of the joint module. A rotary seal (profile R04a) was used to prevent flooding through rotating axis, which is made with poly urethane (PU). O-rings that made with nitrile butadiene rubber (NBR) were used to prevent waterlogging between the casing cover and the main casing. Sealing design of the joint module is shown in Fig. 6.5.

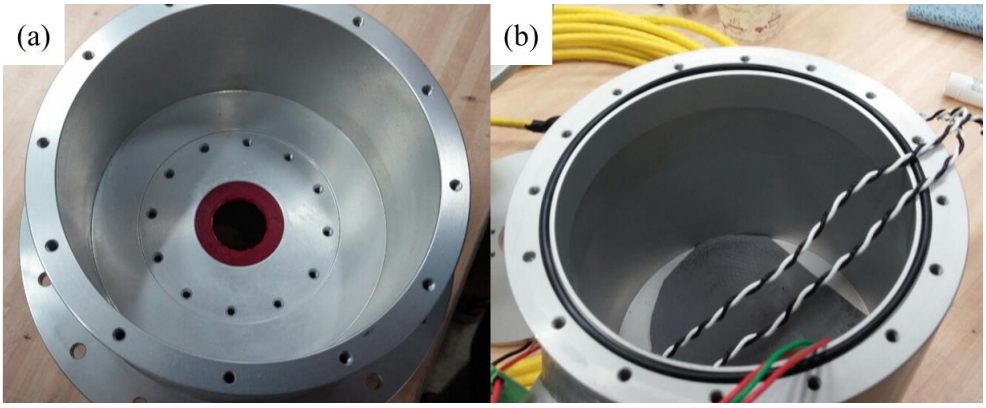

Fig. 6.5 Waterproof components of the joint module—(a) Rotary seal; (b) O-ring and its housing.

6.1.1.2. End-effector

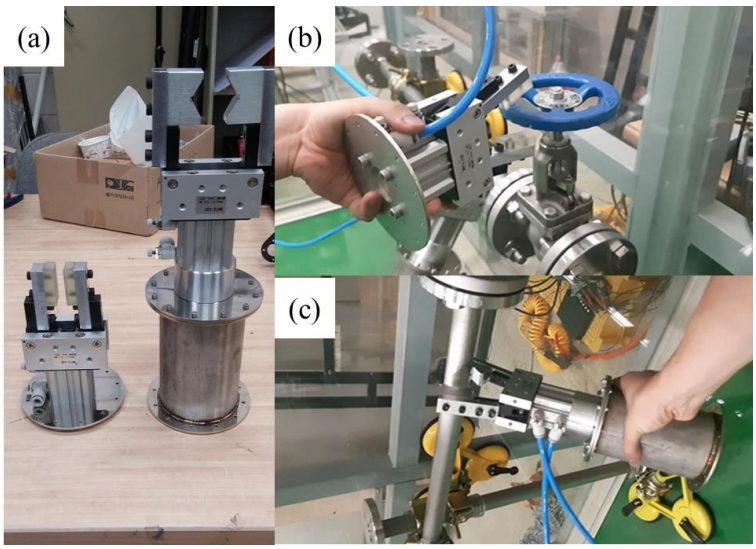

Fig. 6.6 Pneumatic end-effectors of the dual-arm manipulator—(a) A handle grabbing end-effector (left) and a pipe clamping end-effector (right); (b) Grabbing handle valve; (c) Clamping on a pipe structure.

A proper end-effector is needed for strong grasping of the handle valve and clamping on the pipe structure. A pneumatic air clamp (CDQ32-15, SMC) was selected for an end-effector of the dual-arm manipulator. Due to the toggle mechanism of a pneumatic clamp, the clamping can be maintained until a structure of the clamp is collapsed. Compressed air for pneumatic toggle clamp was supplied outside of water tank by an air compressor. Fig. 6.6 shows both of manufactured the end-effectors of the dual-arm manipulator and their movements.

6.1.2. Electronic components

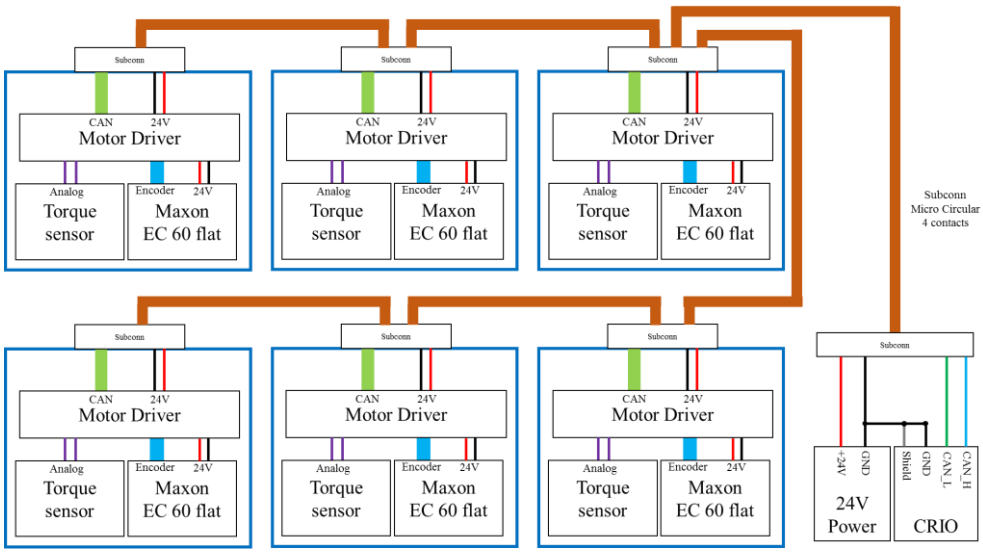

Fig. 6.7 Signal map of the dual-arm manipulator

Overall signal and power diagram of the dual-arm manipulator is presented on Fig. 6.7 National instrument CompactRIO (NI 9082) is used for controller of the dual-arm manipulator, which is located outside of the water tank. The dual-arm manipulator uses CAN protocol to communicate with main controller, and NI high speed CAN module was applied to make CAN communication. The electric component of the joint module is summarized on Table 6.1.

Table 6.1 Electric components of the dual-arm manipulator.

Components	EA	Maker
Motor	6	Maxon EC 60 flat, 24V 100W
Reducer	6	SBB SCSD-17-100-2UF
Motor driver	6	Robotro customized
Controller	1	NI CRIO 9082
Torque sensor	6	SETECH customized
DC power supply	1	24V 1500W
Waterproof cable		Subconn Micro series

6.1.2.1. Actuator

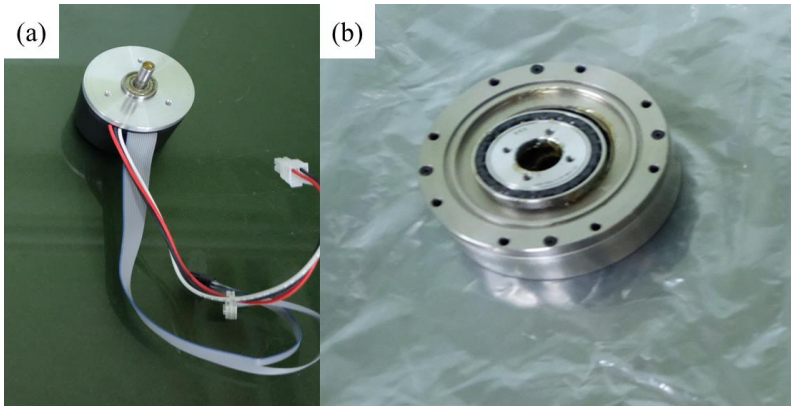

Fig. 6.8 Actuator components of the joint module (a) BLDC motor (Maxon EC flat 60); (b) Harmonic drive (SCSD-17-100-2UF).

An actuating motor (Maxon, EC flat 60) is BLDC type servo motor. The input voltage of the motor is 24 V and the power of it is 100 W. Harmonic drive reducer (SBB tech, SCSD-17-100-2UF) was assembled to the motor, the reducing ratio of which is 1/100. Fig 6.8 shows the actuating motor and the harmonic reducer of the joint module.

6.1.2.2. Torque sensor

Fig. 6.9 Torque sensor attached on BLDC motor

A torque sensor (SETECH, special order) was attached to the actuator to measure actual torque applied on the joint module. The maximum torque of the sensor is 20 Nm for three working manipulator joints, and 50 Nm for three clamping manipulator joints. Fig. 6.9 shows the assembled torque sensor, and Fig. 6.10 shows the assembling method of the actuator.

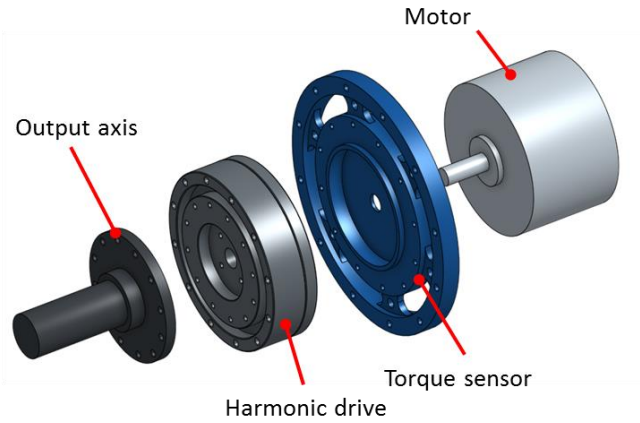

Fig. 6.10 Actuator assembly of the joint module

6.1.2.3. Motor driver

Fig. 6.11 BLDC motor driver (Robotro, special order)

A BLDC motor driver was specially ordered from Robotro to fit the driver into narrow space of the joint module. The driver is capable of receiving torque sensor value and transferring the data with CAN communication.

6.1.3. Torque controller of the joint module

To perform the presented cooperation algorithm, each joint module should produce desired joint torque. By using a torque sensor, the applied torque by the joint module can be directly measured. However, as shown in Fig. 6.4, a rotary seal produces large friction force to the output axis, which cause error between actual applied joint torque and torque sensor value. The friction caused by a rotary seal was removed by feedforward compensation. Dahl's friction model was used to estimate the friction term [38]. The friction force was modeled as a differential equation with the function of displacement. Equation (6.1) shows friction force with Dahl model, and the model can be changed as function of time as equation (6.2). Fig 6.12 shows the relation between displacement and friction force.

$$\frac{dF}{dx} = \sigma(1-\frac{F}{F_c}\operatorname{sgn} v)^{\alpha} \tag{6.1}$$

$$\frac{dF}{dt} = \sigma(1-\frac{F}{F_c}\operatorname{sgn} v)^{\alpha} v \tag{6.2}$$

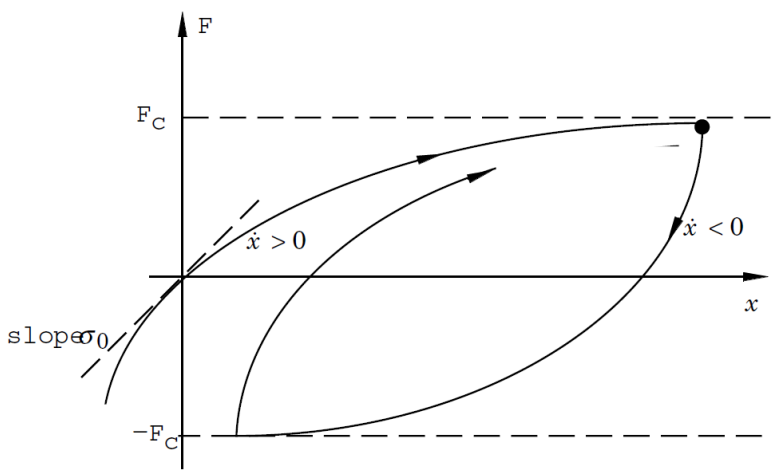

Fig. 6.12 Dahl friction model. The friction force presented as function of displacement [38].

The constants of Dahl model, which are σ, F_c and α, are obtained by experiments for each joint module. Parameter α indicates overall shape friction curve, and set as 1 for all joint modules. Parameter σ and F_c vary for each joint module. Table 6.2 shows the friction parameters of each joint module. With feedforward compensation of friction force, the error value of torque sensor from friction force was significantly reduced. Fig. 6.13 shows results of repeated movement test of the joint module between two positions. Effect of friction is rarely shown in this result.

Table 6.2 Dahl friction parameters of each joint module.

Joint number	W1	W2	W3	C1	C2	C3
σ	80	150	50	50	90	50
F_c	0.55	0.8	0.35	0.32	0.55	0.50

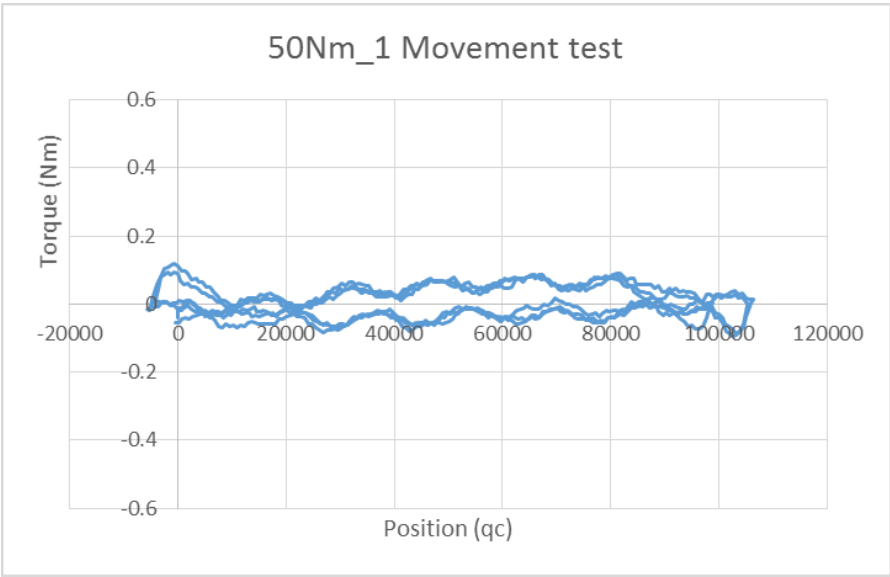

Fig. 6.13 The torque sensor value of C1 joint with repeated movement test.

After friction compensation was completed, a torque controller was designed. Proportion-Integration (PI) controller was used for the torque controller. A process variable is set as value of a torque sensor, and control input is motor driver duty input (-4096 ~ 4096 command input). Friction force is compensated with Dahl friction model, which is function of joint module's angular velocity. Fig. 6.14 shows a torque controller diagram of one joint module. Fig. 6.15 shows joint module's response of sinusoidal desired input.

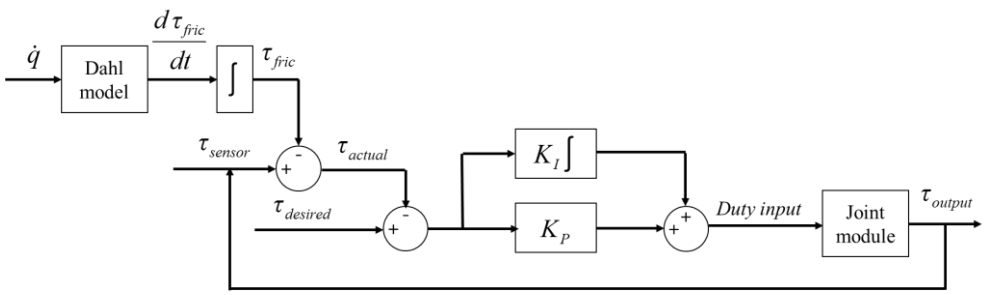

Fig. 6.14 Torque controller diagram of a joint module.

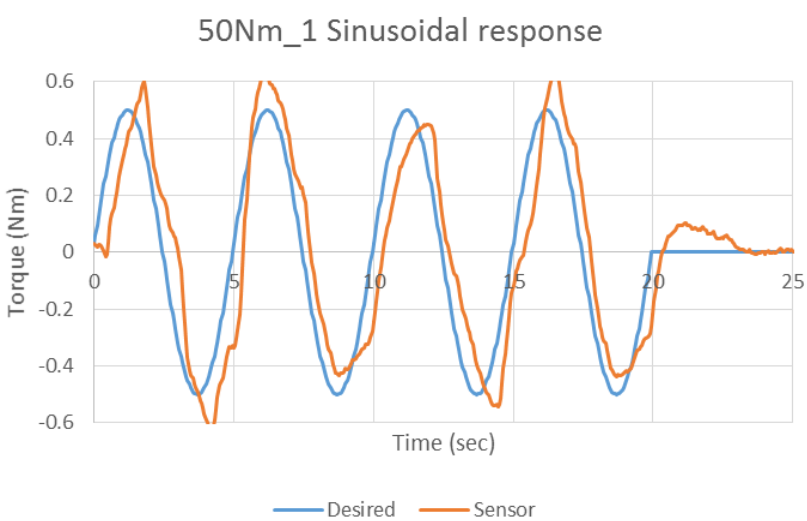

Fig. 6.15 Sinusoidal response of a joint module C1. (Sinusoidal input with amplitude 0.5 Nm and frequency 0.2 Hz)

6.1.4. Test bench design

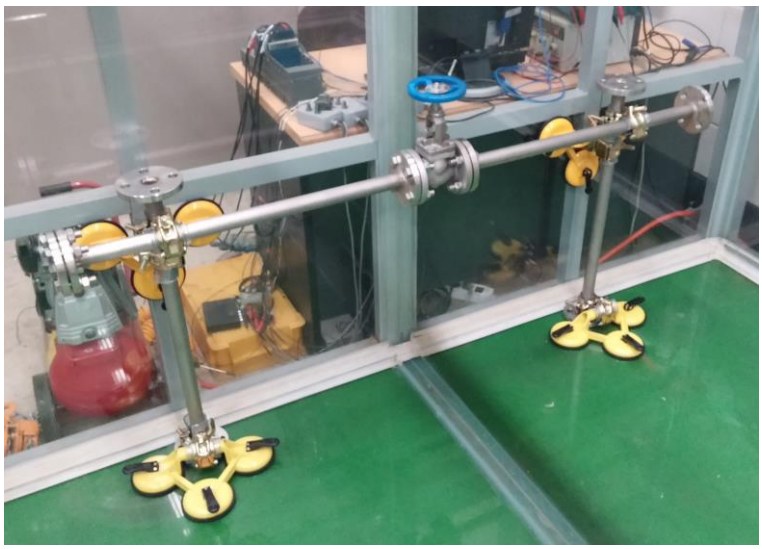

Fig. 6.16 Replica of the underwater handle valve

To perform turning underwater valve task, replica of an underwater handle valve was designed and built. The standard handle valve was selected for example of the handle valve. The structure was built with stainless steel pipes (diameter 30 mm). Four vacuum cup holders (SM-VH03) were used to fix the whole structure on glass surface of a water tank. Fig. 6.16 shows the constructed test bench for valve turning.

6.2. Experimental results

6.2.1. Experimental setup

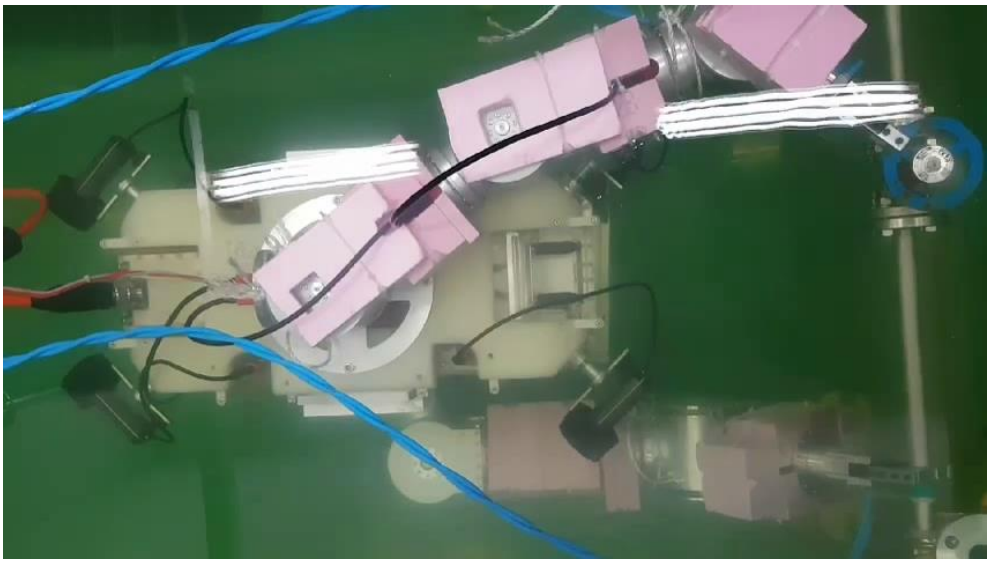

Fig. 6.17 Valve turning experiment setup

With the constructed underwater valve structure described in previous section, valve turning experiments were conducted. To maintain neutral buoyancy of the system, pink foam board was cut and used as buoyant material. By using external air compressor, two end-effectors of the dual-arm manipulator are operated.

The joints are moved to initial position by using position control mode of the operating program. After setting initial joint positions of the dual-arm manipulator, the system is moved to valve clamping position by hands. The end-effectors of dual-arm manipulators are closed to clamp the UVMS on its initial position for turning the valve. After these process, the valve turning operation is started with the cooperative algorithm.

6.2.2. Effect of cooperation

6.2.2.1. Comparison with simulation

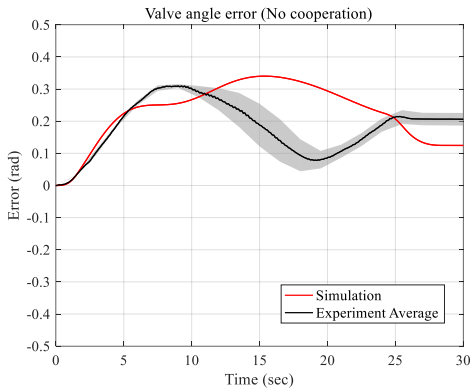

Fig. 6.18 Valve angle error without cooperation. Simulation data is denoted as red dashed line, and experimental data is presented as black line.

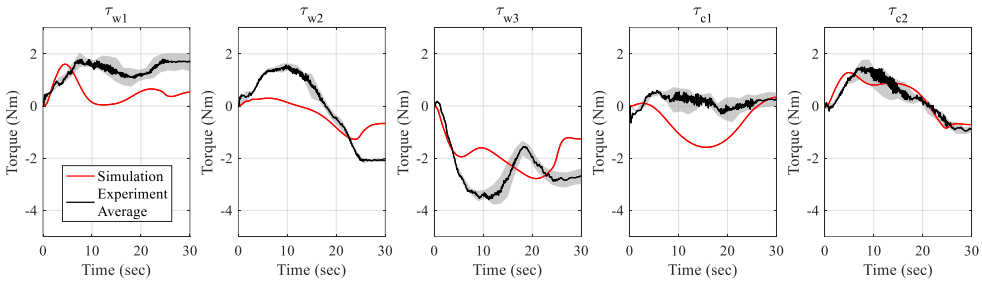

Fig. 6.19 Joint torque graph of valve turning operation without cooperation. Simulation data is denoted as red dashed line, and experimental data is presented as black line.

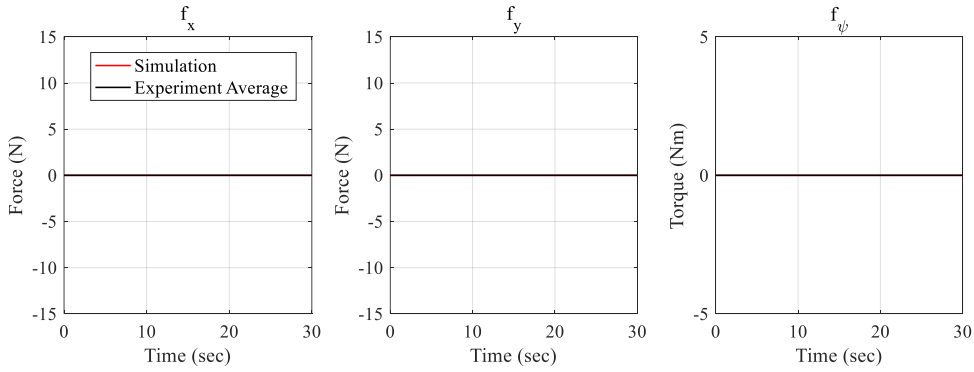

Fig. 6.20 Vehicle thrust force vector of valve turning experiment without cooperation.

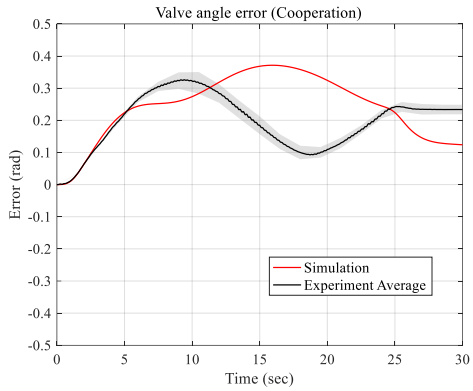

Fig. 6.21 Valve angle error with cooperation. Simulation data is denoted as red dashed line, and experimental data is presented as black line.

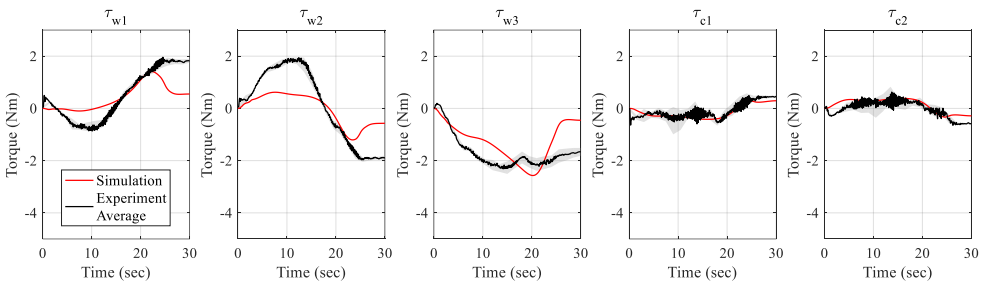

Fig. 6.22 Joint torque graph of valve turning operation with cooperation. Simulation data is denoted as red dashed line, and experimental data is presented as black line.

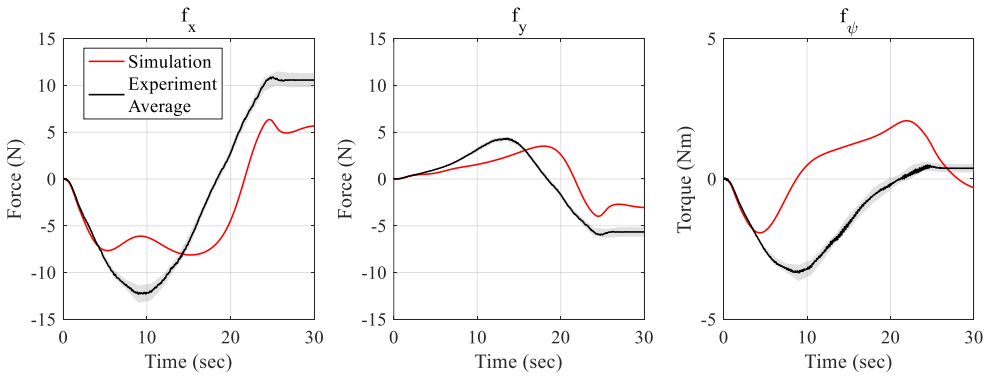

Fig. 6.23 Vehicle thrust force vector of valve turning experiment with cooperation.

The experiments for each case was conducted five times and the averages of the experiments were presented. On Fig. 6.18 to Fig. 6.23, the averages of the experiments were indicated as black lines, and standard deviations of the results were indicated as dim grey area. Simulation results were denoted as red lines. Fig. 6.18 shows the simulation and experimental data of valve angle error without cooperation, using torque of the manipulator only for turning the valve. The experimental data shows similar amount of error with respect to the simulation data. Fig. 6.19 shows joint torque data of simulation and experiments. The error between the simulation and the experiment mainly caused by the slip between the end-effector and the handle valve, which was not considered on the simulation. Also, inaccurate friction modeling of the joint module and the handle valve may cause this difference. However, the tendency of the joint torque and the valve angle error is similar to the simulation data. Fig. 6.20 shows vehicle thrust force vector of the simulation and the experiment. The vehicle did not produce any thrust force vector as shown on the simulation. Fig 6.21 to Fig 6.23 show the simulation and the experiment data with cooperation, using both manipulator torque and vehicle thrust force for turning the valve. The difference between the experimental data and the simulation data shows similar tendency of previous case, but error with respect to the simulation is smaller.

6.2.2.2. Advantages of cooperation

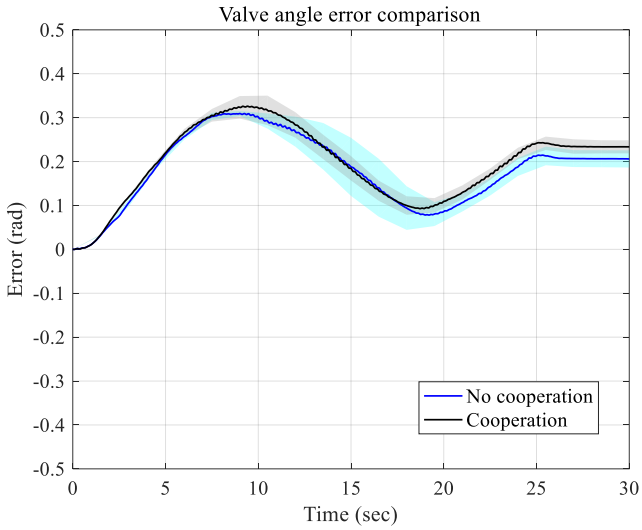

Fig. 6.24 Valve angle error without cooperation and with cooperation.

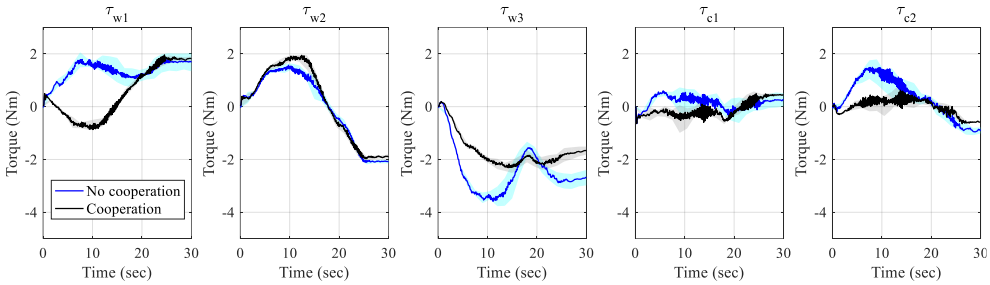

Fig. 6.25 Joint torque values without cooperation and with cooperation.

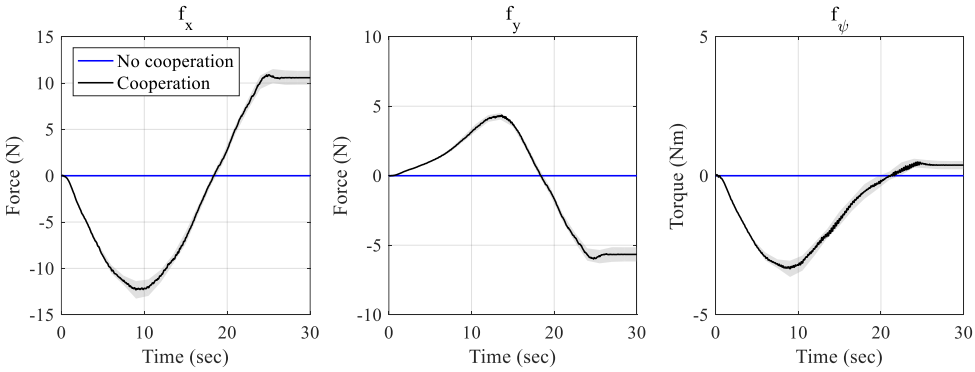

Fig. 6.26 Vehicle thrust force vector of valve turning experiment without cooperation and with cooperation.

To compare two cases, the torque values of joints were reduced when applying cooperation algorithm. Fig. 6.24 to Fig. 6.26 show the comparison of the experimental results of two cases. The averages of results without cooperation were denoted as blue lines, and standard deviations of the results were indicated as dim sky-blue area. The averages of results with cooperation were denoted as black lines, and standard deviations of the results were indicated as dim grey area. As presented on Fig. 6.24, using vehicle thrust to helping manipulator's task does not affect the trajectory of the valve. Root mean square error was 0.20 rad without cooperation, and 0.21 rad with cooperation, which were almost same. Fig. 6.25 shows the torque values of joints of two cases. The torque of W3 and C2 joint were significantly reduced, while maximum torque of W1, W2 and C1 show little difference. Fig.6.26 shows vehicle thrust vector of the two cases.

Fig. 6.27 shows the maximum torque values of each joint. Error bars indicate standard deviation of each maximum torque value. In case of W1 joint, applying of cooperation shows slightly large maximum torque than without cooperation, which almost same as error tolerance of the torque sensor. Torque value of joint W2 and C1 were slightly reduced with using cooperation algorithm. However, W3 and C2 joint torque are significantly reduced. Therefore, applying the cooperation algorithm, the maximum joint torque of the manipulator can be reduced without losing of trajectory tracking accuracy.

Table 6.3 Effect of the cooperation to maximum joint torque

Joints	W1	W2	W3	C1	C2
	↑10%	↓5%	↓36%	↓0%	↓60%

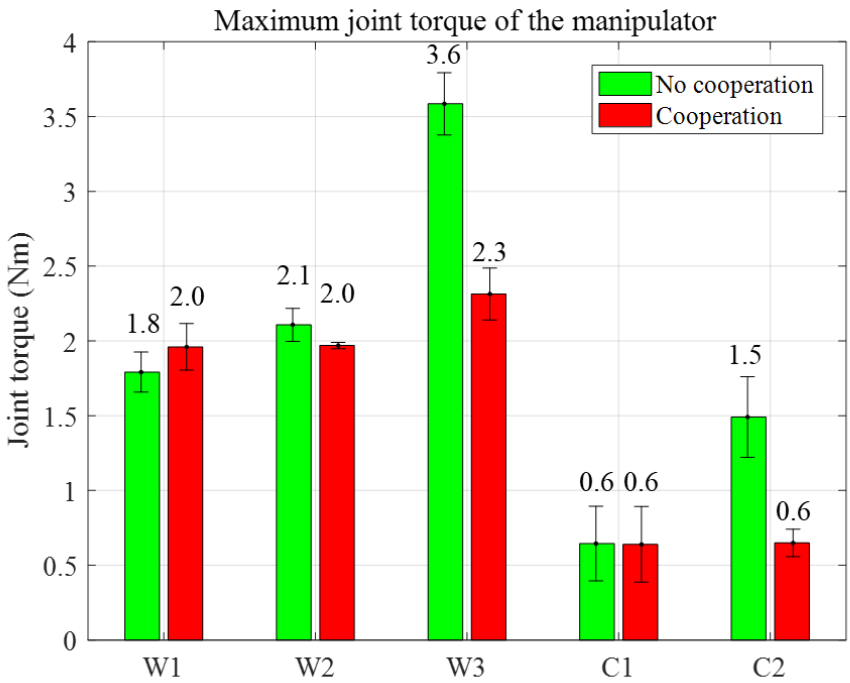

Fig. 6.27 Vehicle thrust force vector of valve turning experiment with selected cooperation weighting.

6.2.3. Disturbance compensation

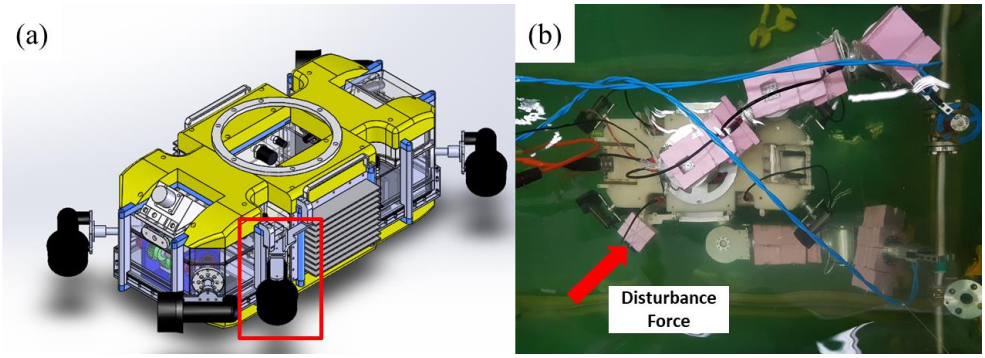

Fig. 6.28 Disturbance generator of the system. (a) Design of the disturbance generator. (b) Manufactured disturbance generator attached on the system.

The disturbance compensating experiment was conducted with disturbance generator made with a spare thruster for the vehicle. The thruster can produce about 25 N force forward and backward direction. 3D printer was used to manufacture the mount for fixing disturbance generator to the vehicle. Fig. 6.28 shows the design and the manufactured disturbance generator. The size of disturbance was controlled with PWM signal to the thruster. The model derived by previous research was used to estimate relation between PWM signal and generated disturbance force [8].

To show the effect of cooperation on compensating disturbance, the disturbance was applied while the system maintains its initial position. Fig. 6.28 (b) shows the experiment of compensating disturbance. In this case, 5 N size disturbance was applied.

Table 6.4 Joint torque values of two cases.

	W1	W2	W3	C1	C2
Vehicle only	0.03 Nm	0.01 Nm	0.02 Nm	0.02 Nm	0.02 Nm
Cooperation	0.08 Nm	0.06 Nm	0.12 Nm	0.08 Nm	0.07 Nm

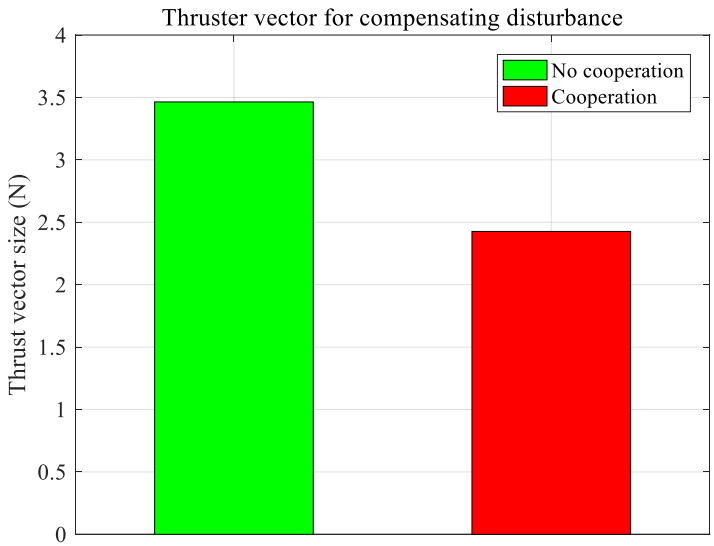

Fig. 6.29 Thrust vector size of two cases. In case of compensating disturbance with vehicle only is denoted as green bar, and case of compensating disturbance with cooperation is denoted as red bar.

The data was acquired by averaging of five experiments. The data of first 15 seconds was cut to ignore effect from transient state. Table 6.3 shows the joint torque for compensating disturbance of two cases. About 0.1 Nm of the joint torque is used for compensating disturbance. Fig. 6.29 shows the vehicle thrust vector size of two cases. The vehicle thrust is reduced about 30 % when using manipulator torque for compensating disturbance. Therefore, it can be concluded that cooperation on compensating disturbance is efficient as shown on the previous simulation.

6.2.4. Combined experiments

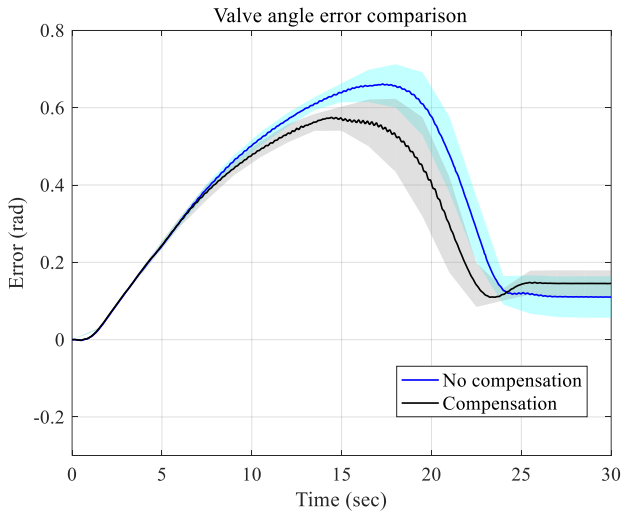

Fig. 6.30 Valve angle error in case of applying compensating term (black line), and case of not applying compensating term (blue line).

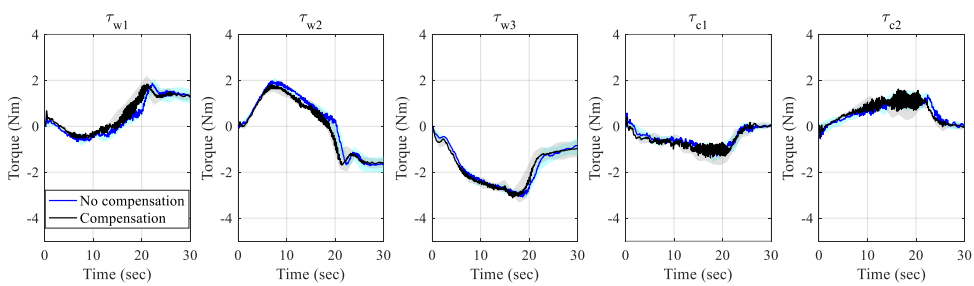

Fig. 6.31 Joint torque values with disturbance compensation and with disturbance compensation.

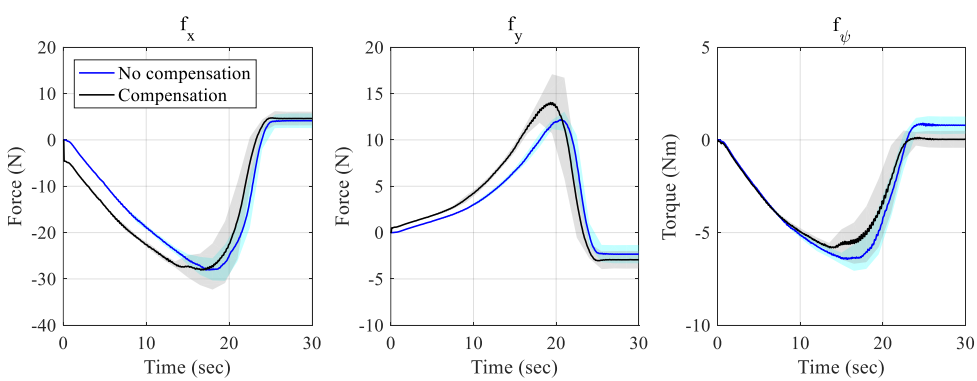

Fig. 6.32 Vehicle thrust force components with disturbance compensation and with disturbance compensation.

After prove the effect of cooperation on compensating disturbance, valve turning experiments under disturbance were conducted to prove the performance of combined cooperation algorithm, the cooperation on turning handle valve and the cooperation on compensating disturbance. Two cases were compared to each other. The first case is turning handle valve with cooperation and without applying disturbance compensating term. The second case is turning the handle valve and compensating disturbance with cooperation. The size of the disturbance was set as 8.5 N, which is equivalent with the system is in the 0.4 m/s speed oceanic current, same as the speed of Kuroshio current [39]. The results were summarized on Fig. 6.30, Fig. 6.31 and Fig. 6.32. The experimental results without compensating term is denoted as blue line while the results with compensating term is denoted as black line. Similar to previous experiments, each experiment was conducted five times, and the graph shows the average value with thick line and the standard deviation with deem area.

As shown in the graphs, the root mean square value of the valve angle error is 15% reduced while applying the disturbance compensating term. However, the manipulator torque and the vehicle force were rarely increased when applying disturbance compensation algorithm. Therefore, the proposed disturbance compensation term can get rid of effects from external disturbance without adding large amount of manipulator torque and vehicle thrust force. In summary, the cooperation algorithm is beneficial for performing the handle valve turning task and compensating disturbance by reducing burden of the dual-arm manipulator.

Chapter 7. Conclusion

In this paper, the dual-arm manipulator for underwater vehicle was designed and manufactured for turning underwater handle valve, and the cooperative manipulation algorithm was proposed. First, the manipulation method for turning handle valve was proposed. The idea of clamping on the fixed structure while performing the task is created. While clamped on fixed structure, not only the system is being stable under disturbance, but also desired torque and thrusts are needed to perform valve turning. After that, the dual-arm manipulator for turning valve was designed and optimized to have maximum dynamic manipulability during operation. By distributing degree-of-freedoms between two manipulators, the optimal configuration of the dual-arm manipulator was selected. Link length of the manipulator was optimized to maximize dynamic manipulability considering dynamic properties. Cooperation algorithm was developed for performing objective task efficiently. By applying weighted pseudoinverse method on deriving desired torque and thrust generation algorithm, task load of the manipulator and the vehicle can be adjusted. Also, disturbance compensation method was developed with similar way. Likewise, the disturbance load can also be distributed between two subsystems. The proposed cooperation algorithm was proved by experiments. A joint module for underwater manipulator was designed and manufactured. To follow the desired torque from manipulation algorithm, PI torque controller was designed for the joint module. The dual-arm manipulator was made by connecting joint modules with linkages. By attaching the dual-arm manipulator to the vehicle, UVMS was made. The valve turning and disturbance compensating experiments were performed on the water tank with underwater handle valve structure. Advantages of the cooperation algorithm were proved by experiments. With the presented algorithm, the burden of manipulator was reduced by cooperation, and the system can perform same task with lighter and smaller manipulator.

Bibliography

[1] Leopard – Saab Seaeye, *http://www.saabseaeye.com/solutions/underwater-vehicles/leopard* (retrieved Aug. 01, 2018).

[2] DTG2 worker - Deep Trekker, *https://www.deeptrekker.com/product/dtg2-worker/* (retrieved Aug. 01, 2018).

[3] T.W. McLain, S.M. Rock, Experiments in the coordination of underwater manipulator and vehicle control, in: *Proceedings of OCEANS' 95, MTS/IEEE, Challenges of Our Changing Global Environment. IEEE* (1995) 1208–1215.

[4] J. Kim, W.K. Chung, J. Yuh, Dynamic analysis and two-time scale control for underwater vehicle-manipulator systems, in: *Proceedings of the 2003 IEEE/RSJ International Conference on Intelligent Robots and Systems*, Las Vegas, Nevada (2003) 577–582.

[5] P. Cieslak, P. Ridao, M. Giergiel, Autonomous underwater panel operation by GIRONA500 UVMS: A practical approach to autonomous underwater manipulation, in: *Proceedings of 2015 IEEE International Conference on Robotics and Automation*, Seattle, Washington (2015) 529–536.

[6] E. Simetti, G. Casalino, Whole body control of a dual arm underwater vehicle manipulator system, *Annual Reviews in Control*, 40 (2015) 191-200.

[7] O. Khatib, X. Yeh, G. Brantner, B. Soe, B. Kim, S. Ganguly, H. Stuart, S. Wang, M. Cutkosky, A. Edsinger, P. Mullins, M. Barham, C. R. Voolstra, K. N. Salama, M. L'Hour and Vincent Creuze, Ocean One: A Robotic Avatar for Oceanic Discovery, *IEEE Robotics& Automation Magazine* (2016) 20-29.

[8] S. Jin, Hovering Control of an Underwater Robot with Tilting Thrusters Enabling Various Works, *PhD diss., Seoul National University* (2014).

[9] S. Jin, J. Kim, J. Kim, T.W. Seo, Six-degree-of-freedom hovering control of an underwater robotic platform with four tilting thrusters via selective switching control, *IEEE/ASME Transactions on mechatronics* 20(5) (2015) 2370–2378.

[10] S. Jin, J. Kim, J. Bae, T.W. Seo and J. Kim, Design, modeling and optimization of an undertwater manipulator with four-bar mechanism and compliant linkage, *Journal of Mechanical Science and Technology* 30 (9) (2016) 4337-4343.

[11] Surface wellhead equipment modified for subsea well control, *https://www.offshore-mag.com/articles/print/volume-67/issue-8/construction-installation/surface-wellhead-equipment-modified-for-subsea-well-control.html* (retrieved Nov. 13, 2018).

[12] MARDIVE marine & commercial diving, *http://www.mardive.gr/services.html* (retrieved Nov. 13, 2018).

[13] Subsea valves | ABV, *http://www.abvvalves.com/content/subsea-valves.html* (retrieved Nov. 25, 2018).

[14] E. Cataldi, G. Antonelli, Basic interaction operations for an underwater vehicle-manipulator system, in: *2015 International Conference on Advanced Robotics*, Istanbul, Turkey (2015) 524-529.

[15] P. Cieslak, P. Ridao, M. Giergiel. Autonomous Underwater Panel Operation by GIRONA500 UVMS: A Practical Approach to Autonomous Underwater Manipulation. IEEE International Conference on Robotics and Automation (ICRA), 2015.

[16] Y. Seki, S. Sagara, R. Ambar, Impedance Control of Dual-Arm 3-link Underwater Robot, ICT-robot 2018, Busan, Sep., 2018.

[17] K. Harada, H. Hirukawa, F. Kanehiro, K. Fujiwara, K. Kaneko, S. Kajita, M. Nakamura, Dynamical balance of a humanoid robot grasping an environment, *Proceedings of the 2004 IEEE/RSJ International conference of intelligent robots and system* (2004) 1167–1173.

[18] K. Koyanagi, H. Hirukawa, S. Hattori, M. Morisawa, S. Nakaoka, K. Harada, S. Kajita, A pattern generator of humanoid robots walking on a rough terrain using a handrail, *Proceedings of the 2008 IEEE/RSJ International conference of intelligent robots and system* (2008) 2167–2622.

[19] C. Lehmann, B. Olofsson, K. Nilsson, M. Halbauer, M. Haage, A. Robertsson, O. Sornmo, U. Berger, Robot joint modeling and parameter identification using the clamping method, In: *7th IFAC*

Conference on Manufacturing Modelling, Management, and Control in: International Federation of Automatic Control, Saint Petersburg, Russia (2013) 813–818.

[20]S. Sivcev, J. Coleman, E. Omerdic, G. Dooly and D. Toal, Underwater manipulators: A review, Ocean Engineering 163 (2018) 431-450.

[21]F. Inoue, T. Murakami, K. Ohnishi, A Motion Control of Mobile Manipulator with External Force, *Transactions on Mechatronics* 6 (2) (2001) 137-142.

[22]A. Dietrich, K. Bussmann, F. Petit, P. Kotyczka, C. Ott, B. Lohmann, A. Albu-Schaffer, Whole-body impedance control of wheeled mobile manipulators, *Autonomous Robot* 40 (3) (2016) 505-517.

[23]J. Han, J. Park, W. K. Chung, Robust coordinated motion control of an underwater vehicle-manipulator system with minimizing restoring moments, *Ocean Engineering* 38 (2011) 1197-1206.

[24]E. Simetti, G. Casalino, Whole body control of a dual arm underwater vehicle manipulator system, *Annual Reviews in Control* 40 (2015) 191-200.

[25]J. Russakow, O. Khatib, S. M. Rock, Extended operational space formulation for serial-to-parallel chain (branching) manipulators, In: *Proceedings of 1995 IEEE International Conference on Robotics and Automation* (1995) 1056–1061.

[26]S. Lee, Research on antagonistic stiffness for over-actuated parallel mechanisms, *PhD dissertation*, Seoul National University (2008).

[27]H. S. An, J. H. Lee, C. Lee, T. Seo, J. W. Lee, Geometrical kinematic solution of serial spatial manipulator using screw theory, *Mechanism and Machine Theory*, 116 (2017) 404–418.

[28]I. Schjolberg, T. I. Fossen, Modelling and control of underwater vehicle-manipulator systems, In: *Proc. rd Conf. on Marine Craft maneuvering and control* (1994) 45–57.

[29]H. Cheng, Y.-K. Yiu, Z. Li, Dynamics and control of redundantly actuated parallel manipulators, IEEE/ASME Transactions on mechatronics 8 (4) (2003) 483–491.

[30]J. Bae, J. Bak, S. Jin, T. Seo, J. Kim, Optimal configuration and parametric design of an underwater vehicle manipulator system for a valve task, *Mechanism and Machine Theory* 123 (2018) 76–88.

[31]T. I. Fossen, Guidance and control of ocean vehicles, *John Wiley & Sons Inc*. (1994).

[32]T. Yoshikawa, Dynamic manipulability of robot manipulators, in: Proceedings of 1985 IEEE International Conference on Robotics and Automation in: Robotics and Automation. Proceedings. 1985, pp. 1033–1038.

[33]Maxon motor, http://www.maxonmotor.com/maxon/view/content/index (retrieved Dec. 21, 2017).

[34]M. W. Spong, S. Hutchinson, M. Vidyasagar, Robot modeling and control, *John Wiley & Sons Inc.* (1989).

[35]F. M. White, Fluid mechanics, fourth edition, *McGraw-Hill* (1999).

[36]L. Elden, A weighted pseudoinverse, generalized singular values, and constrained least square problems, *BIT Numerical Mathematics* 22 (4) (1982) 487-502.

[37]S. Jin, J. Bae, J. Kim, T.W. Seo, Disturbance compensation of a dual-arm underwater robot via redundant parallel mechanism theory, *Meccanica* 52 (7) (2017) 1711-1719.

[38]H. Olsson, K. J. Astrom, C. Canudas de Wit, M. Gafvert, P. Lischinsky, Friction Models and Friction Compensation, European Journal of Control 4 (3) (1998) 176-195.

[39]M. G. Gross, Oceanography, 6th ed., *Columbus: Merrill* (1990) 74-75.

Abstract

본 연구에서는 수중 양팔 매니퓰레이터를 장착한 무인잠수정을 사용하여 수중 밸브를 개폐하는 작업 방법을 제시하였으며 무인잠수정과 양팔 매니퓰레이터 간 협업 알고리즘을 개발하여 작업 성능의 향상 및 두 시스템간 작업 부담의 분배, 그리고 외란 보상을 실현하였다. 기존 수중 시스템에서는 무인잠수정을 고정시키지 않고 작업을 수행하며 작업에는 매니퓰레이터만 사용하고 외란 보상에는 무인잠수정 자체의 추력만을 사용한다. 본 논문에서는 한쪽 팔을 사용해서 무인잠수정을 고정시킴으로써 작업 효율 증가, 외란에 대한 안정성을 확보하였다. 또한 작업 진행과 외란 보상 각각에 대해서 무인잠수정과 매니퓰레이터가 서로 협업하는 알고리즘을 도입하여 기존의 작업 방법보다 작은 매니퓰레이터 토크로 효율적으로 작업을 수행할 수 있음을 증명하였다.

밸브 개폐 작업을 하는데 있어서 본 논문에서는 양팔 중 한 쪽 팔로 고정된 구조물을 잡은 채로 작업하는 방법을 새롭게 제시하였다. 구조물에 한쪽 팔을 고정시킬 경우 전체 시스템은 닫힌 고리 형태로 구성되어 병렬 매니퓰레이터의 기구적 특성을 가지게 된다. 병렬 매니퓰레이터의 특성으로 인해서 특정 작업을 진행하는데 양팔 매니퓰레이터와 무인잠수정의 추력 간 힘 분배가 가능해지며 추가적으로 내력을 생성시켜 수중에서 중요한 요소인 외란을 쉽게 보상할 수 있다. 기존의 고정되지 않은 채로 한 팔, 혹은 양팔로 작업하는 방식에 비해서 작업에 필요한 무인잠수정 추력과 양팔 매니퓰레이터의 토크가 모두 감소됨을 동역학 시뮬레이션을 통해서 검증하였다. 이런 이점은 외란이 가해질 경우 더욱 잘 드러나는 것이 확인되었다.

해당 작업 방식을 바탕으로 양팔 매니퓰레이터의 구조 선정과 링크 길이의 최적화가 진행되었다. 매니퓰레이터의 총 자유도를 지정 후, 각각의 자유도를 양팔에 분배하는 방법을 사용하여 네 가지의 설계 대안을 고안하였다. 동역학적 조작성 지수(dynamic manipulability)를 최적화 목적함수로 선정하고 각각의 설계 대안들을 밸브를 돌리는 동안의 총 동역학적 조작성 지수가 가장 높게 되도록 유전 알고리즘을 이용해 궤적과 링크 길이를 최적화하였다. 이후 가장 높은 최적화 목적함수 값을 가진 2개의 대안 중에서 무인잠수정의 추력을 함께 사용할 수 있는 구조로 전체 시스템 구조를 선정하였다.

효율적인 밸브 회전 작업을 위해서 시스템의 특성을 응용하여 양팔 매니퓰레이터와 무인잠수정 간 협업 알고리즘을 개발하였다. 시스템이 병렬 매니퓰레이터의 기구학적 특성을 가짐과 동시에 여유자유도가 있으므로 야코비 행렬의 가중의사역행렬(weighted pseudoinverse)을 취하여 양팔 매니퓰레이터와 무인잠수정 추력 간에 작업 부담을 분배할 수 있다. 밸브 회전 작업의 경우 기존 시스템에서는 사용하지 않던 무인잠수정의 추력을 작업에 같이 사용할 수 있으며 외란 보상 시에는 매니퓰레이터의 작은 토크로 효율적으로 무인잠수정의 외란 보상을 도울 수 있다. 본 연구에서는 최대 힘이나 토크에 비례해서 부담을 분배하였으며 우선 시뮬레이션을 통해서 본 알고리즘의 이점을 분석하였다. 무인잠수정의 추력을 사용할 경우 매니퓰레이터의 최대 토크가 크게 줄어드는 것이 확인되었으며 반대로 외란 보상에 대해서는 작은 매니퓰레이터 토크를 가했음에도 외란보상에 필요한 무인잠수정 추력이 크게 감소하였다.

마지막으로 실험을 통해 양팔 매니퓰레이터와 무인잠수정의 협업 알고리즘을 검증하였다. 방수 기능이 있는 관절 모듈을 설계 및 제작하였으며 관절 모듈을 서로 체결하는 방식으로 전체 매니퓰레이터를 구성하였다. 관절 모듈이 원하는 토크를 가할 수 있도록 토크 센서 피드백을 이용한 제어기를 구성하였으며 방수 구조에서 기인한 마찰 보정 알고리즘 또한 구성하였다. 수중 밸브 구조물을 모사한 테스트 벤치에서 밸브 개폐 및 외란 보상 실험을 진행하였으며 실험을 통해 협업 알고리즘의 효과를 증명하였다.

주요어 : 수중 잠수정-매니퓰레이터 시스템, 양팔 매니퓰레이터, 모바일 매니퓰레이션, 협업, 밸브 회전 작업, 매니퓰레이터 설계.

학번 : 2012-23167